Stimuli-Responsive Peptide Self-Assembly for Therapeutic Delivery

by

Su Yang

Presented to the Faculty of the Graduate School of

The University of Texas at Arlington in Partial Fulfillment

of the Requirements

for the Degree of

DOCTOR of PHILOSOPHY

THE UNIVERSITY OF TEXAS AT ARLINGTON

August 2022

Abstract

Peptide self-assembly offers an effective method to generate supramolecular nanomaterials with much higher stability than traditional monomeric peptides. The materials exhibit well-organized hierarchical structures and high resistance toward proteolysis and have been utilized extensively in various biomedical applications. Furthermore, due to the prevalence of non-covalent interactions, these structures are highly dynamic. The dynamic nature is beneficial for the design and synthesis of smart, trigger-responsive peptide self-assembly under specific stimulus, in particular various stimuli associated with disease conditions. In **Chapter 1**, I will introduce different types of peptide building blocks used for the construction of peptide self-assembly. I will further discuss the design of trigger-responsive peptide self-assembly that are formed under disease-specific triggers such as pH, redox and enzymes.

In **Chapter 2**, I will focus on the design, synthesis, and characterization of a reductive-responsive self-assembled peptide nanofibers, to selectively target therapeutics to tumor cells with high levels of glutathione. The peptide nanofibers exhibit supramolecular-structure dependent cell penetrating activity and can be controlled with a reductive tumor microenvironment. The reduction-dependent structure and activity were thoroughly investigated using combined biophysical methods and *in vitro* cell-based assay.

In **Chapter 3**, I conducted a more systematic design approach to understand the relationship between supramolecular structure and cell penetrating activity. A small library of multidomain peptides (MDPs) with a general sequence of $K_x(QW)_6E_y$ was synthesized and used to probe the supramolecular structure-dependent cell penetrating activity. It was found that cell penetrating activity is dictated by both supramolecular stability and conformational flexibility of the charged domain. Preliminary screening studies identified $K_{10}(QW)_6E_3$ as the self-assembling precursor to form nanofibers with most potent cell penetrating activity. This sequence was further selected for the construction of enzyme-responsive cell penetrating nanofibers for tumor cell targeting, which will be described in **Chapter 4**.

In **Chapter 4**, I will discuss my efforts on a more advanced design and synthesis of peptide nanofibers with enzymatic-controlled cell penetrating activity. This work could open new avenues for cancer imaging and therapy due to their potential of targeting overexpressed enzymes in different cancer tissues. Specifically, we synthesized a new family of MDPs that can undergo enzyme-mediated molecular transformation and supramolecular assembly to form nanofibers. The MDP is designed to have three modules, a membrane-active self-assembling (SA) module, a cationic capping (CC) module and labile linker (LL) module. The hypothesis is in the presence of the cationic CC domain, due to the abundance of the cationic charges and increased electrostatic repulsion, MDPs do not self-assemble and therefore have weak membrane activity. When the external stimulus is applied under specific cellular condition, the LL domain is cleaved to release the CC domain. Consequently, the ability of MDPs to self-assemble is restored to form nanofibers with improved membrane activity. As a proof-of-concept study, we chose matrix metalloproteinase 2, MMP-2 as our initial cellular target due to its overexpression by cancer cells. We synthesized an MDP consisting of an MMP-2 responsive substrate as the linker and observed high cell penetrating activity in the presence of MMP-2. *In vitro* cell-based assay supports our design based on the therapeutic efficacy against cancer cells with and without endogenous MMP-2.

In **Chapter 5**, I will shift gear and discuss our recent work for the development of pH-responsive peptide materials which have potential for both anticancer and antimicrobial therapy development. This approach is based on the self-assembly of peptides containing unnatural ionic amino acids with an aliphatic tertiary amine side chain. These residues generally have a high pKa value in the basic pH range and may be less useful for the design of biomaterials. We found that when they are incorporated in a peptide self-assembly, the hydrophobic microenvironment within the assembly shifts their pKa significantly from a basic pH to a more biologically relevant pH in the weakly acidic range, therefore greatly boosting their therapeutic potential. I will discuss in detail the synthesis, structural characterization and antimicrobial activity of these pH-responsive peptide self-assembly.

Acknowledgments

I would like to thank to Professor He Dong for her guidance and dedication to my study in the field of self-assembled peptides. I have learned peptide synthesis skills and multiple instrumental characterization, but more importantly I completed the training of thinking process for how to do research and problem solving. I also want to thank my committee member Professor Carl J. Lovely, Professor Subhrangsu Mandal and Professor Junha Jeon for their comments and kind suggestion along my research process. I would like to thank Professor Frank Foss, Professor Kytai T Nguyen and Professor Reidar Lund for their help in our collaboration.

I wonld also like to thank everyone in Dong lab: Dr. Dawei Xu, Weike Chen, Dr. Xiushuang Yuan, Ryan Madigan, Dr. Jun Wang, Haritha Asokan Sheeja, and our undergraduate Ashley Anne Adones. Your help and encouragement help me come through all the tough times. I also want to thank my other friends that help me with my research during me Ph.D study. I will thank Dr. Chad Brautigam and Dr. Tso Shih-Chia for their help in AUC study. I will thank Dr. Jiechao Jiang, Dr. Yi Shen and Chuzhong Zhang for their help in TEM study. I will thank John C Lang for his kind suggestions for my study. I wish to thank Dr. Yan Chang for her help with the confocal microscope and cell study. I thank Dr. Shuxin Li for his help with different characterizations. I would thank Dr. Uday K. Chintapula for his help with the cell study. I will thank Brandon B Fulton and Shan Hazoor for their help with NMR study.

Financial support from NSF and the University of Texas at Arlington are grateful acknowledged.

Finally, I want to thank my Mom for encourages and supporting me over the years. Also thanks my best friends Weiya Wang, Chen Zhang and Pupu for keep company through the tough days.

Contents

List of Figures

List of Table

Abbreviations

AUC	Analytical Ultracentrifugation
Boc	Tert-butyloxycarbonyl
CAC	Critical aggregation concentration
CD	Circular dichroism
CLSM	Confocal laser scanning microscope
CPP	Cell penetrating peptide
CR	Congo red
DCM	Dichloromethane
DIPEA	N, N-Diisopropylethylamine
DMF	Dimethylformamide
DMSO	Dimethyl sulfoxide
DOX	Doxorubicin
DTT	DL-Dithiothreitol
ESI/MS	Electrospray ionization/mass spectrometry
FITC	Fluorescein isothiocyanate

Fmoc	Fluorenylmethyloxycarbonyl
HPLC	High-performance liquid chromatography
HBTU	*N,N,N′,N′*-Tetramethyl-*O*-(1*H*-benzotriazol-1-yl)uronium hexafluorophosphate
MALDI	Matrix assisted laser desorption ionization
MIC	Minimum inhibitory concentration
MDP	Multidomain peptide
MMP	Matrix metalloproteinase
MPA	Mercaptopropionic acid
NBD	Nitrobenzoxadiazole
PBS	Phosphate-buffered saline
SPCN	Supramolecular peptide cell penetrating nanofiber
TEM	Transmission electron microscopy
TFA	Trifluoroacetic acid
THF	Tetrahydrofuran
TIS	Triisopropylsilane

Chapter 1. General Introduction to Peptide Self-Assembly

Peptides consist of short chains of amino acids which are held together by amide bonds to form different molecular secondary structures to serve different functions.[1] Based on the amino acid sequence, various secondary structures such as α-helices and β-sheets can be formed. These secondary structures can further assemble to form more complex tertiary and quaternary structures as seen in proteins. Peptides are widely used for biomaterial studies due to their bioactivity, biocompatibility, and biodegradability[2-4] and have found use in biomedical applications such as drug delivery[5-6], cell growth scaffolds[7], antibacterial[8-9], and wound healing[10]. However, there are significant challenges with traditional single chain peptides as most of them suffer from instability and enzymatic degradation in physiological conditions.[11-12] Peptide self-assembly offers an effective method to generate supramolecular nanomaterials with improved stability, dynamic nanostructure, and biological activity. Self-assembled peptides are constructed by means of non-covalent interactions such as hydrogen bonds, hydrophobic effects, and electrostatic interactions. The supramolecular approach strikes a good balance between traditional monomeric peptide and polymer-based materials fofabrication and use in therapeutic delivery due to their tunable stability, structural dynamics and the ease of incorporation of various chemical and biological functionalities.[13] Parallel development of *de novo* peptide design seems to seamlessly fit into the material framework by providing diversified molecular building blocks with different structure and functionality.

1.1 Strategies for Peptide Self-Assembly

Depending on the types of molecular building blocks involved in the self-assembly, several strategies have been reported for the design and synthesis of self-assembling peptides. Commonly used motifs include peptides that form β-sheets/hairpins and alpha helices/coiled coils and chemically modified amphiphilic peptides, such as peptide amphiphiles and short aromatic peptide derivatives (**Fig. 1.1**). The peptide building blocks can be naturally derived or through *de novo* design. Various *de novo* design rules are established and available to guide peptides to form desired secondary structures, in particular β-sheets and alpha helices. The amino acids within secondary structure have highly specific interactions to form higher-order supramolecular assemblies by means of non-covalent interactions. Alternatively, chemically modified peptides can be used to provide additional driving force for self-assembly to occur. For example, peptide amphiphile utilizes the hydrophobic effects among the alkyl chains that are attached to the N-terminus of a peptide to drive self-assembly. In the following section, examples of peptide self-assembly based on different peptide molecular building blocks will be discussed.

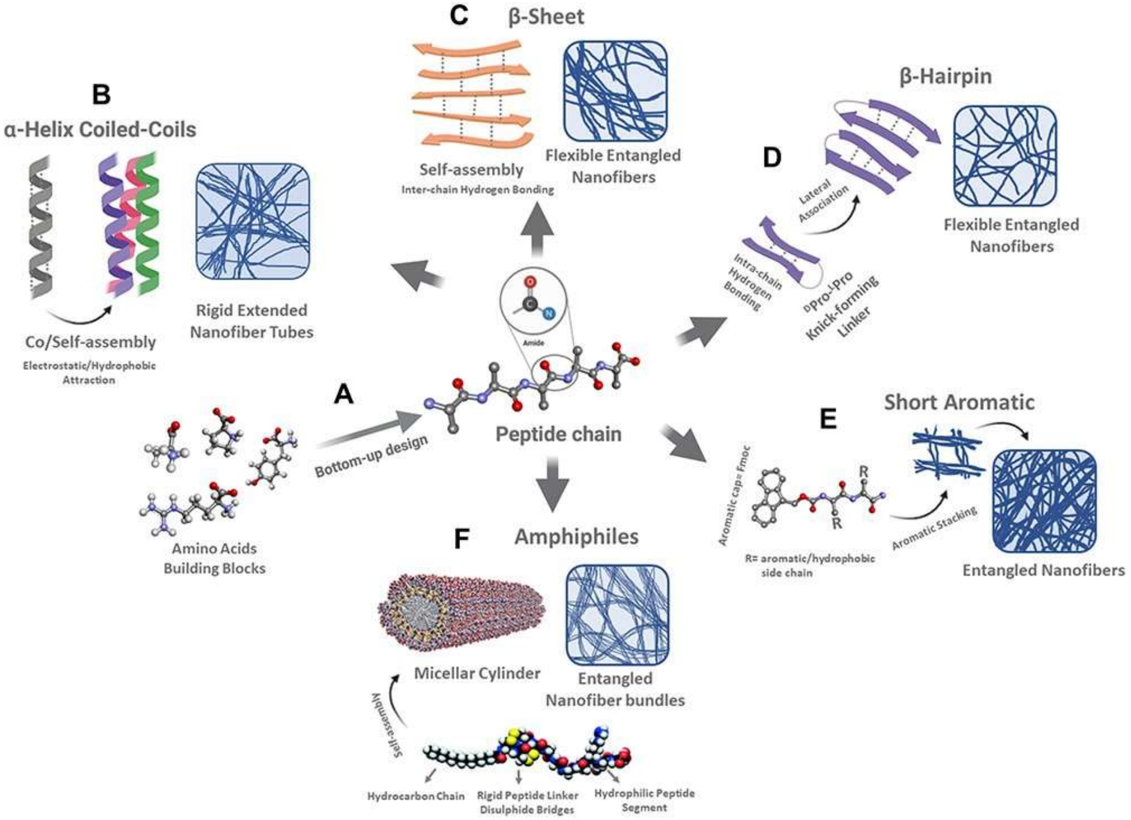

Figure 1.1 Peptide self-assembly based on *de novo* designed peptides. (A) Amino acids acting as building blocks to form oligopeptides that have different molecular secondary structures, such as (B) α-helix (C) β-sheet, (D) β-hairpin. Molecular building blocks based on chemically modified peptides including (E) short aromatic, and (F) amphiphile peptides.[14]

1.1.1 β-sheets

The β-sheets and β-hairpin motifs are typically formed by intermolecular hydrogen bonding between amide bonds. Each of the peptide chains is referred to as a strand and the hydrogen bonded strands are referred to as sheets. Based on the orientation of hydrogen bonds between sheets and side chain interactions, β-sheets can be orientated either as a parallel or anti-parallel structure. The parallel and anti-parallel structures of β-sheets were identified by Pauling, Corey and others in the early 1950's when the possible structures that proteins could adopt were identified.[15] β-Sheets are well known for their ability to assemble into long fibrous structures, which are present in amyloid diseases like Alzheimer's and

Parkinson's diseases.[16] The basic building block of β-sheets is alternating hydrophobic, hydrophilic residues. This special pattern produces a hydrophobic and hydrophilic face on the peptide sheet, allowing two sheets to assemble by hydrophobic packing forces. The sandwich-like structure has a tendency of to assemble into a nanofiber structure (**Fig. 1.2**). Recent studies show that by adding certain hydrophilic motifs, the length and morphology of the nanofibers can be tuned by multiple factors.

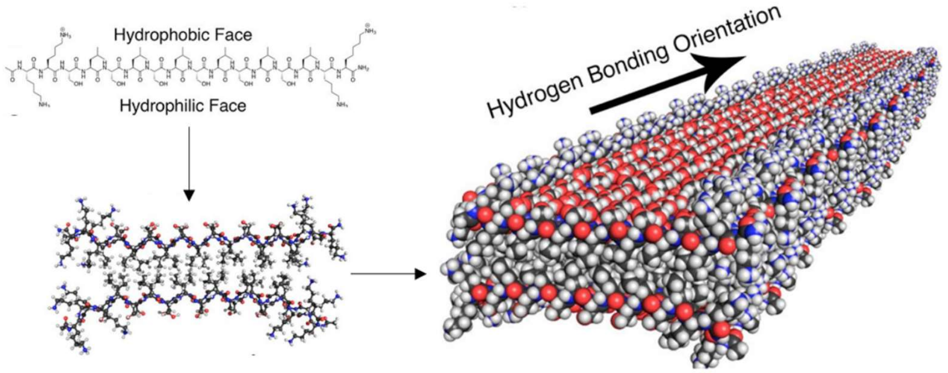

Figure 1.2 β-Sheet forming short peptides with alternating ionic complementary properties. [17]

Self-assembly ability can be controlled by multiple structural factors. The effect of hydrophobic residues on self-assembly was studied and revealed that stable assembly can be achieved with peptide sequences (FKFE), (IKIE) and (VKVE) with 2-4 repeating units.[18] Sequences with more hydrophobic residues were demonstrated to have significantly lower critical assembly concentrations. Also, the critical assembly concentrations of the peptide increases with the increasing number of repeating units due to a competition between enthalpy and entropy.

Incorporation of additional hydrophilic amino acids can be used to further tune the self-assembly. The self-assembling ability of multi-domain peptides with a general sequence of $K_x(QL)_yK_x$ was studied by changing the ratio of x/y.[19] Increasing the number of charged domains leads to a spherical micelle structure. Additionally, the increase of the hydrophobic domains leads to the fiber structures, and eventually results in aggregation.

Charge–charge interactions also play a role in assembly. The electrostatic interaction between multiple sheets highly affects the assembly of these systems. The EAK16-II (AEAEAKAKAEAEAKAK) peptide has been found to form high stabile nanofibers in aqueous solution.[20] The structure has minimum change under high temperature, extreme pH and high salt concentration. This unique property is presumably due to the checkerboard-like ionic interactions.

In summary, the design of β-sheet based peptide nanofibers is well understood with a number of designed systems that have been extensively studied. They have been utilized for bio-medical application *in vitro* and *in vivo* levels.

1.1.1 α-helix

The alpha helix is another folding motif found in proteins. As an alternative to β-sheets, α-helices are used as components of coiled-coils as first described by Pauling, Corey and Crick.[15] Coiled-coil structures usually consist of at least two helices that come together to bury a hydrophobic interface. It is possible to make more complicated interfaces involving multiple helices through the interactions of neighbors. A seven residues sequence serves as the basic heptad unit for coiled-coil α-helices (**Fig. 1.3A**). The hydrophobic residues at the a and d positions, as well as the charged residues at the e and g positions are the dominate amino acids for directing the dimer interface. The rest of the residues at the b, c, and f positions are exposed on the surface, allowing these to be varied and modified for different design requirements.[21] The configuration of the coiled-coil motifs can be manipulated by changing environmental conditions such as temperature, pH and ionic strength.

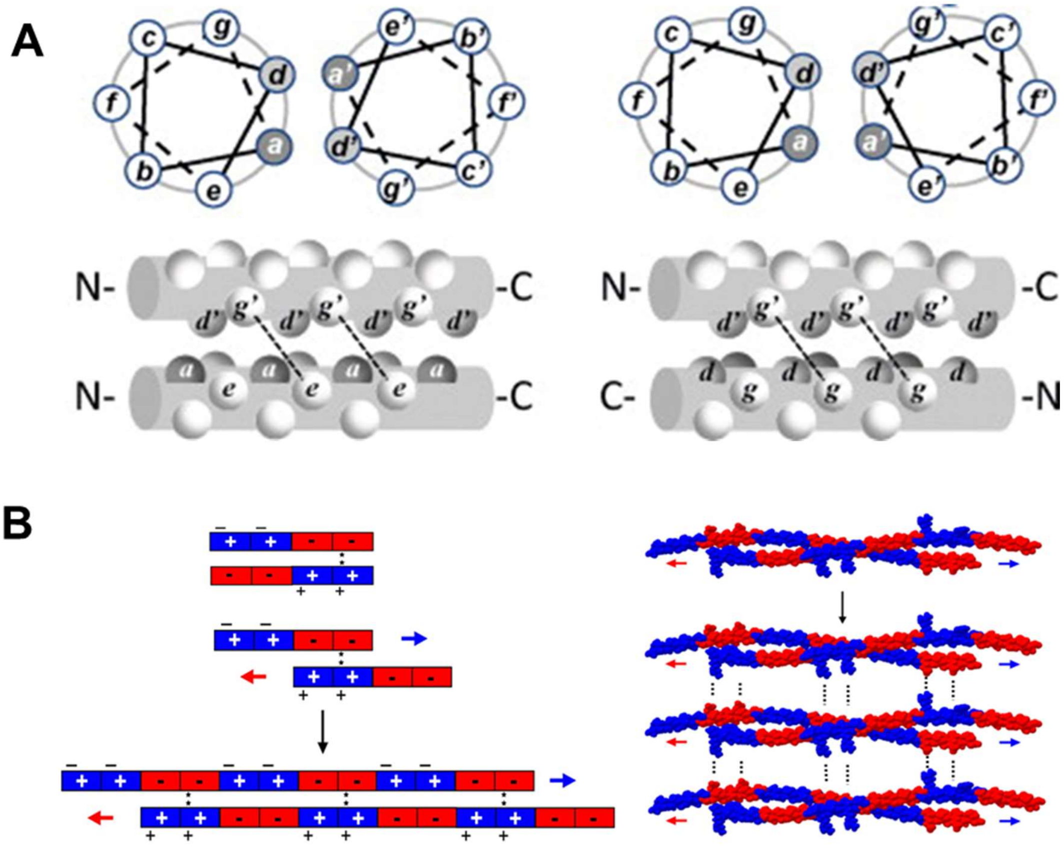

Figure 1.3 (A) Helical wheel diagrams (top) and side-view representations (bottom) illustrating the absolute position of residues in a parallel or antiparallel dimeric CC. C- (carboxy-) and N- (amino-) indicate the peptide termini.[22] (B) Design principles of the SAF peptides. In the SAF system, complementary charges in companion peptides direct the formation of staggered, parallel, and codirectional heterodimers. The resulting “sticky ends” are also complementary and promote longitudinal association into extended fibers. Complementary charged pairs on the outer surfaces of the coiled-coil protofibrils promote protofibril–protofibril interactions, fiber assembly, and thickening.

The design of the GCN4 leucine zipper represents a successful platform for creating a broad range of structural forms by performing minor changes to its sequence. In the native state, it forms a parallel, two-helical coiled-coil of 30 residues (GCN4-p1).[23-24] By changing amino acids at the helix interfaces, the stability typically increases but leads to heterogeneous oligomerization states, including trimers or mixtures of dimers and trimers. It was found that coiled-coil dimers favor β-branched residues in the a position and γ-branched or unbranched residues in the d position, while tetramers show the opposite trend of amino acid preference. Further studies show consistent results with the above rule. For example, a retro-GCN4, consisting of an inversion GCN4 sequence, yielded a tetramer with swapping the amino acids at the a and d position. Other combinations of isoleucine, leucine, and valine in the hydrophobic position typically resulted in trimers or occasionally mixtures of dimers and trimers.

Self-assembly of coiled-coils into higher-order supramolecular nanostructures was first demonstrated by the Woolfson group using the approach of so called ‘‘sticky end’’ assembly(**Fig. 1.3B**).[25] A heterodimeric parallel coiled coil, SAF-p1 and SAF-p2, was designed to have a staggered hydrophobic interface which triggers supramolecular polymerization of coiled coils into elongated nanofibers.

1.1.3 Amphiphilic Peptides

Peptide amphiphiles (PA) are constructed with peptides that are modified with a hydrophobic alkyl tail to generate an amphiphiles. When these molecules are in an aqueous solution, they generally assemble into high aspect ratio nanostructures with a hydrophobic core consisting of carbon alkyl tails. Hydrogen bonding within the β-sheet forming peptides also drives it to assemble into nanofibers. The diameter and length can be adjusted by the lipid tail length, the number of charged amino acids, and self-assembly conditions. The peptide sequences can incorporate various ligands to target different cell surface receptors or peptide sequences that facilitate intracellular uptake. The hydrophobic core can be used for cargo loading and delivery. It has been reported that mixing oppositely charged PA molecules allows for the generation of fibers with improved stability.[26]

Hartgerink et al.[27] first demonstrated the self-assembly of PA with tailored nanostructure and chemical functionality (**Fig. 1.4**). These self-assembled PA has been used for controlled biomineralization. The alkyl chain provides a hydrophobic effect to promote self-assembly. The cystines were introduced to form crosslinking and stabilize the hydrophobic core. The glycines work as a linker to provide sufficient flexibility of the hydrophilic head group. The phosphorylated serine was used to accomplish targeted mineralization. A RGD sequence was appended as an integrin-receptor targeting ligand. This highly dynamic PA system could capture multiple types of responsiveness and achieve targeted function in relatively simple structures.

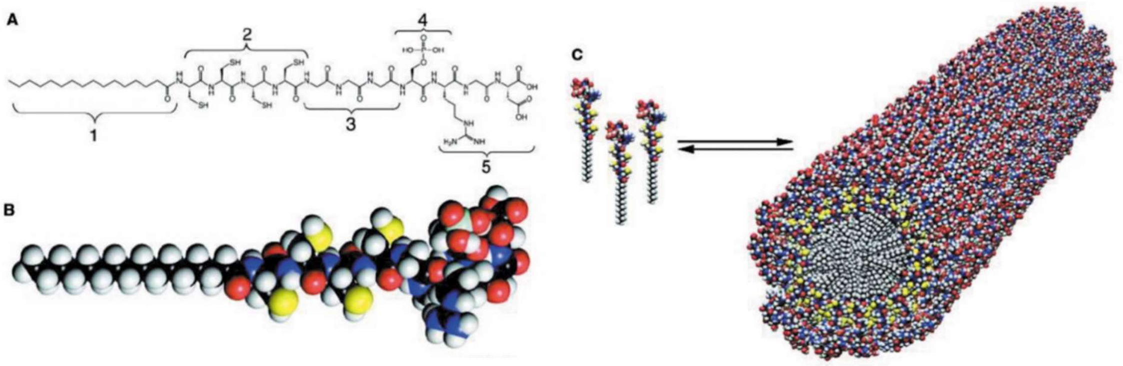

Figure 1.4 (A) Chemical structure of Hartgerink's peptide amphiphile. (B) Molecular model of the peptide amphiphile, showing its conical shape. (C) Schematic showing the self-assembly of the amphiphiles into a cylindrical micelle.

1.2 Stimuli-Responsive Peptide Self-Assembly

1.2.1 pH-Responsiveness Peptide Self-Assembly

pH responsiveness can be achieved either in the extracellular environment or in the endosomal/lysosomal environment. Compared to normal tissues, tumors can induce acidic extracellular environments. The pH in certain regions is 6.5-6.8 which is significantly different from human blood and normal tissue (~7.4). Endosomes/lysosomes have a lower pH (6.5-4.5) compared with those in the extracellular environment. Upon endocytosis, rapid drug release from endosome/lysosome is triggered by exposing designed materials in the acidic environment. pH-triggered drug release is achieved via two routes. First, the functional groups on drug carriers undergo protonation at the endosomal pH leading to disassembly of the nanocarrier to release therapeutic drugs.[28-29] Secondly, covalent bonds are broken upon acidification, inducing drug release.[30]

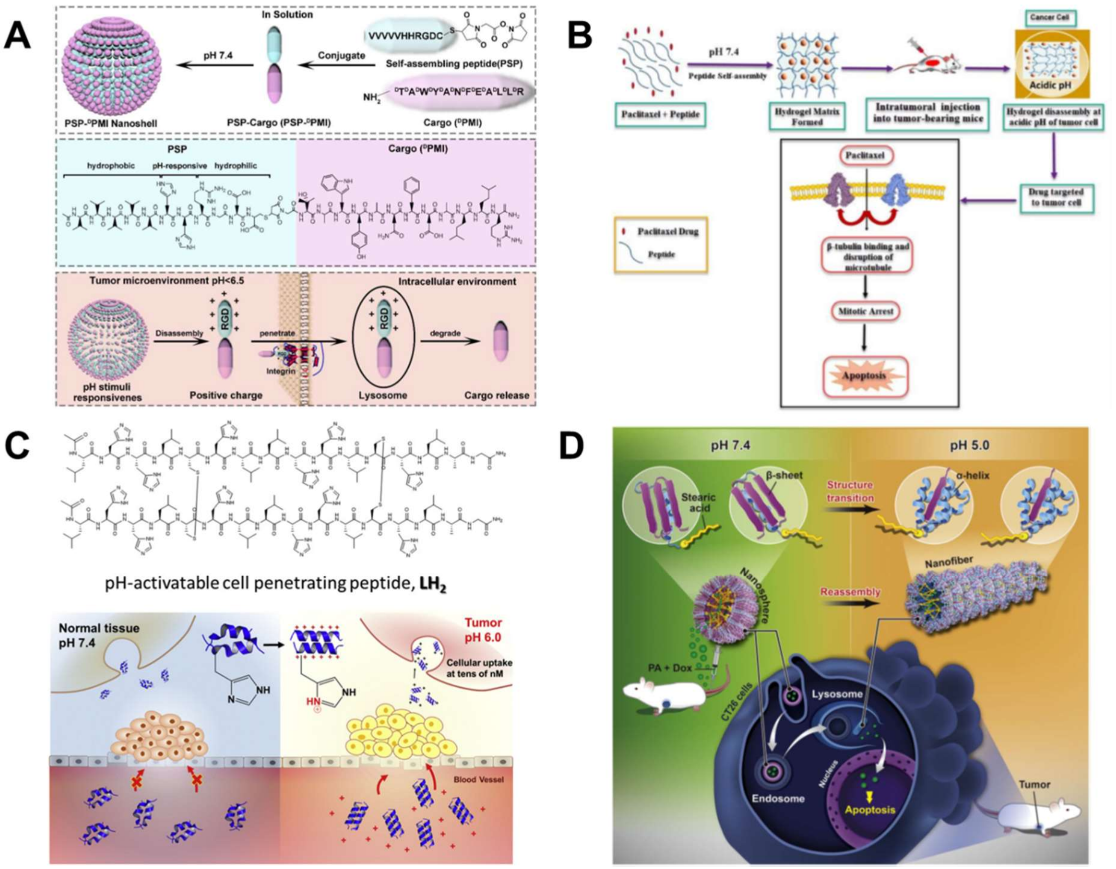

Figure 1.5 (A) Schematic illustration of self-assembly synthetic procedure and the properties of pH-responsive charge reversal and size change of PSP-DPMI spherical shells. (B) pH-responsive hydrogel consisting of self-assembly peptide FER-8 for the delivery of paclitaxel against tumor. (C) Schematic representation of pH-activatable penetration of cell penetrating peptide, LH2, into the acidic region. (D) Schematic illustration of pH-induced secondary structure transition of mimicking peptide amphiphile in the acidic microenvironment of tumor cell for controlled release and cell apoptosis.

He et al.[31] designed a pH-responsive self-assembling peptide (PSP) which consists of an N-terminal hydrophobic moiety (VVVVV), a pH-responsive segment (HH), and a C terminal hydrophilic sequence (RGDC) (**Fig. 1.5A**). This module is conjugated to a cargo and subsequently forms a nanoshell at neutral pH. The nanoshell disintegrates at pH 6.5 due to the protonation of histidine. The released monomer is then internalized and released the cargo. This design is widely suitable for hydrophilic therapeutic delivery. Raza et al.[32] reported an injectable drug loading peptide hydrogel with a sequence of FER-8 (FEFEFRFK) (**Fig. 1.5B**).

The peptides were formed with long crosslinked nanofibers and have high stability over 6 months. In tumor tissues, the acidic conditions trigger protonation which interrupts the secondary structure of the β-sheets and results in sustained diffusion over 14 hs. The intertumoral injection of the hydrogel can enhance tumor targeting and prolong retention. Coiled-coil based peptide self-assembles have also been explored for the development of pH-responsive peptide materials. Nam et al.[33] developed a histidine-based CPP dimer, LH2, of which cell penetrating activity can be activated only at a weakly acidic pH by the protonation of histidine(**Fig. 1.5C**). Due to dimer formation, cell penetration can be achieved at a low concentration. The selectivity of peptide assembly for targeting cancer cells has been confirmed *in vitro* and *in vivo*. Liang et al.[34] showed a new approach to fabricate pH-sensitive PA based on mimicking peptides and stearic acid. This self-assembled peptide nanostructure undergoes protonation in an endosomal low pH environment which is accompanied by the secondary structure changing from β-sheet to α-helix (**Fig. 1.5D**). The secondary structure changes lead to a nanostructure transformation from micelles to nanofibers, which facilitate drug release from nanomaterial and escape from the endosome by the proton sponge effect.

1.2.2 Reduction-Responsive Peptide Self-Assembly

The redox potential is significantly higher in tumors than that in normal tissues due to the overexpression of GSH. The reductive tumor microenvironment could be used as a trigger to mediate assembly/disassembly of peptides and further achieve site-specific therapeutic delivery.

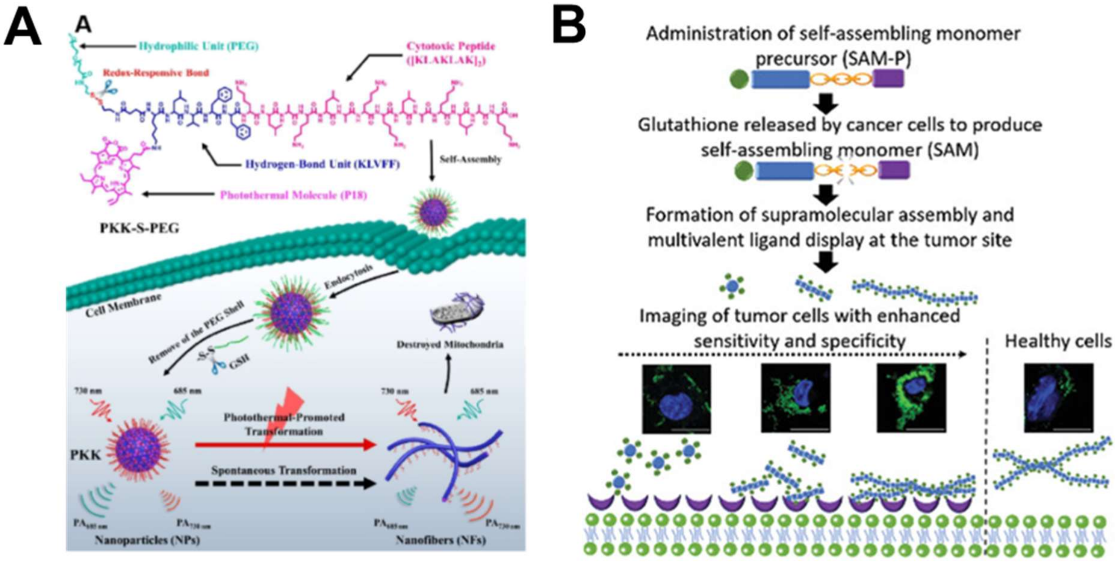

Figure 1.6 (A) Functionalized molecule structure and the transportation, cleavage, fibration process of PKK-S-PEG in cancer cells. (B) Illustration of the chemical design of the assembling precursor that undergoes reduction-triggered self-assembly to form supramolecular assemblies with multivalent ligand presentation for tumor targeting. Supramolecular structure-dependent receptor targeting with elongated nanofibers formed by SAM-P-262 offers higher sensitivity than short nanofibers and spherical aggregates.

Zhang et al.[35] established a reductive-responsive supramolecular peptide (**Fig. 1.6A**). The modularly designed β-sheet peptide contains four functional domains, including cell penetration, cell targeting, photothermal activity and reduction sensing. The PKK-S-PEG can assemble into nanoparticles that undergo structural transformation from micelles to fibers. The fiber structure was found to toxic by inducing mitochondria damage. Chen et al.[36] designed ligand conjugated self-assembling monomer precursor (SAM-P), with disulfide bonds as a responsive motif (**Fig. 1.6B**). SAM-P undergoes reduction-triggered cleavage to retrieve the self-assembling ability to form supramolecular peptide nanofibers. Upon self-assembly, ligands were organized in a multivalent manner at the fiber-solvent interface. *In vitro* cell-based fluorescence assay showed significant enhancement of membrane adherence, which supports the hypothesis that the supramolecular morphology is critical in mediating the ligand-receptor interactions.

1.2.3 Enzyme-Responsive Peptide Self-Assembly

Enzymes are attractive targets for the design of stimuli-responsive peptide self-assembly. There are many types of peptide substrates targeted for enzymatic cleavage or modification. This approach enables targeted delivery of therapeutics to certain disease tissues where an enzyme is overexpressed at the desired site of drug action. For example, matrix metalloproteinases (MMPs), cysteine cathepsins, and alkaline phosphatases have been identified in diseases such as cancer, arthritis, and atherosclerosis.[37] Many peptide-based assemblies have been designed to release drugs by enzymatic triggers. These site-specific deliveries occur through either direct cleavage of the covalent bond between the peptides and cargo or by inducing assembly/disassembly of the nanostructure. Provided with the high enzymatic specificity, the non-specific release to healthy tissues can be minimized. Furthermore, through a modular design approach, the substrate can be easily changed to peptides sequences that can target different enzymes in various diseases.

Kalafatovic et al.[38] designed an MMP-9 specific peptide which self-assembled into spherical aggregates. The hydrophilic domain of the peptides was cleaved at the site with overexpression of MMP-9, leading to transformation of spherical micelles to nanofibers (**Fig. 1.7A**). A sustained release of drugs is achieved due to the formation of nanofibers with increased hydrophobicity. This approach opens up the possibility of using enzyme responsive peptide self-assembly for controlled drug delivery. Huang et al.[39] designed a phosphatase-instructed co-assembling nanostructure. A photothermal therapeutic agent ICG co-assembled with an alkaline phosphatase (ALP)-responsive peptide to form micelles (**Fig. 1.7B**). The micelles showed enhanced permeability and retention (EPR) effect and limited non-specific uptake by the reticuloendothelial system (RES)-rich organs. At the disease site, micelles are transformed into nanofibers as triggered by the ALP to remove the phosphate group and therapeutic ICG. Wu et al.[40] reported a peptide amphiphile which contains a hydrophobic drug denoted and a ALP responsive peptide domain (**Fig. 1.7C**). The cleavage of phosphate groups highly increased the hydrophobicity of the peptide amphiphile and triggered self-assembly into nanogel. The hydrogel promoted sustained release of free drug. Peptide-based sensors are also achieved by enzyme instructed disassembly. Li et al.[41] designed C-3 peptides that selectively detect furin in a live cell (**Fig. 1.7D**). The peptide is composed of three moieties: a furin responsive hydrophilic moiety RVRR, a hydrophobic moiety FFF and imaging moiety NBD. The C-3 probe was “turned-off” as self-assembly occurs into micelles. The RVRR provided positive charges for cell uptake. The cleavage of the RVRR moiety by intracellular furin causes the disassembly of micelles and subsequently turns on fluorescence. The cleavage process occurs rapidly within 5 mins, which enables a rapid and specific detection of furin overexpressing cells.

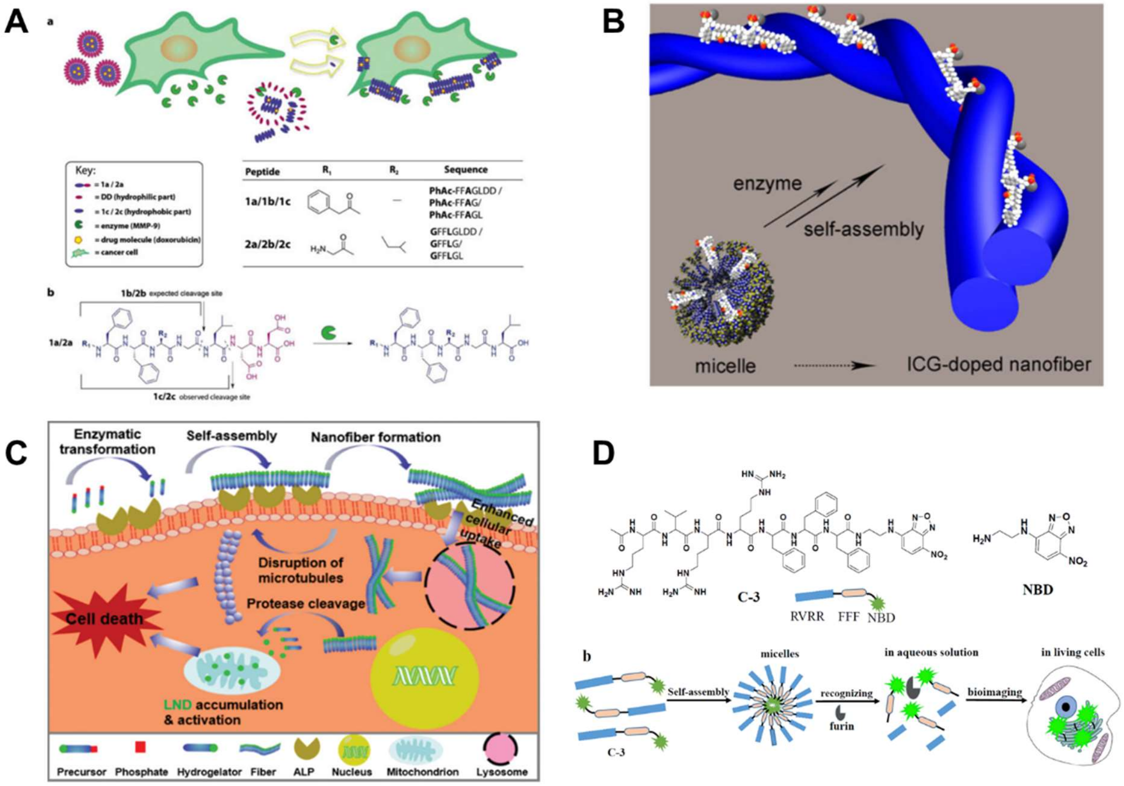

Figure 1.7 (A) MMP-9 triggered micelle to fiber transition. (a) Schematic representation of micelle-to-fiber transition in the presence of cancer cells due to MMP-9 secretion, followed by entrapment of doxorubicin in fibrillar structures, which act as less mobile depots of the anticancer drug. (b) Chemical structure of the MMP-9 responsive peptide amphiphiles. (B) Schematic Enzyme-triggered self-assembly of ICG-doped nanofiber conversion of micelles to nanofiber via enzyme-catalyzed dephosphorylation. (C) Schematic illustration of the self-delivery system of LND–GFFpY for the selective killing of cancer cells. (D) The molecular structures of C-3 and NBD. Schematic illustrations of self-assembly process and furin detection of C-3.

1.3 References

1. Lam, K. S.; Salmon, S. E.; Hersh, E. M.; Hruby, V. J.; Kazmierski, W. M.; Knapp, R. J., A new type of synthetic peptide library for identifying ligand-binding activity. *Nature* **1991,** *354* (6348), 82-84.
2. Guyon, L.; Lepeltier, E.; Passirani, C., Self-assembly of peptide-based nanostructures: Synthesis and biological activity. *Nano Res.* **2018,** *11* (5), 2315-2335.
3. Deng, Y.; Zhan, W.; Liang, G., Intracellular Self‐Assembly of Peptide Conjugates for Tumor Imaging and Therapy. *Adv. Healthc. Mater.* **2021,** *10* (1), 2001211.
4. Wu, E. C.; Zhang, S.; Hauser, C. A., Self‐assembling peptides as cell‐interactive scaffolds. *Adv. Func. Mater.* **2012,** *22* (3), 456-468.
5. Fan, T.; Yu, X.; Shen, B.; Sun, L., Peptide self-assembled nanostructures for drug delivery applications. *J. Nanomater.* **2017,** *2017*.
6. Lian, Z.; Ji, T., Functional peptide-based drug delivery systems. *J. Mater. Chem. B* **2020,** *8* (31), 6517-6529.
7. Luo, Z.; Yue, Y.; Zhang, Y.; Yuan, X.; Gong, J.; Wang, L.; He, B.; Liu, Z.; Sun, Y.; Liu, J., Designer D-form self-assembling peptide nanofiber scaffolds for 3-dimensional cell cultures. *Biomaterials* **2013,** *34* (21), 4902-4913.
8. Chen, W.; Yang, S.; Li, S.; Lang, J. C.; Mao, C.; Kroll, P.; Tang, L.; Dong, H., Self-assembled peptide nanofibers display natural antimicrobial peptides to selectively kill bacteria without compromising cytocompatibility. *ACS Appl. Mater. Interfaces* **2019,** *11* (32), 28681-28689.
9. Shen, Z.; Guo, Z.; Zhou, L.; Wang, Y.; Zhang, J.; Hu, J.; Zhang, Y., Biomembrane induced in situ self-assembly of peptide with enhanced antimicrobial activity. *Biomater. Sci.* **2020,** *8* (7), 2031-2039.
10. Zhang, X.-Y.; Liu, C.; Fan, P.-S.; Zhang, X.-H.; Hou, D.-Y.; Wang, J.-Q.; Yang, H.; Wang, H.; Qiao, Z.-Y., Skin-like wound dressings with on-demand administration based on in situ peptide self-assembly for skin regeneration. *J. Mater. Chem. B* **2022,** *10* (19), 3624-3636.
11. Han, K.; Zhang, W. Y.; Zhang, J.; Lei, Q.; Wang, S. B.; Liu, J. W.; Zhang, X. Z.; Han, H. Y., Acidity‐triggered tumor‐targeted chimeric peptide for enhanced intra‐nuclear photodynamic therapy. *Adv. Func. Mater.* **2016,** *26* (24), 4351-4361.
12. Chen, S.; Lei, Q.; Li, S.-Y.; Qin, S.-Y.; Jia, H.-Z.; Cheng, Y.-J.; Zhang, X.-Z., Fabrication of dual responsive co-delivery system based on three-armed peptides for tumor therapy. *Biomaterials* **2016,** *92*, 25-35.
13. Aida, T.; Meijer, E. W.; Stupp, S. I., Functional Supramolecular Polymers. *Science* **2012,** *335* (6070), 813-817.
14. Meziani, M. J.; Sun, Y.-P., Protein-conjugated nanoparticles from rapid expansion of supercritical fluid solution into aqueous solution. *J. Am. Chem. Soc.* **2003,** *125* (26), 8015-8018.
15. Pauling, L.; Corey, R. B., The pleated sheet, a new layer configuration of polypeptide chains. *Proc. Natl. Acad. Sci. U.S.A* **1951,** *37* (5), 251-256.
16. Chiti, F.; Dobson, C. M., Protein misfolding, functional amyloid, and human disease. *Annu. Rev. Biochem.* **2006,** *75* (1), 333-366.

17. Moore, A. N.; Hartgerink, J. D., Self-assembling multidomain peptide nanofibers for delivery of bioactive molecules and tissue regeneration. *Acc. Chem. Res.* **2017,** *50* (4), 714-722.
18. Caplan, M. R.; Schwartzfarb, E. M.; Zhang, S.; Kamm, R. D.; Lauffenburger, D. A., Control of self-assembling oligopeptide matrix formation through systematic variation of amino acid sequence. *Biomaterials* **2002,** *23* (1), 219-227.
19. Dong, H.; Paramonov, S. E.; Aulisa, L.; Bakota, E. L.; Hartgerink, J. D., Self-assembly of multidomain peptides: balancing molecular frustration controls conformation and nanostructure. *J. Am. Chem. Soc.* **2007,** *129* (41), 12468-12472.
20. Hong, Y.; Pritzker, M. D.; Legge, R. L.; Chen, P., Effect of NaCl and peptide concentration on the self-assembly of an ionic-complementary peptide EAK16-II. *Colloids Surf. B* **2005,** *46* (3), 152-161.
21. Yu, Y. B., Coiled-coils: stability, specificity, and drug delivery potential. *Adv. Drug Deliv. Rev.* **2002,** *54* (8), 1113-1129.
22. Oheix, E.; Peacock, A. F. A., De Novo Design of Metallocoiled Coils. In *Reference Module in Chemistry, Molecular Sciences and Chemical Engineering*, 2015.
23. Harbury, P. B.; Zhang, T.; Kim, P. S.; Alber, T., A switch between two-, three-, and four-stranded coiled coils in GCN4 leucine zipper mutants. *Science* **1993,** *262* (5138), 1401-1407.
24. Gonzalez, L.; Woolfson, D. N.; Alber, T., Buried polar residues and structural specificity in the GCN4 leucine zipper. *Nat. Struct. Biol.* **1996,** *3* (12), 1011-1018.
25. Papapostolou, D.; Smith, A. M.; Atkins, E. D.; Oliver, S. J.; Ryadnov, M. G.; Serpell, L. C.; Woolfson, D. N., Engineering nanoscale order into a designed protein fiber. *Proc. Natl. Acad. Sci. U.S.A* **2007,** *104* (26), 10853-10858.
26. Behanna, H. A.; Donners, J. J.; Gordon, A. C.; Stupp, S. I., Coassembly of amphiphiles with opposite peptide polarities into nanofibers. *J. Am. Chem. Soc.* **2005,** *127* (4), 1193-1200.
27. Hartgerink, J. D.; Beniash, E.; Stupp, S. I., Self-assembly and mineralization of peptide-amphiphile nanofibers. *Science* **2001,** *294* (5547), 1684-1688.
28. Li, Z.; Zhu, Y.; Matson, J. B., pH-Responsive Self-Assembling Peptide-Based Biomaterials: Designs and Applications. *ACS Appl. Bio Mater.* **2022**.
29. Zimenkov, Y.; Dublin, S. N.; Ni, R.; Tu, R. S.; Breedveld, V.; Apkarian, R. P.; Conticello, V. P., Rational design of a reversible pH-responsive switch for peptide self-assembly. *J. Am. Chem. Soc.* **2006,** *128* (21), 6770-6771.
30. Wang, T.-W.; Yeh, C.-W.; Kuan, C.-H.; Wang, L.-W.; Chen, L.-H.; Wu, H.-C.; Sun, J.-S., Tailored design of multifunctional and programmable pH-responsive self-assembling polypeptides as drug delivery nanocarrier for cancer therapy. *Acta Biomater.* **2017,** *58*, 54-66.
31. He, W.; Yan, J.; Jiang, W.; Li, S.; Qu, Y.; Niu, F.; Yan, Y.; Sui, F.; Wang, S.; Zhou, Y.; Jin, L.; Li, Y.; Ji, M.; Ma, P. X.; Liu, M.; Lu, W.; Hou, P., Peptide-Induced Self-Assembly of Therapeutics into a Well-Defined Nanoshell with Tumor-Triggered Shape and Charge Switch. *Chem. Mater.* **2018,** *30* (20), 7034-7046.

32. Raza, F.; Zhu, Y.; Chen, L.; You, X.; Zhang, J.; Khan, A.; Khan, M. W.; Hasnat, M.; Zafar, H.; Wu, J., Paclitaxel-loaded pH responsive hydrogel based on self-assembled peptides for tumor targeting. *Biomater. Sci.* **2019,** *7* (5), 2023-2036.
33. Nam, S. H.; Jang, J.; Cheon, D. H.; Chong, S.-E.; Ahn, J. H.; Hyun, S.; Yu, J.; Lee, Y., pH-Activatable cell penetrating peptide dimers for potent delivery of anticancer drug to triple-negative breast cancer. *J Control Release* **2021,** *330*, 898-906.
34. Liang, P.; Zheng, J.; Dai, S.; Wang, J.; Zhang, Z.; Kang, T.; Quan, C., pH triggered re-assembly of nanosphere to nanofiber: The role of peptide conformational change for enhanced cancer therapy. *J Control Release* **2017,** *260*, 22-31.
35. Zhang, X. H.; Cheng, D. B.; Ji, L.; An, H. W.; Wang, D.; Yang, Z. X.; Chen, H.; Qiao, Z. Y.; Wang, H., Photothermal-Promoted Morphology Transformation in Vivo Monitored by Photoacoustic Imaging. *Nano Lett.* **2020,** *20* (2), 1286-1295.
36. Chen, W.; Li, S.; Lang, J. C.; Chang, Y.; Pan, Z.; Kroll, P.; Sun, X.; Tang, L.; Dong, H., Combined Tumor Environment Triggered Self-Assembling Peptide Nanofibers and Inducible Multivalent Ligand Display for Cancer Cell Targeting with Enhanced Sensitivity and Specificity. *Small* **2020,** *16* (38), e2002780.
37. Mu, J.; Lin, J.; Huang, P.; Chen, X., Development of endogenous enzyme-responsive nanomaterials for theranostics. *Chem. Soc. Rev.* **2018,** *47* (15), 5554-5573.
38. Kalafatovic, D.; Nobis, M.; Son, J.; Anderson, K. I.; Ulijn, R. V., MMP-9 triggered self-assembly of doxorubicin nanofiber depots halts tumor growth. *Biomaterials* **2016,** *98*, 192-202.
39. Huang, P.; Gao, Y.; Lin, J.; Hu, H.; Liao, H. S.; Yan, X.; Tang, Y.; Jin, A.; Song, J.; Niu, G.; Zhang, G.; Horkay, F.; Chen, X., Tumor-Specific Formation of Enzyme-Instructed Supramolecular Self-Assemblies as Cancer Theranostics. *ACS Nano* **2015,** *9* (10), 9517-27.
40. Wu, C.; Liu, J.; Tang, X.; Zhai, Z.; Xu, K.; Zhong, W., An enzyme-assisted self-delivery system of lonidamine-peptide conjugates for selectively killing cancer cells. *Chem. Commun.* **2019,** *55* (98), 14852-14855.
41. Li, X.; Cao, C.; Wei, P.; Xu, M.; Liu, Z.; Liu, L.; Zhong, Y.; Li, R.; Zhou, Y.; Yi, T., Self-Assembly of Amphiphilic Peptides for Recognizing High Furin-Expressing Cancer Cells. *ACS Appl. Mater. Interfaces* **2019,** *11* (13), 12327-12334.

Chapter 2. Reduction-Responsive Peptide Self-Assembly*

2.1 Introduction

The development of nanomaterials has offered tremendous promise and opportunity for nanocarrier-based cancer therapy which dramatically reduces the toxicity effects of chemotherapeutic drugs on healthy tissues and cells.[1-4] More recently, targeted delivery of cancer therapeutics to diseased sites has attracted great attention to promote the clinical application of functional nanocarriers. Various tumor physiology triggers, such as pH,[5-6] enzymes,[7-8] reduction,[9-10] and hypoxia,[11-12] have been utilized to activate the nanomaterials at the tumor sites to improve cell uptake and subsequent drug release.

Trigger-responsive nanomaterials can be divided into two classes depending on their sites of activation at the cellular level. One is designed to respond to the physiological triggers in the extracellular matrix where the nanomaterials become highly cell membrane permeable for enhanced cell uptake.[13-15] The second becomes activated only when they are internalized inside cells where nanomaterials are degraded or disassembled to release the therapeutic payloads.[16-17] Both mechanisms demonstrate great potential in selectively targeting cancer therapeutics to tumor tissues and cells for improved therapeutic effects. Particularly, for trigger-responsive membrane active nanoparticles, efforts have been made to modify the surface chemistry of the drug delivery systems by incorporating membrane pro-active components, such as protected cell penetrating peptides (CPPs).[18-20] The membrane

---

[*] This chapter is based on Su Yang et al. Design and fabrication of reduction-sensitive cell penetrating nanofibers for enhanced drug efficacy. *J. Mater. Chem. B*, **2018**, *6(44)*, 7179-7184. Some sections were rearranged for continuity.

activity of CPP functionalized system is greatly enhanced upon CPP activation in the presence of tumor-specific triggers leading to improved cell uptake and drug efficacy. However, the fabrication of such systems often involves the use of multi-component building blocks and may require stringent quality control for both the synthesis and formulation process. Therefore, it is desirable to develop new design principles and chemical methods to generate trigger-responsive materials that are structurally simple, easy to fabricate and modulate, and highly membrane penetrable for effective cancer treatment.

We have previously reported a membrane-active peptide nanofiber based on the self-assembly of multidomain peptides (MDPs) with a general sequence of $K_x(QW)_y$ where x represents the numbers of lysine (K) residues and y represents the numbers of alternating glutamine (Q) and tryptophan (W) repeating units.[21-22] The alternating polar and nonpolar residue pattern provides the driving force for β-sheet formation and their packing into supramolecular nanofibers while the lysine residues are displayed at the fiber surface to interact with the cell membrane. We previously studied the self-assembly process of MDPs and showed the significance of the interplay between peptide self-assembly and cell penetrating activity. Nanofibers composed of $K_{10}(QW)_6$ showed a good balance between supramolecular packing and charge domain flexibility which is a critical factor for achieving optimal cell uptake and transport of membrane-impermeable molecules. In this work, we will utilize the unique membrane activity of these self-assembled nanofibers and fabricate a trigger-responsive cell penetrating nanofiber (TR-CPN) using integrated MDPs where each individual component is amenable to change to tune the nanostructure and biological activity for targeted cancer therapy.

2.2 Result and Discussion

2.2.1 Peptide Design

Jiang et al. demonstrated the design of fusion activatable CPPs in which enzymatic cleavage of a β-hairpin linker achieved between the polycationic and polyanionic domain released the polycationic CPP portion and delivery cargo intracellular.[14] The supramolecular assembly of β-sheet peptides provides an alternative strategy to control the charge density of the polyanionic domain, and eventually tune their membrane activity. Collier's group recently reported the effect of correlation between surface charges peptide nanofibers and eliciting antibody production.[23] The study suggested positively charged surface can augment cell uptake of antigen presenting cells while a negatively charged surface prevented cell uptake. Cui and Azevedo recently established an enzymatic activation peptide self-assembly transformation from nanofibers to spherical micelles.[13] We will take advantage of the existing discovery about the triggered cell penetrating peptide nanomaterial, we incorporate both positive and negative surface design parameters into a single peptide design to fabricate smart, tumor-responsive cell penetrating nanomaterials.

As a proof-of-concept, in this work, we focus on the design of reductive microenvironment responsive TR-CPNs which have been used to differentiate tumor tissues and cells from normal ones.[24-26] **Fig. 2.1** shows the chemical structure of the reduction-sensitive MDP with a sequence of $K_{10}(QW)_6(SS)E_5$, abbreviated as K(SS)E where SS refers to the reduction sensitive linker which was synthesized according to the procedure published by Yang et al.[27] and can be readily programmed in the solid phase peptide synthesis. Five glutamic acid residues were conjugated on the C-terminus through the SS linker to have intermolecular ionic interactions with the lysine residues on N-terminus. Upon self-assembly, the E5 and K10 domains are bonded along the fiber axis by the intrinsic packing order of the MDPs within the supramolecular assembly (**Fig. 2.1**). With the interaction of polyanionic (E5) and polycationic (K10), the positive charges are partially shielded, therefore the membrane activity of the nanofiber is reduced. In the tumor reduction environment, the E5 domain was removed by the cleavage of the SS linker, enhanced positive charges exposure at the fiber surface will increase and the membrane activity of the assembly can be retrieved.

Based on our results, five glutamic acids are sufficient to shield the positive charge of lysine residues and allow selectivity cell penetration under the reductive condition. However, the number of glutamic acids can be varied to tune the nanostructure and membrane activity as needed. A control MDP (**Fig. 2.1**) was synthesized by replacing the SS moiety with a non-responsive carbon chain with the same length and the sequence is referred to as $K_{10}(QW)_6(C6)E_5$, abbreviated as K(C6)E. Although current peptides are designed to establish reduction-sensitive, the design principle can be easily applied to other kinds of TR-CPNs, such as enzymatic responsive CPNs by integrating oligopeptide substrates for various tumor-specific enzymes in the MDPs and pH-responsive by employing a pH-sensitive covalent bond in the MDPs for targeted cancer therapeutics and imaging delivery.

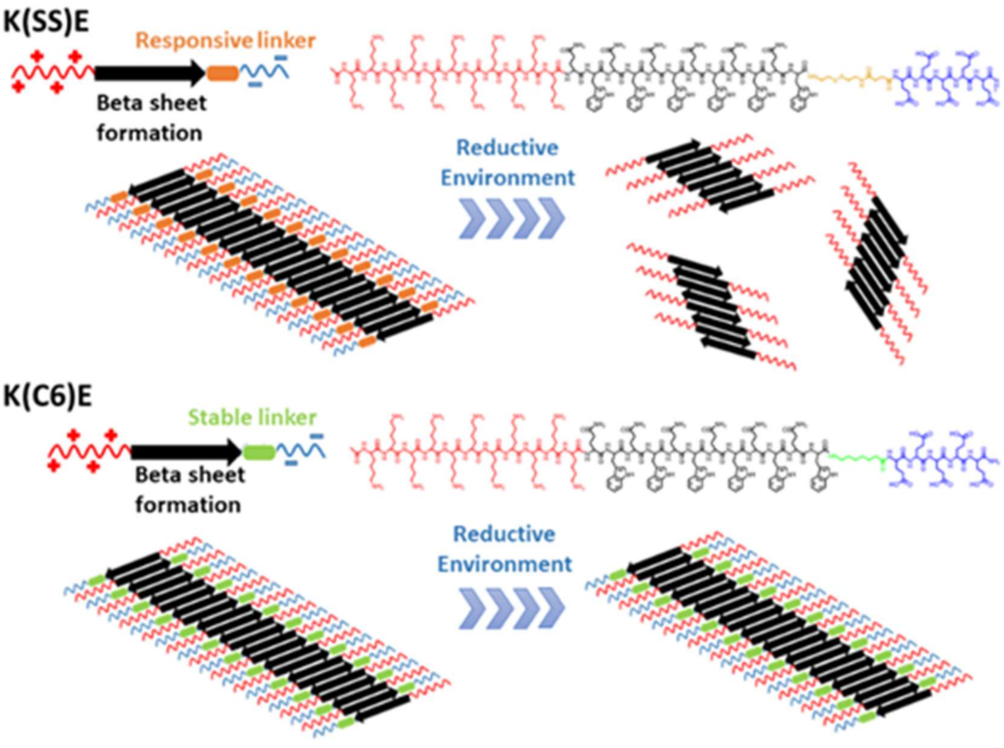

Figure 2.1 Color-coded chemical structure and cartoon representation of reduction-sensitive and non-sensitive MDPs and their self-assembly into supramolecular nanofibers. Red: K10 as the polycationic domain; black: (QW)6 to drive the supramolecular packing of the b-sheet nanofibers; blue: E5 as the polyanionic domain; orange: reduction-sensitive linker; green: non-sensitive linker.

2.2.2 Molecular and Supramolecular Structural Characterization

K(SS)E and K(C6)E were designed to undergo spontaneous self-assembly into β-sheet nanofibers in Tris buffer (pH = 7.4, 20 mM). To monitor the assembly behavior in solution, the critical assembly concentrations (CACs) of both peptides were determined using a previously established method where the fluorescence intensity of the tryptophan in the peptides was measured as a function of peptide concentration.[28-29] Due to the packing of β-sheets, the aromatic tryptophan residues are in spatial proximity relative to each in the self-assembling hydrophobic core, the fluorescence intensity falls off the linear range at the CAC, it could be read from the x-axis of cross point between linear and quenched range (**Fig. 2.2**).

The determined CACs for K(SS)E and K(C6)E are 9.1 μM and 7.9 μM respectively. For all the following structural characterization and biological activity measurements, the peptide concentrations were designed to be above their CACs to consistent forming supramolecular nanofibers.

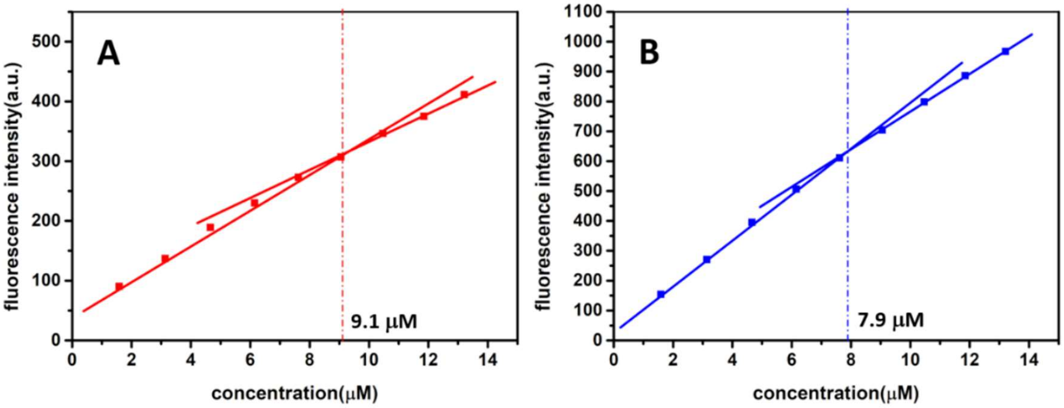

Figure 2.2 CAC determination through fluorescence measurements of peptides as a function of concentration in Tris buffer (20 mM, pH 7.4) (A) K(SS)E and (B) K(C6)E

To study the response of the peptides toward the reductive environment, the self-assembled peptides were treated in Tris buffer (pH 7.4) were treated with a reducing agent dithiodithreitol (DTT) and resulted peptide was analyzed by mass spectrometry. The DTT concentration used in the solution study was based on clinical studies of glutathione levels in human tumors that showed a typical range from 0.5 to 3 mM, for example, brain tumors along with several other cancers.[30] The near complete degradation of K(SS)E was confirmed by analytical HPLC where a peak shift of the DTT-treated peptide was clearly observed compared to the peptide before DTT addition (**Fig. 2.3A**). Based on the MALDI results (**Fig.2.3B**), K(SS)E was completely degraded upon the addition of DTT leading to a peptide fragment of reduced molecular weight at 3291 while the original peptide was not detected. The control peptide, K(C6)E, remained intact upon DTT treatment (**Fig. 2.3C**).

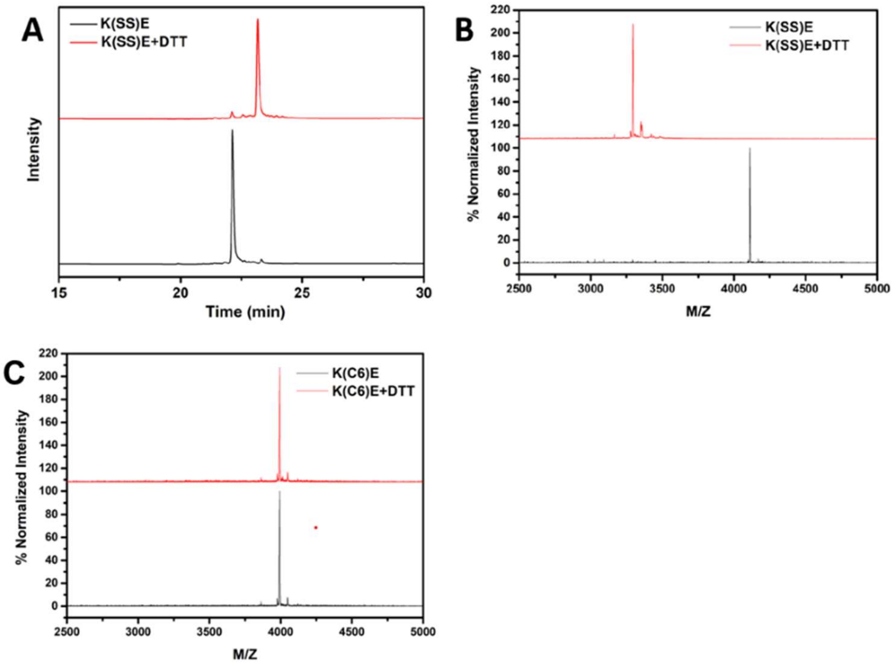

Figure 2.3 (A) HPLC of K(SS)E incubated with and without DTT. (B) MALDI spectra of K(SS)E incubated with and without DTT (B) MALDI spectra of K(C6)E incubated with and without DTT

Next, the molecular secondary structures of the peptides were studied by circular dichroism (CD) spectroscopy in the presence of DTT. **Fig. 2.4A** shows the CD spectra of K(SS)E before and after DTT treatment for 1 h at 37 °C. Before adding DTT, K(SS)E adopted a predominant β-sheet structure characterized by the minimum peak at 213 nm. Upon the addition of DTT, a new peak at 208 nm appeared suggesting part of the β-sheets transitioned to α-helices. As mentioned above, E5 is used to stabilize the packing by electrostatic interactions with K10. As shown in the previous study, the sequence $K_{10}(QW)_6$ couldn't for β-sheet structure without a property desalting process. The increased helical content has presumably suggested the removal of the E5 domain. The isolated polylysine becomes more flexible to form α-helices. But there is a possibility that most of the cleaved E5 might still be attached to the positively charged fiber surface. Therefore, we performed zeta-potential measurements to characterize the surface charges changing upon DTT treatment. To minimize potential structural reorganization of the nanofibers upon exposure to the electric field, we took the average of the zeta potential readings from the first three measurements of each sample for a fair comparison. As shown in **Fig. 2.4**, the zeta potential of the self-assembled peptides nanofiber increased from 17.5 mV to 25 mV upon the addition of DTT. The result demonstrated that the positive charges on the nanofiber surface were successfully recovered upon the cleavage of a disulfide bond. The cleaved product has a comparable zeta potential value with the control peptide $K_{10}(QW)_6$ (28 mV). This result was consistent with the cell-based assay results as will be discussed later. The cell penetrating activity and therapeutic delivery efficacy were dramatically enhanced for the responsive peptide compared with the non-responsive peptide in HeLa cell culture. The results indicated residual E5 won't cause a major issue for peptide nanofiber to interact with the cell membrane for drug transport.

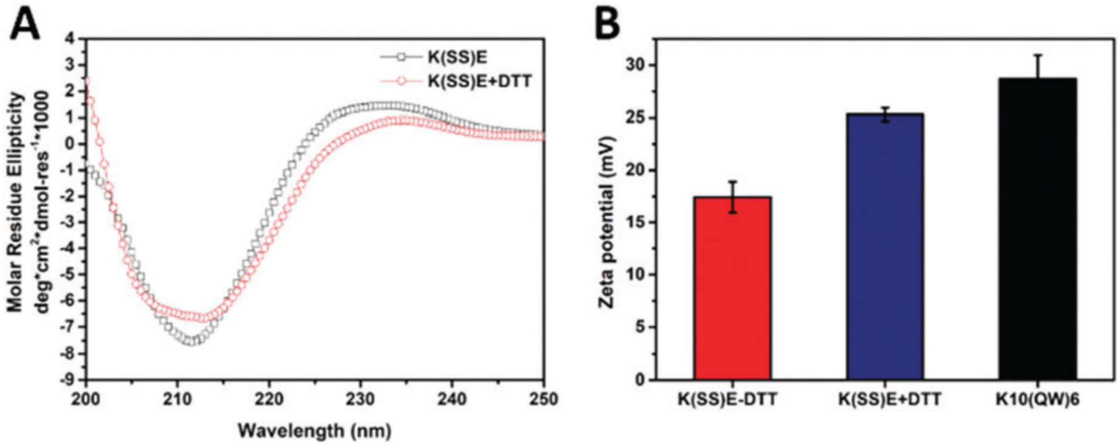

Figure 2.4 (A) CD spectra of K(SS)E in the presence and absence of DTT. (B) Zeta potential of K(SS)E upon DTT treatment. Peptide concentration: 100 μM in Tris buffer (20 mM, pH = 7.4). DTT concentration: 1 mM in Tris buffer (20 mM, pH = 7.4).

To compare with K(SS)E, the CD spectrum of the nonresponsive peptide, K(C6)E with and without DTT treatment was also performed, but there was essentially change shown upon DTT addition (**Fig. 2.5**). The result suggested the achievement of secondary structure change is relay on the cleavage of the SS linker and change recover, instead of just non-specific bonding with DTT. But it is also very limited information that CD spectroscopy only provides information about the global secondary structures, so TEM was employed to study the actual nanostructure change based on the microlevel.

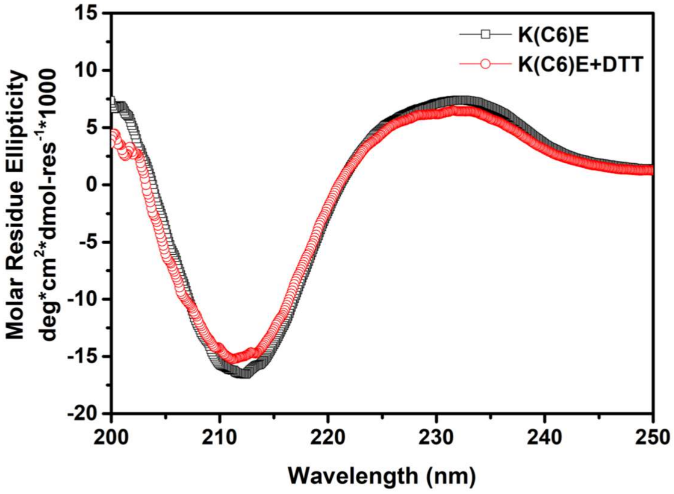

Figure 2.5 CD spectra of K(C6)E treat with and without DTT. Peptide concentration: 100 μM in Tris buffer (20 mM, pH =7.4), DTT concentration: 1 mM in Tris buffer (20 mM, pH =7.4).

The self-assembled nanostructure change of the responsive peptide upon DTT treatment was examined by negatively stained transmission electron microscopy (TEM). Without DTT treatment, the peptides form nanofibers of relatively defined morphology with minimum twisting and deformation (**Fig. 2.6 A**). A statistical measurement based on a total of one hundred randomly selected nanofibers yielded an average length of 80 nm and a uniform diameter at 5 nm for self-assembled K(SS)E (**Fig. 2.6C**). With the treatment of DTT, the average length of nanofiber was dramatically reduced to 50 nm and a large fraction of defects was observed on the nanofibers after reduction (**Fig. 2.6B and 2.6D**). The nanostructure change of the peptide self-assembly was correlated to the change of the molecular secondary structures shown on the CD spectra. Upon removal of the E5 domain, the exposure of cationic domains of K10 generated repletion between each peptide chain and compromise the molecular packing of the β-sheet nanofibers. This effect leads to local disassembly in some areas and overall fiber length reduction.

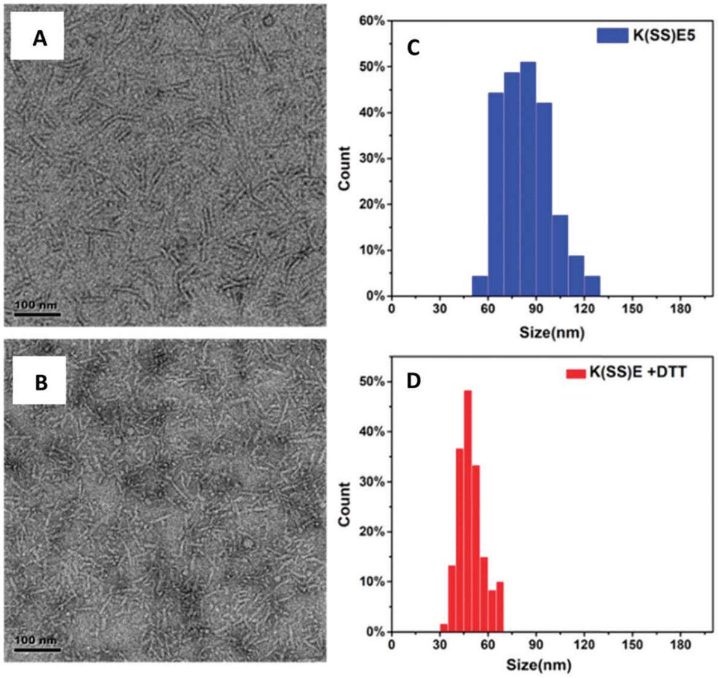

Figure 2.6 TEM images of the nanofibers formed by K(SS)E incubated without (A) and with (B) DTT. Statistical measurements of length and length distribution of K(SS)E nanofibers without (C) and with (D) DTT based on a total number of 100 fibers. Scale bar: 100 nm.

The nanostructure of self-assembled K(C6)E was also characterized in the presence and absence of DTT to make a comparison. As shown in **Fig. 2.7**, the nanofiber form by K(C6)E was not affected by the treatment of DTT, the size and morphology stays the same in both groups. Based on the statistical size analysis, the average lengths of the K(C6)E nanofibers were significantly shorter than those of K(SS)E before reduction, yet comparable to the reduced K(SS)E nanofiber. We speculate that the morphological difference between K(C6)E and K(SS)E before reduction is mostly due to the chemical nature of the linker used to connect the anionic domain and self-assemble domain. The SS linker has two additional amide groups that could also donate to the intermolecular hydrogen bonding network along the fiber axis. Instead, the hexyl group in the C6 linker is more flexible and likely to cause steric hindrance and break the continuous hydrogen bond between peptide subunits along the fiber axis. Although K(C6)E formed shorted nanofibers, it is still not membrane-active presumably because of the charge screening effect. In our previous publication, [21] we explored the cell penetrating activity of nanofibers with different lengths but relatively comparable cationic charge density. We found that with a given surface charge density, shorter nanofibers showed higher membrane activity. Combining the results of both studies, we believe that the membrane activity of the reduced K(SS)E nanofibers got enhanced by a combined effect of charge and morphology.

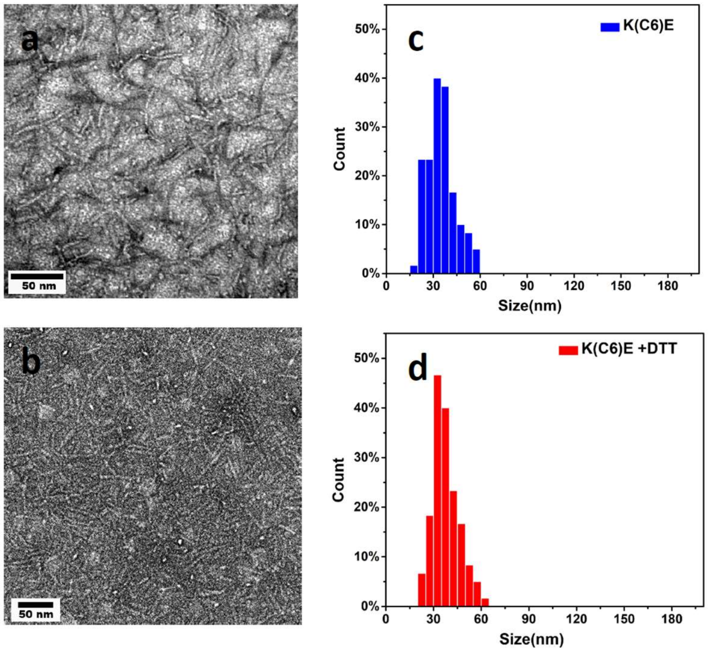

Figure 2.7 TEM images of the nanofibers formed by K(C6)E incubated without (A) and with (B) DTT. Statistical measurements of length and length distribution of K(SS)E nanofibers without (C) and with (D) DTT based on a total number of 100 fibers.

2.2.3 *In Vitro* Study of the Membrane Activity and Therapeutic Delivery Efficacy

The membrane activity of K(SS)E under the reductive condition was investigated *in vitro* by using HeLa cells as a model cancer cell line. Most cancer cells are known to produce much higher concentrations of glutathione (GT) in both the cytoplasm and extracellular matrix which has been widely used as a tumor-specific trigger to achieve selective delivery of cancer therapeutics.[31-32] For all the *in vitro* assays, no exogenous reducing agents were added because the 0.5-1.0 mM free thiol groups were present in the Hela culture medium. The concentration was determined by Elman's test. In this experiment, we investigated and compared the cell uptake of K(SS)E and K(C6)E by monitoring the intracellular fluorescence of fluorescein (FITC)-labeled peptides at 2 h and 24 h time points through confocal laser scanning microscopy (CLSM) and flow cytometry. A marked difference in peptide cell uptake was observed upon 2 h of incubation of the peptides with HeLa cells. K(SS)E was internalized to a much larger extent than K(C6)E as demonstrated by both the CLSM and flow cytometry results (**Fig. 2.8A and B**).

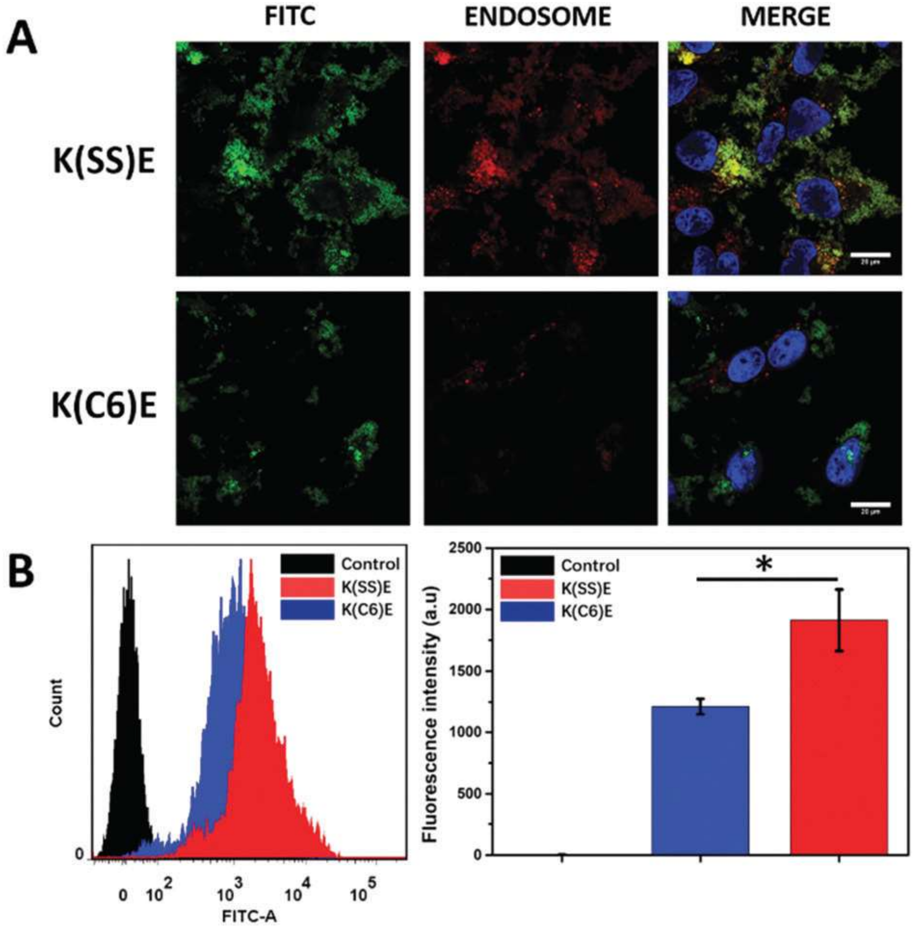

Figure 2.8 (A) Confocal images of the cell uptake of FITC-labeled K(SS)E and K(C6)E upon incubation with HeLa cells for 2 h. (B) Cell uptake of K(SS)E and K(C6)E as measured by flow cytometry. Scale bar: 20 μm. Peptide concentration: 16 μM. Statistically significant differences are indicated by $^*p \leq 0.05$.

Extended incubation promoted higher uptake of the control peptide (**Fig. 2.9**), but the K(SS)E still showed higher fluorescence intensity than that of K(C6)E. In this work, the rational design of peptide is targeted to trigger by the extracellular GT of tumor tissues and becomes membrane active in the extracellular matrix upon removal of the capping domain of E5. However, we cannot exclude the possibility of other routes in which the peptide nanofibers may first attach to the cell membrane because the peptide is still positively charged after being screened (**Fig. 2.4B**) the peptide could be cleaved by leaked intracellular GT to be activated the further increasing cell uptake. Regardless of the passway of cleavage and activation, tumor tissues are known to express much higher amounts of GT than normal tissues, which are supposed to provide enough GT for SS liner reduction. The nanofibers composed of reduction-sensitive K(SS)E are highly promising nanocarriers for targeted cancer therapy.

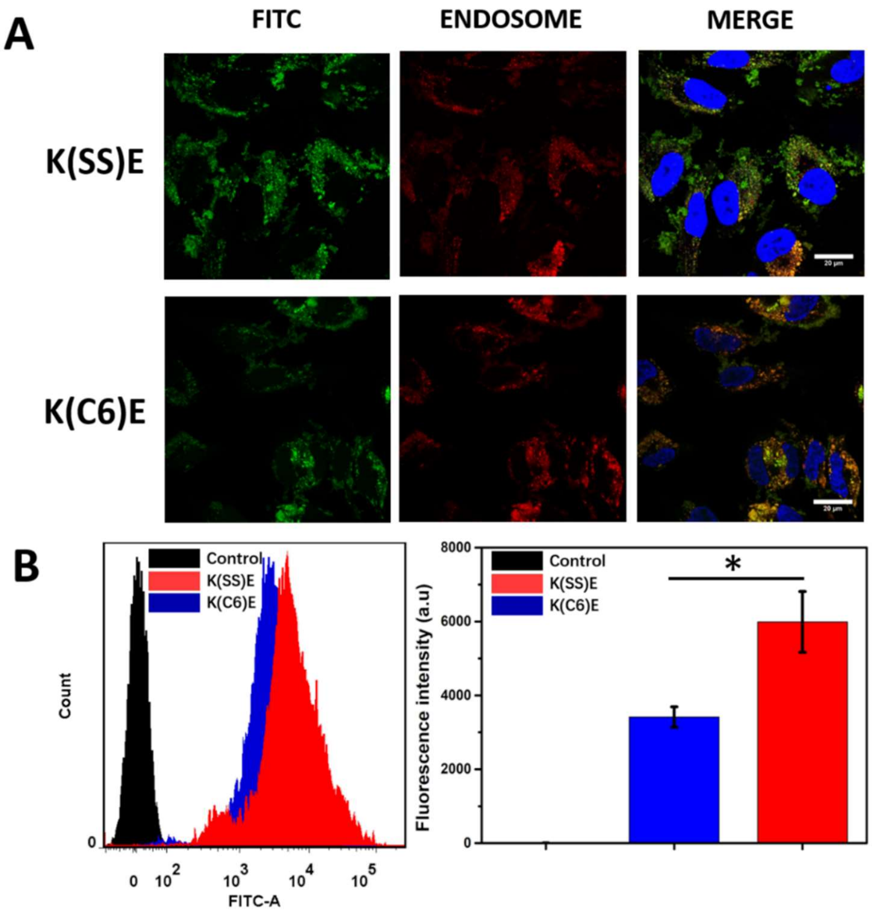

Figure 2.9 (A)Cell uptake of FITC-labeled K(SS)E and K(C6)E upon incubation with HeLa cells for 24 hs. (B) Cellular uptake of K(SS)E and K(C6)E evaluated by flow cytometry. Scale bar: 20 μm. Statistically significant differences are indicated by $*p \leq 0.05$.

To further validate the reduction-sensitive nanofiber platform for targeted therapeutics delivery, we performed an *in vitro* cytotoxicity assay using a model anticancer drug membrane impermeable doxorubicin (DOX, in the form of HCl salt). The model drug was co-incubated with three different nanofibers in HeLa cell culture. According to our previous work, there are minimum physical or chemical interactions occurred between DOX and the peptides. The idea of this study is the peptide could interact with the cell membrane based on their positive changed surface, the interaction not only allows the peptide to penetrate across the cell membrane but also perturbated the cell membrane to improve the permeability. The ability of peptide nanofiber perturbated the cell membrane could be quantified by an increase in antitumor drug cytotoxicity increasing. Three peptides used in the study include (1) K(SS)E as a reduction-sensitive formulation, (2) K(C6)E as a non-responsive and membrane inactive formulation and (3) K10(QW)6 (abbreviated as K10) as a non-selective but membrane-active formulation. The peptide concentration in the cell culture medium was fixed at 16 μM which is above their CACs, this concentration has been proved in our previous study to successfully achieve the membrane perturbation. And the DOX concentrations span from 0.05 μM to 4 μM. Cell viability was evaluated using the CCK-8 assay and the IC(50) values of DOX were calculated for each formulation through the sigmoidal fitting of the cell viability results (**Fig. 2.10**).

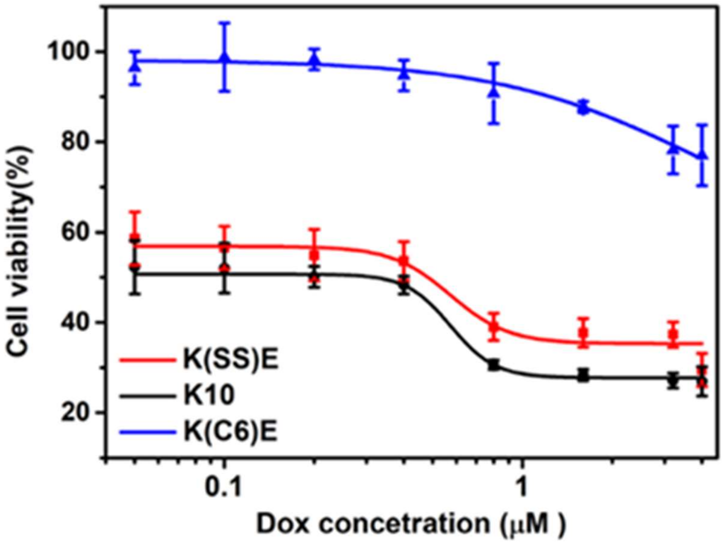

Figure 2.10 HeLa cell viability upon 24 hs of incubation with DOX in the presentence of K(SS)E, K(C6)E and K10. All three peptide concentrations are fixed at 16 μM and DOX concentrations span from 0.05 to 4 μM.

The IC(50) value of DOX alone is determined at 2.7 mM (**Fig. 2.11**), which was reduced to 0.48 μM upon the addition of K(SS)E, which suggested the improvement of drug efficacy, the result correlated to the increase cell uptake. It should be noted that the IC(50) value of K(SS)E is slightly higher than that of K10 (at 0.3 μM). This is presumably caused by the partially electronic static bonding of the cleaved residual glutamic acids. The attachment partially shielded the membrane interaction of the nanofibers, therefore resulting in slightly diminishing the cell penetrating activity. K(C6)E, as a non-responsive formulation and negative control, mimicked the behavior of peptides in normal tissues where the peptides are not subject to cleavage. Although the control formulation still underwent cell membrane bonding as shown by the confocal microscopy and flow cytometry (**Fig. 2.8 A and B**), because of the overall positive changed surface. But most of the peptide nanofibers were stuck to the cell membrane interface which doesn't help to enhance the drug permeability.

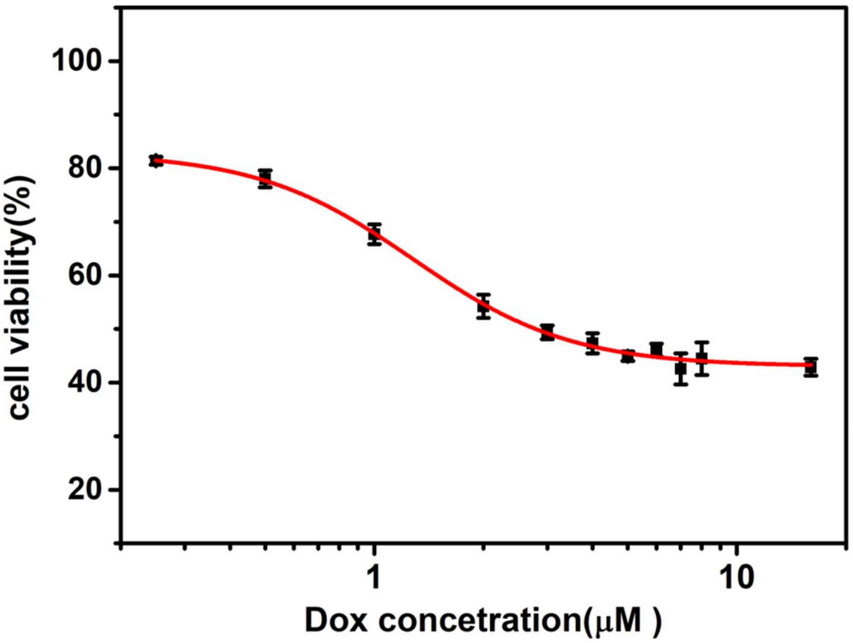

Figure 2.11 IC50 of Doxorubicin in Hela cell

An intriguing phenomenon was observed, that is the IC(50) value of DOX in the presence of K(C6)E appeared to be higher than that of DOX alone. The result suggested that the cell uptake of DOX was inhibited upon the addition of the intact supramolecular nanofibers which are expected to exist in healthy tissues and cells. The mechanistic origin of this unusual effect is largely unknown, but certainly deserves additional research efforts to understand. Further validation of the results using other small molecule drugs will help justify the current design system in terms of its capability to protect healthy tissues and cells from passive uptake of cancer therapeutics. Meanwhile, the cell viability of K(SS)E and K10 alone was estimated at 70% and 81% while K(C6)E showed 97% viability after 24 h of incubation with HeLa cells (**Fig. 2.12**). Moderate cytotoxicity is generally recognized when designing cationic peptides/lipids/polymers.[33-34] However, in this work, the relative higher cytotoxicity of the reduction-responsive cell penetrating nanofiber may not be a significant concern because the peptide is only expected to function in tumor specific sites as the experiment is also performed in a cancer cell line. In healthy tissues, it is mostly dormant and is not expected to be cytotoxic as shown in the case of the nonresponsive formulation based on K(C6)E.

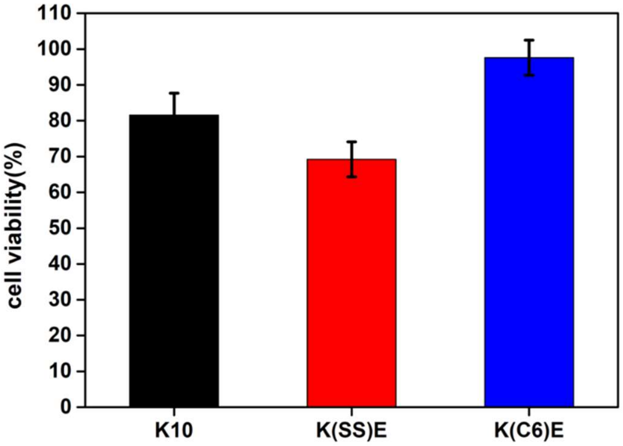

Figure 2.12 Cell viability of K(SS)E, K(C6)E and K10 (16 μM) after 24 hs incubation with Hela cells.

2.4 Conclusions

In conclusion, we designed a new class of supramolecular materials based on the self-assembly of β-sheet forming MDPs with a tunable nanostructure and cell penetrating activity in response to reduction triggers. Owing to the supramolecular packing order of the MDPs, the anions and cations were juxtaposed at the periphery of the nanofiber where the lysine residues are partially neutralized by the glutamic acid residues within the assembly process. Trigger responsive cleavage removal of the polyanions allows for deshielding of the positive charges on the nanofiber. The increased electron static repulsion led to a reduction of the fiber length. The newly produced short nanofibers demonstrated superior cell penetrating activity and significantly improved drug efficacy upon co-incubation with drug molecules in the reduction HeLa cell culture. Although the current peptides are designed to be reduction-sensitive, the cleavable linker is amenable to changing any other types of responsive triggers in diseased tissues and cells such as pH, enzyme and hypoxia. The modular nature of the MDPs and the solid phase synthesis method allows easy incorporation of non-natural amino acids or synthetic linkers or polymers into the peptide sequence to overcome the structural limitation associated with natural amino acids. This study is expected to provide important guidelines and templates for the design of peptide-based trigger-responsive self-assembly to satisfy various needs in biomedical applications. Further study on multi-responsive MDPs for targeted therapeutic delivery is deserved to explore.

2.5 Experimental Section

General Methods

MBHA rink amide resin, Fmoc-protected amino acids, O-(Benzotriazol-1-yl)-N,N,N',N'-tetramethyluronium hexafluorophosphate (HBTU) were purchased from Novabiochem. Piperidine and diisopropylethylamine (DIPEA) were purchased from Sigma-Aldrich. All other reagents and solvents for peptide synthesis and purification were purchased from Fisher Scientific and used as received. Dulbecco's modified Eagle medium (DMEM) culture medium, Hoechst 33342 and LysoTracker Red DND-99 were purchased from Life Technologies. Fetal Bovine Serum (FBS) was ordered from VWR. CCK8 assay kit was obtained from Dojindo Molecular Technologies (Rockville, MD). 1H NMR (JEOL ECX 500MHz) was used to characterize the synthesized compounds. Fluorescence measurements were performed on Varian Cary Eclipse fluorescence spectrophotometer. Circular dichroism

(CD) spectra were acquired on a Jasco-J715 spectrometer using a quartz cell with 1 mm path length. Transmission electron microscopy (TEM) was conducted on a JEOL 2010 high-resolution transmission electron microscope. Reversed-phase HPLC was carried out on a HITACHI L-7100 pump using a Higgins semi-prep column (proto 300 C4 10 μm, 250*10 mm). UV absorbance was measured on a micro-plate reader (Vitor2 1420 Multilabel Counter, PerkinElmer) for toxicity quantification.

Synthesis of the reductive responsive linker Fmoc-Cystamine succinate (Fmoc-CS)

Cystamine dihydrochloride (2.25g, 10 mmol) and NaHCO3 (2.52g, 30 mmol) erewere dissolved in deionized water. Then 35 mL of Dioxane was added by drop with stirring. Succinic anhydride (1.00g 10 mmol) was added to the above solution. The resulting reaction mixture was stirred at room temperature for overnight. Then NaHCO3(0.84g 10 mmol) was added to the mixture. Afterwards 50 mL of acetone solution containing Fmoc-OSu (3.373g 10 mmol) was added. Then the reaction was last for 10 hs. The mixture was filtered remove the insoluble materials. The solution was concentrated by the rotary evaporator. The pH of the solution was adjusted to 1~3 by HCl. The final solution was cold down to 4℃ for 2 hs, and white powder was precipitated. The precipitate was collected by filtration and dried in vacuum. 1H-NMR (500 MHz, DMSOD6) δ 7.86 (d, J = 8.0 Hz, 2H), 7.65 (d, J = 7.4 Hz, 2H), 7.38 (t, J = 7.4 Hz, 2H), 7.30 (t, J = 7.4 Hz, 2H), 4.28 (d, J = 6.9 Hz, 2H), 4.18 (t, J = 6.9 Hz, 1H), 2.72 (q, J = 6.5 Hz, 4H), 2.38 (t, J = 6.9 Hz, 2H), 2.28 (t, J = 6.9 Hz, 2H)

Peptides Synthesis and Purification

The synthesis of MDPs followed the standard Fmoc-solid phase peptide synthesis method. Briefly, Fmoc group was deprotected in the presence 20% (V/V) piperidine/DMF for 5 minutes, and was repeated once. HBTU was used as the coupling reagent and the coupling reaction was carried out for 45 mins in the presence of diisopropyl ethyl amine (DIPEA) and five equivalents of Fmoc protected amino acids. After the completion of the synthesis, the N-terminus of the MDPs was acetylated using DIPEA and acetic anhydride in DMF for 1 h. The Kaiser test was used to verify the completion of the reaction. The acetylated peptide was cleaved in a mixture of TFA / triisopropanolsilane (TIS) / H2O (95/2.5/2.5 by volume). After 3 hs, the cleavage solution was collected and the resin was washed twice with neat TFA. TFA was evaporated under air flow and the residual solution was precipitated with cold diethyl ether. The resulting precipitate was collected by centrifugation at 6500 rpm for 5 min and washed three times with cold diethyl ether. Upon completion of the final amino acid coupling, 4 equivalents of 5(6)-carboxyfluorescein were added to the resin in the presence of 4 equivalents of HBTU and 8 equivalents of DIPEA in DMF. After 24 hs, the reaction mixture was filtered and the resin was tested by Kaiser test. If needed, coupling reaction was repeated until a negative Kaiser test result is achieved. The resin was cleaved using the same procedure as for the non-labeled peptides. The crude peptide was then dried under vacuum overnight for further HPLC purification. Peptides were purified using a preparative reverse phase C18 column with a linear gradient of binary water/acetonitrile solvent containing 0.05% TFA. Elution was monitored at 280 nm. The HPLC fraction was collected, combined and dried in the lyophilizer for 3 days. The molecular weight of each peptide was confirmed by by MALDI-TOF mass spectrometry using a-cyano-4-hydroxycinnamic acid as the matrix.

K(SS)E: expected [M+H]+: 4105, observed [M+H]+: 4105; FITC-K(SS)E: expected [M+H]+: 4421, observed [M+H]+: 4421; K(C6)E: expected [M+H]+: 3983, observed [M+H]+: 3984; FITC-K(C6)E: expected [M+H]+: 4299, observed [M+H]+: 4299. For all the experiments, peptide stock solution was prepared by dissolving lyophilized peptide powder in Tris buffer (20 mM, pH=7.4) to reach a final concentration at 800 μM and left at 4°C for a day.

Circular Dichroism (CD) Spectroscopy

MDPs were diluted to 100 μM in Tris buffer (pH 7.4, 20 mM) for CD measurements. The data were collected from 250 nm to 190 nm at room temperature with a scan rate of 100 nm/min, a bandwidth of 1 nm and a response time of 2 sec. The final spectra were an average of five scans. The mDeg of rotation was converted to the molar residual ellipticity via the formula $\theta=(mDeg*1000)/(c*n*l)$, where c is the concentration of the peptide solution in mM, n is the number of amino acids in the peptide sequence and l is the path length of the cell used in mm.

Transmission Electron Microscopy (TEM)

MDPs were diluted to 100 μM in Tris buffer (pH 7.4, 20 mM). 10 μl of the peptide solution was dropped onto a holey carbon grid (TED PELLA 01824). After 1 min, the excess solution was carefully removed with filter paper. 10 μl of 2 wt% uranyl acetate solution was dropped onto the grid for negative staining. The excess staining solution was removed with filter paper and the TEM sample was dried for overnight before imaging.

Zeta Potential Measurement

Zeta Potential was performed on a Malvern Zetasizer. MDPs were diluted to 40 µM in Tris buffer (pH 7.4, 20 mM). The zeta potential was averaged on three measurements with a total number of 50 scans in each.

Critical Aggregation Concentration (CAC) Measurement

CACs were determined using a previous protocol based on the fluorescence intensity change of tryptophan. Peptide stock solution (160 µM) was added into 200 µL Tris buffer (20 mM, pH=7.4) with an increment of 2 µL each time. Fluorescence emission was acquired from 295 nm to 440 nm with the excitation wavelength at 280 nm. Fluorescence intensity at 350 nm was plotted as a function of the peptide concentration. The CAC was determined at the crossing point in which the linearity deviates from the initial trend.

Cytotoxicity Measurement

HeLa cells were seeded onto a 96-well plate at a density of 104 cells/well and incubated for 24 hs at 37 °C in an incubator with 5% CO2. The culture medium was replaced and 10 µL of peptide solution (160 µM) was added to reach a final concentration of 16 µM. DOX was added to each well plate to reach final concentrations ranging from 0.05 µM to 4 µM. After 24 hs of incubation, the CCK-8 assay was used to quantify cell viability by monitoring the UV absorbance at 450 nm. All the experiments were performed in four replicates.

Cell Uptake

HeLa cells were seeded onto a confocal dish at a density of 1 x 105 cells/well. FITC-labeled peptides were diluted in Tris buffer to a final concentration of 160 μM. 20 μL of the peptide solution was added to the cell culture medium to reach a concentration at 16 μM. After 2 hs and 24 hs of incubation, cells were washed with PBS buffer for three times. Images were captured using a laser scanning confocal microscope (Leica DMi8, Germany) and processed with ImageJ software.

Flow Cytometry

HeLa cells were seeded onto a 24-well plate at a density of 105 cells/well and incubated for 24 hs 37 °C. Culture medium was replaced with 200 μL fresh DMEM medium and 20 μL of FITC labeled peptide solutions (160 μM) were added. After incubation with FITC-labeled MDPs for 2 hs and 24 hs, cells were washed with PBS buffer for three times. Cells were digested with trypsin and washed twice with PBS buffer. 2% paraformaldehyde was used for cell fixation. Cell uptake of the FITC-labeled peptide was quantified using a BD FACS Calibur flow cytometer. A minimum of 10,000 events per sample was analyzed and data were processed using FlowJo software.

Statistical Analysis

All data were expressed as means ± standard deviation (SD). The statistical analysis was performed using Student's T-test and oneway analysis of variance (ANOVA) at confidence levels of 95%.

2.5 References

1. Torchilin, V. P., Multifunctional nanocarriers. *Adv Drug Deliv Rev* **2012,** *64*, 302-315.
2. Petros, R. A.; DeSimone, J. M., Strategies in the design of nanoparticles for therapeutic applications. *Nat. Rev. Drug Discov.* **2010,** *9* (8), 615.
3. Peer, D.; Karp, J. M.; Hong, S.; Farokhzad, O. C.; Margalit, R.; Langer, R., Nanocarriers as an emerging platform for cancer therapy. *Nat. Nanotechnol.* **2007,** *2* (12), 751.
4. Farokhzad, O. C.; Langer, R., Nanomedicine: developing smarter therapeutic and diagnostic modalities. *Adv Drug Deliv Rev* **2006,** *58* (14), 1456-1459.
5. Tseng, S.-J.; Liao, Z.-X.; Kao, S.-H.; Zeng, Y.-F.; Huang, K.-Y.; Li, H.-J.; Yang, C.-L.; Deng, Y.-F.; Huang, C.-F.; Yang, S.-C., Highly specific in vivo gene delivery for p53-mediated apoptosis and genetic photodynamic therapies of tumour. *Nat. Commun.* **2015,** *6*, 6456.
6. Poon, Z.; Chang, D.; Zhao, X.; Hammond, P. T., Layer-by-layer nanoparticles with a pH-sheddable layer for in vivo targeting of tumor hypoxia. *ACS Nano* **2011,** *5* (6), 4284-4292.
7. Zhu, L.; Wang, T.; Perche, F.; Taigind, A.; Torchilin, V. P., Enhanced anticancer activity of nanopreparation containing an MMP2-sensitive PEG-drug conjugate and cell-penetrating moiety. *Proc. Natl. Acad. Sci.* **2013,** *110* (42), 17047-17052.
8. Huang, S.; Shao, K.; Liu, Y.; Kuang, Y.; Li, J.; An, S.; Guo, Y.; Ma, H.; Jiang, C., Tumor-targeting and microenvironment-responsive smart nanoparticles for combination therapy of antiangiogenesis and apoptosis. *ACS Nano* **2013,** *7* (3), 2860-2871.
9. Luo, Z.; Ding, X.; Hu, Y.; Wu, S.; Xiang, Y.; Zeng, Y.; Zhang, B.; Yan, H.; Zhang, H.; Zhu, L., Engineering a hollow nanocontainer platform with multifunctional molecular machines for tumor-targeted therapy in vitro and in vivo. *ACS Nano* **2013,** *7* (11), 10271-10284.
10. Dunn, S. S.; Tian, S.; Blake, S.; Wang, J.; Galloway, A. L.; Murphy, A.; Pohlhaus, P. D.; Rolland, J. P.; Napier, M. E.; DeSimone, J. M., Reductively responsive siRNA-conjugated hydrogel nanoparticles for gene silencing. *J. Am. Chem. Soc.* **2012,** *134* (17), 7423-7430.
11. Thambi, T.; Deepagan, V.; Yoon, H. Y.; Han, H. S.; Kim, S.-H.; Son, S.; Jo, D.-G.; Ahn, C.-H.; Suh, Y. D.; Kim, K., Hypoxia-responsive polymeric nanoparticles for tumor-targeted drug delivery. *Biomaterials* **2014,** *35* (5), 1735-1743.
12. Perche, F.; Biswas, S.; Wang, T.; Zhu, L.; Torchilin, V., Hypoxia‐Targeted siRNA Delivery. *Angew. Chem.* **2014,** *126* (13), 3430-3434.
13. Shi, Y.; Hu, Y.; Ochbaum, G.; Lin, R.; Bitton, R.; Cui, H.; Azevedo, H. S., Enzymatic activation of cell-penetrating peptides in self-assembled nanostructures triggers fibre-to-micelle morphological transition. *Chem. Commun.* **2017,** *53* (52), 7037-7040.
14. Jiang, T.; Olson, E. S.; Nguyen, Q. T.; Roy, M.; Jennings, P. A.; Tsien, R. Y., Tumor imaging by means of proteolytic activation of cell-penetrating peptides. *Proc. Natl. Acad. Sci. U. S. A.* **2004,** *101* (51), 17867-17872.

15. Jiang, T.; Zhang, Z.; Zhang, Y.; Lv, H.; Zhou, J.; Li, C.; Hou, L.; Zhang, Q., Dual-functional liposomes based on pH-responsive cell-penetrating peptide and hyaluronic acid for tumor-targeted anticancer drug delivery. *Biomaterials* **2012,** *33* (36), 9246-9258.
16. Rajendran, L.; Knölker, H.-J.; Simons, K., Subcellular targeting strategies for drug design and delivery. *Nat. Rev. Drug Discov.* **2010,** *9* (1), 29.
17. Wei, H.; Zhuo, R.-X.; Zhang, X.-Z., Design and development of polymeric micelles with cleavable links for intracellular drug delivery. *Prog. Polym. Sci.* **2013,** *38* (3-4), 503-535.
18. Fosgerau, K.; Hoffmann, T., Peptide therapeutics: current status and future directions. *Drug Discov. Today* **2015,** *20* (1), 122-128.
19. Deshayes, S.; Morris, M.; Divita, G.; Heitz, F., Cell-penetrating peptides: tools for intracellular delivery of therapeutics. *Cellular and Molecular Life Sciences CMLS* **2005,** *62* (16), 1839-1849.
20. Gupta, B.; Levchenko, T. S.; Torchilin, V. P., Intracellular delivery of large molecules and small particles by cell-penetrating proteins and peptides. *Adv Drug Deliv Rev* **2005,** *57* (4), 637-651.
21. Xu, D.; Samways, D. S.; Dong, H., Fabrication of self-assembling nanofibers with optimal cell uptake and therapeutic delivery efficacy. *Bioactive Materials* **2017**.
22. Xu, D.; Dustin, D.; Jiang, L.; Samways, D. S.; Dong, H., Designed filamentous cell penetrating peptides: probing supramolecular structure-dependent membrane activity and transfection efficiency. *Chem. Commun.* **2015,** *51* (59), 11757-11760.
23. Wen, Y.; Waltman, A.; Han, H.; Collier, J. H., Switching the immunogenicity of peptide assemblies using surface properties. *ACS Nano* **2016,** *10* (10), 9274-9286.
24. Fleige, E.; Quadir, M. A.; Haag, R., Stimuli-responsive polymeric nanocarriers for the controlled transport of active compounds: concepts and applications. *Adv Drug Deliv Rev* **2012,** *64* (9), 866-884.
25. Chen, W.; Zhong, P.; Meng, F.; Cheng, R.; Deng, C.; Feijen, J.; Zhong, Z., Redox and pH-responsive degradable micelles for dually activated intracellular anticancer drug release. *J. Control. Release* **2013,** *169* (3), 171-179.
26. Steinhilber, D.; Sisson, A. L.; Mangoldt, D.; Welker, P.; Licha, K.; Haag, R., Synthesis, reductive cleavage, and cellular interaction studies of biodegradable, polyglycerol nanogels. *Adv. Funct. Mater.* **2010,** *20* (23), 4133-4138.
27. Ren, C.; Song, Z.; Zheng, W.; Chen, X.; Wang, L.; Kong, D.; Yang, Z., Disulfide bond as a cleavable linker for molecular self-assembly and hydrogelation. *Chem. Commun.* **2011,** *47* (5), 1619-1621.
28. Xu, D.; Ran, Q.; Xiang, Y.; Jiang, L.; Smith, B. M.; Bou-Abdallah, F.; Lund, R.; Li, Z.; Dong, H., Toward hemocompatible self-assembling antimicrobial nanofibers: understanding the synergistic effect of supramolecular structure and PEGylation on hemocompatibility. *RSC advances* **2016,** *6* (19), 15911-15919.
29. Chen, Y.; Barkley, M. D., Toward understanding tryptophan fluorescence in proteins. *Biochemistry* **1998,** *37* (28), 9976-9982.
30. Gamcsik, M. P.; Kasibhatla, M. S.; Teeter, S. D.; Colvin, O. M., Glutathione levels in human tumors. *Biomarkers* **2012,** *17* (8), 671-691.

31. Yang, M.; Xu, D.; Jiang, L.; Zhang, L.; Dustin, D.; Lund, R.; Liu, L.; Dong, H., Filamentous supramolecular peptide–drug conjugates as highly efficient drug delivery vehicles. *Chem. Commun.* **2014,** *50* (37), 4827-4830.
32. Xu, D.; Jiang, L.; Singh, A.; Dustin, D.; Yang, M.; Liu, L.; Lund, R.; Sellati, T. J.; Dong, H., Designed supramolecular filamentous peptides: balance of nanostructure, cytotoxicity and antimicrobial activity. *Chem. Commun.* **2015,** *51* (7), 1289-1292.
33. Lv, H.; Zhang, S.; Wang, B.; Cui, S.; Yan, J., Toxicity of cationic lipids and cationic polymers in gene delivery. *J. Control. Release* **2006,** *114* (1), 100-109.
34. Breunig, M.; Lungwitz, U.; Liebl, R.; Goepferich, A., Breaking up the correlation between efficacy and toxicity for nonviral gene delivery. *Proc. Natl. Acad. Sci.* **2007,** *104* (36), 14454-14459.

Chapter 3. Peptide Self-Assembly with Cell Penetrating Activity*

3.1 Introduction

The discovery of cell penetrating peptides (CPPs) has great impacts on both fundamental and translational biomedical research due to their seemingly at will ability to transverse the cell membrane.[1-5] The structure-dependent membrane activity of CPPs inspired the design of a range of cell penetrating polymers and liposomes with multivalent presentation of cationic groups, which play important roles in mediating their membrane activity.[6-7] Compared to traditional CPPs, these cell penetrating macromolecules show improved stability and tunable pharmacokinetics although their cytotoxicity has been a concern.[8-9]

As an alternative for the fabrication of macromolecular structures, peptide self-assembly offers an effective method to generate peptide-based nanomaterials with much higher stability than monomeric peptides, tunable nanostructures, biological activity and good biocompatibility.[10-20] In particular, the high aspect ratio peptide nanofibers, which are formed through self-assembly of β-sheet peptides show good stability and high resistance toward proteolysis.[21-23] Recently there have been increasing interests in the design of peptide nanofibers for vaccine and gene delivery, which often require highly efficient delivery of antigenic and genetic agents in the cytoplasm.[12, 24] From this

---

* This chapter is based on Su Yang et al. Modular design and self-assembly of multidomain peptides towards cytocompatible supramolecular cell penetrating nanofibers. *RSC Adv.*, **2020**, *10(49)*, 29469-29474. Some sections were rearranged for continuity.

perspective, peptide nanofibers with intrinsic cell penetrating activity would be greatly beneficial to the development of peptide-based immuno-and gene therapy.

Inspired by recent advances in peptide self-assembly and cell penetrating macromolecules, we have developed a new class of peptide assemblies with intrinsic cell penetrating activity, termed as supramolecular cell penetrating nanofibers (SCPNs).[25-28] SCPNs are generated through the self-assembly of *de novo* designed cationic multidomain peptides (MDPs) with a general sequence of $K_x(QW)_6$ (K: lysine, Q: glutamine; W: tryptophan). The central $(QW)_6$ domain drives the self-assembly to form "sandwich"-like β-sheet nanofibers while the terminal domain consisting of a variable number of lysine residues drives disassembly due to electrostatic repulsion among the lysine residues. The end products reflect an energetic balance between the attractive forces provided by the $(QW)_6$ domain and the repulsive forces among the lysine residues. Upon self-assembly, MDP nanofibers display a high positive charge density due to the accumulation of the lysine residues at the fiber-solvent interface, and therefore being potentially membrane-active. Although we have fabricated a library of supramolecular peptide assembly using the $K_x(QW)_6$ series as the molecular building block and identified a potent cell penetrating nanofiber based on $K_{10}(QW)_6$,[26, 28] the sample preparation was tedious. Desalting was often required to induce self-assembly for peptides having a relatively larger number of lysine residues. Although the mechanism for desalting-induced self-assembly has not been fully understood, we presume that parts of the lysine residues were deprotonated upon trifluoroacetate exchange by carbonate during the desalting process, thereby the electrostatic repulsion was reduced, and the equilibrium was shifted toward self-assembly. Although desalting is effective to generate

SCPNs, the procedure is relatively tedious. In the current work, we aim to apply the self-assembly strategy based on a new set of modularly designed MDPs for facile generation of cationic supramolecular peptide assemblies and screening their cell penetrating activity.

3.2 Results and Discussion

3.2.1 Peptide Design

To demonstrate the self-assembly strategy for the construction of cell penetrating peptide assemblies, we synthesized a new series of MDPs, $K_x(QW)_6E_y$. In this design, we simply add a few glutamic acids to the C terminal of the peptide which is appended at the opposing end of lysine residues to allow certain attractive ionic interactions. With the addition of glutamic acid residues, it provided an enhanced driving force to shift the equilibrium toward self-assembly. Based on our previous work, the supramolecular nanofiber is a prerequisite, but not a sufficient factor for potent cell penetrating activity. The flexibility which highly relies on the length of the cationic domain of the supramolecular charge domain is also critical for improving the membrane activity of supramolecular peptides. In our study of the $K_x(QW)_6$ series, we found that a minimum of seven lysines was required to keep a flexible cationic domain for effective cell membrane interactions and enhanced therapeutic delivery efficacy.[26, 28] Therefore, in this work, we intend to keep the excess of lysine residues at or above 7 for the new sequences in order to ensure effective membrane interactions. Specifically, two or three glutamic acids were added to the C-terminus of $K_{10}(QW)_6$ to stabilize the self-assembly nanostructure while keeping sufficient positive charged domain descent and flexibility.

Table 0.1 Sequences of cationic MDPs used in the study to probe the supramolecular structural and structure-dependent membrane activity

Abbreviation	**Sequences**
K10	KKKKKKKKKKQWQWQWQWQWQW
K10-E2	KKKKKKKKKKQWQWQWQWQWQWEE
K10-E3	KKKKKKKKKKQWQWQWQWQWQWEEE
K12-E3	KKKKKKKKKKKKQWQWQWQWQWQWEEE

By designing a small library of MDPs with varying numbers of lysine and glutamic acid residues, we expect to generate self-assembled peptides with different supramolecular nanostructures and intermolecular packing within the assemblies. By evaluating the membrane activity, we explore and optimize supramolecular-structure dependent cell penetrating activity. **Table 3.1** shows the full peptide sequences and their abbreviated names which reflect the numbers of lysine and glutamic acid in the sequence, while the repeating unit of QW is kept as 6. For example, K10-E2 refers to the sequence of $K_{10}(QW)_6E_2$. All peptides were synthesized through standard Fmoc-solid phase peptide synthesis protocol and used without further treatment after reverse phase HPLC purification. All the peptide was confirmed with MALDI-TOF. (**Fig. 3.1**)

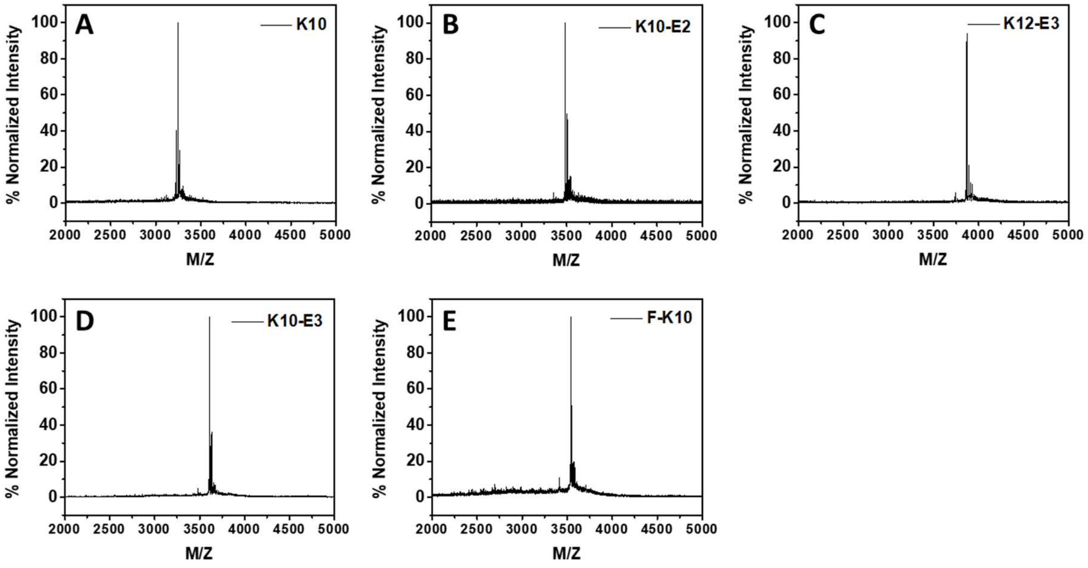

Figure 3.1 MALDI spectra of (A) K10 (B) K10-E2 (C) K12-E3 (D) K10-E3 and (E) F-K10.

3.2.2 Structural Characterization of Self-Assembled MDPs

The MDPs were evaluated for their ability to self-assemble in Tris buffer (pH 7.4, 20 mM). Using a previously established tryptophan fluorescence quenching method,[29-30] the critical assembly concentrations (CACs) of all glutamic acid containing MDPs were determined at 11-12 μM which suggested that all of them can form some level of self-assemble (**Fig. 3.2**).

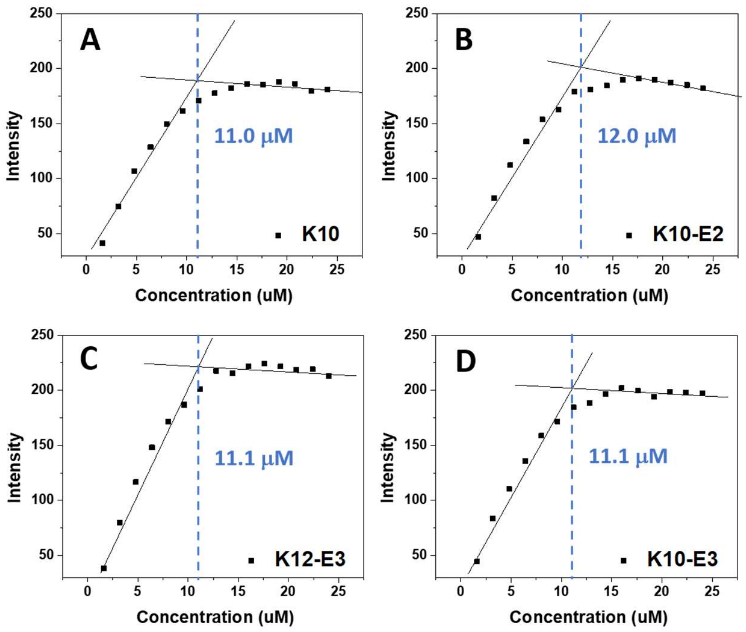

Figure 3.2 CAC determination of (A) K10, (B) K10-E2 (B), (C) K12-E3 and (D) K10-E3 by plotting the tryptophan fluorescence intensity as a function of peptide concentrations.

To quantitatively determine the oligomerization states of each assembly nanostructure and the relative abundance of oligomers versus monomers upon equilibrium, we performed sedimentation velocity (SV) experiments using the analytical ultracentrifugation (AUC) technique. Samples were prepared in Tris buffer at 20 µM (above their CACs) and incubated for 24 hs at 4 °C to achieve equilibrium toward self-assembly. By monitoring the sedimentation profile of each sample in real-time, we can obtain a distribution of sedimentation coefficients which can be used to calculate the observed molecular weight of each species present in each peptide sample. **Fig. 3.3** showed the raw sedimentation scans taken every ~ 30 mins at 50,000 rpm and the residual plot supplied by SEDFIT software which showed the goodness of fit.

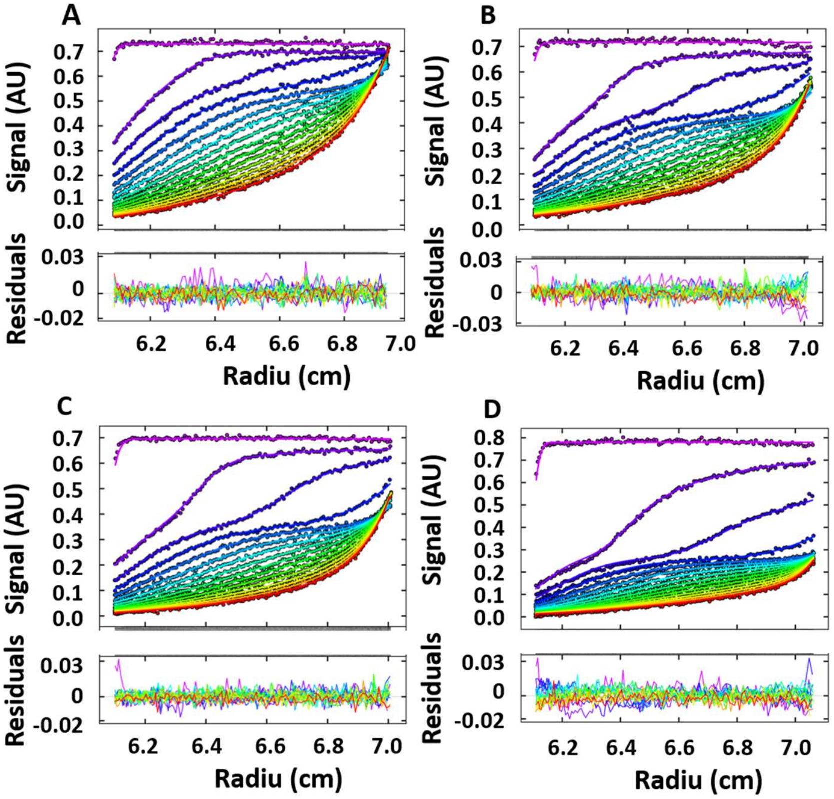

Figure 3.3 Raw sedimentation profiles by monitoring the absorbance at 280 nm versus cell radius and residual plots supplied by SEDFIT software showing the fitting goodness. (A) K10, (B) K10-E2, (C) K12-E3 and (D) K10-E3.

As shown by the distribution of sedimentation coefficients (**Fig. 3.4**), we confirmed that the majority (78%) of K10 existed as monomers and 22% formed oligomers consisting of 12 subunits. By adding glutamic acids on K10, the percentage of the oligomeric species was significantly increased. For example, both K10 and K10-E2 formed oligomers of a similar size, but the percentage of oligomers in K10-E2 (37%) was much higher than that of K10 (22%) (**Fig. 3.4B**). Further increasing the numbers of glutamic acid further drives the equilibrium toward self-assembly which led to the formation of larger assemblies composed of more than 30 subunits (**Fig. 3.4D**). The larger scale supramolecular assemblies are more heterogeneous than small oligomers formed by K10 and K10-E2. This observation is consistent with what is commonly found in amyloid-like fibrous peptide assembly.[31] It is also worth noting that these assemblies formed by K10-E3 were in equilibrium with dimers rather than monomers as found with K10 and K10-E2. Compared to K10-E3, K12-E3 formed small oligomers in equilibrium with monomers, which is consistent with the sequence-structure design rule for MDP self-assembly (**Fig. 3.4C**). The twelve lysine residues need additional glutamic acids are needed to balance the higher repulsive interactions to induce the large self-assembly. These results suggested the supramolecular peptide nanostructures could be tuned by varying the ratio of lysine and glutamic acid residues. The potential molecular packing and nanostructure size were correlated to the peptide design, and the resulted peptide nanostructure has high potential for further morphology and biological activity study.

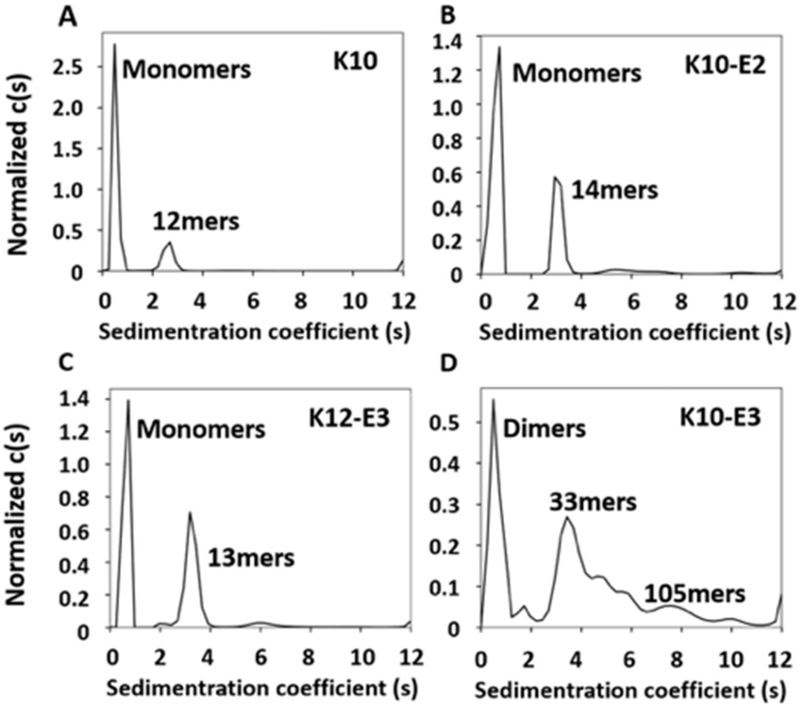

Figure 3.4 AUC-sedimentation velocity data of (A) K10, (B) K10-E2, (C) K12-E3 and (D) K10-E3 as a semi-quantitative measure of the assembly states. Continuous sedimentation coefficient distribution,

c(s) curve, obtained with a regularization procedure. Peptide concentration: 20 μM in Tris buffer (20 mM, pH = 7.4).

The supramolecular structure of peptide assembly was examined by negatively stained transmission electron microscopy (TEM). As shown in **Fig. 3.5A**, K10 was invisible under TEM likely due to the fact that K10 largely existed as a monomer. With additional glutamic acids to promote self-assembly, K10-E2 and K12-E3 formed spherical micellar nanostructures while K10-E3 formed nanofibers mixed with a small fraction of micelles (**Fig. 3.5B-D**). The result is consistent with the AUC data (**Fig. 3.4**), which contributed to the hypophysis of lysine and glutamic acid ratio tuned nanostructure change.

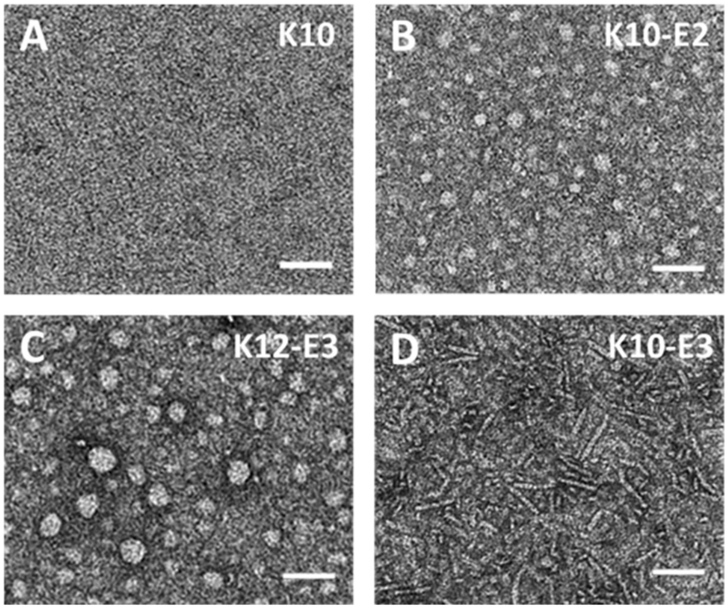

Figure 3.5 Negatively stained TEM images of (A) K10, (B) K10-E2, (C) K12-E3 and (D) K10-E3. Scale bar = 50 nm.

Based on the AUC and TEM results, we propose that MDPs may follow different self-assembly routes to form either spherical micelles or nanofibers **(Fig. 3.6)**. The self-assembly product is dictated by the energetic balance between the hydrophobic interactions among the (QW) repeating units, the electronic repulsive interactions among the lysine residues and the attractive ionic interactions between lysines and glutamic acids. By varying the ratio of lysine and glutamic acids, we expect to change the priority factor in balance and further affect the self-assembly pathway and product. For K10-E2 and K12-E3, AUC confirmed the presence of peptide monomers in equilibrium with oligomers (**Fig. 3.4B and 3.4C**). The monomers are likely to fold into a pseudo β-hairpin conformation which is driven by the intramolecular ionic interactions between the lysine and glutamic acids. Although these MDPs were not designed to form a β-hairpin, studies showed that appending oppositely charge amino acids at the peptide termini can drive the formation of β-hairpin conformation.[32-34] Indeed, the β-strand conformation of K10-E2 and K12-E3 was confirmed by circular dichroism (CD) spectroscopy (**Fig. 3.7**). While the QW repeat unit was still donated to the conformation by self-bonded. This could largely be due to the low lysine and glutamic acid ratio, the glutamic acid could be fully shielded by intramolecular interaction, and the intermolecular was bent. These β-hairpin conformation experienced further self-assemble into micelles due to the hydrophobic packing between the QW domain as observed by TEM. But due to the leading factor of electronic repulsion between polylysine domain, only oligomers were achieved.

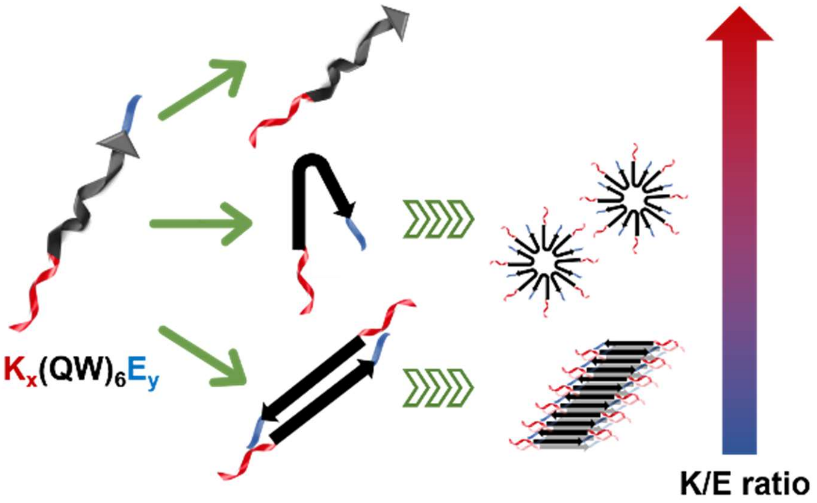

Figure 3.6 Color-coded schematic representation of $K_x(QW)_6E_y$ and their self-assembly routes to form spherical particles and nanofibers. Red: K_x as the cationic domain; black: $(QW)_6$ to drive the supramolecular packing of the β-sheet nanofibers; blue: E_y as the anionic domain.

For K10-E3, due to the increased portion of glutamic acids with respect to the lysine domain, instead of monomer, dimers were found to be in equilibrium with higher ordered assemblies (**Fig. 3.4D**). These dimers are possibly initiated by the intermolecular attractive ionic interactions, due to the low ratio of lysine and glutamic acid, followed by the hydrophobic packing. The dimers adopt a β-strand conformation as shown by the CD spectroscopy (**Fig. 3.7**), which can further self-assemble into nanofibers as driven by the intermolecular hydrogen bonding. It is important to note that slight variation of the relative numbers of lysine and glutamic acid in the peptide sequence could highly impact the self-assemble process, such as the initial formation of monomers versus dimers, and further aggregation into micelles versus nanofibers. This suggests a fine energetic balance existed between the attractive and repulsive interactions on these MDPs, which in turn can be used to manipulate the self-assembly pathways and products.

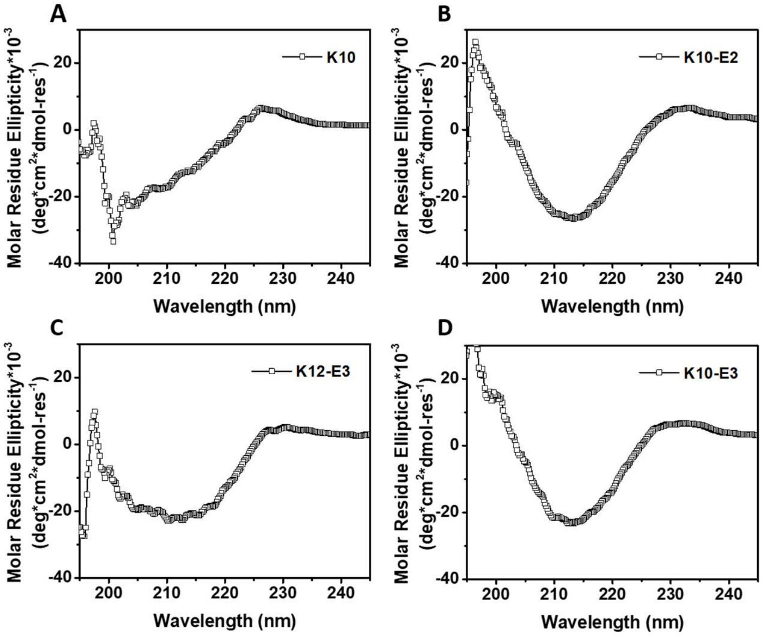

Figure 3.7 CD spectra of (A) K10, (B) K10-E2, (C) K12-E3 and (D) K10-E3 in Tris buffer (pH 7.4, 20 mM). Peptide concentration: 20 μM.

3.2.3 Evaluation of the Membrane Activity by Cell-Based Fluorescence Imaging

In vitro cell uptake experiment was performed to evaluate the cell penetrating activity of different MDPs. In the experimental design of cell uptake, rather than using 100% of FITC-labeled MDPs, we prepared co-assembled MDPs which consist of a small fraction of FITC labeled peptides to alleviate the potential effect of the bulky, hydrophobic fluorescent moiety on non-specific cell uptake. Meantime, with 100% FITC label, peptides also tend to be precipitated in cell culture which could be a digester for cell uptake. As demonstrated in our earlier work,[35] the co-assembled peptides can be prepared by physically mixing 5% of fluorescein (FITC) labeled MDPs with 95% of non-labeled MDPs in an organic solvent, such as acetonitrile followed by lyophilization and rehydrate of MDP powders in Tris buffer. Notably, for the preparation of the co-assembled samples, all of the MDPs were mixed and co-assembled with FITC-labeled

K10, rather than using FITC-labeled peptides of their own sequences. Given the consensus $(QW)_6$ domain, even with a different sequence, FITC-labeled K10 (5% in total) is expected to co-assemble with the other peptides. The usage of a common imaging probe will minimize the variation of fluorescence intensity. As a result, the fluorescence intensity observed for cells is largely attributed to the different MDPs cell penetrating activities. The co-assembled MDPs were added to HeLa cell culture to reach a final concentration of 20 μM and incubated for 2 hs and 24 hs for fluorescence imaging and flow cytometry quantification. As shown in **Fig. 3.8**, after 2 hs of incubation with HeLa cells, the micelle and fiber forming MDPs showed much higher fluorescence intensity than monomeric K10 while no significant difference was observed among the self-assembling MDPs. It is also noticeable that all the self-assembled MDPs were mostly localized on the cell membrane area upon incubation with cells for 2 hs.

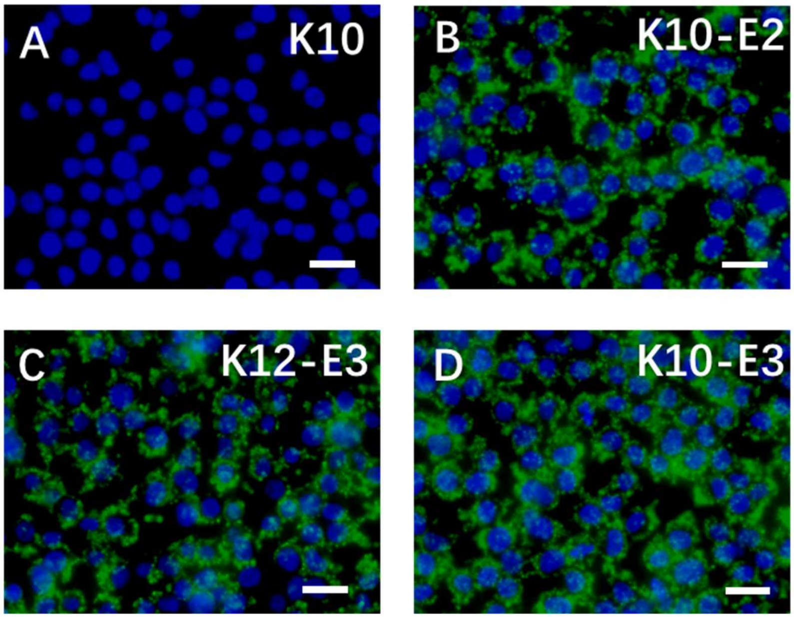

Figure 3.8 Fluorescence microscopic images of HeLa cells upon incubation with FITC-labeled (A) K10, (B) K10-E2, (C) K12-E3 and (D) K10-E3 for 2 hs. Scale bar = 25 μm.

Fig. 3.9A-D showed the fluorescence images of HeLa cells upon incubation with different MDPs for 24 hs. While K10 still had minimal fluorescence, the intracellular fluorescence was significantly enhanced for both micelle and fiber-forming MDPs, which suggested a time-dependent cell penetrating activity. K10-E3 exhibited the vitalized highest intracellular fluorescence intensity among all MDPs.

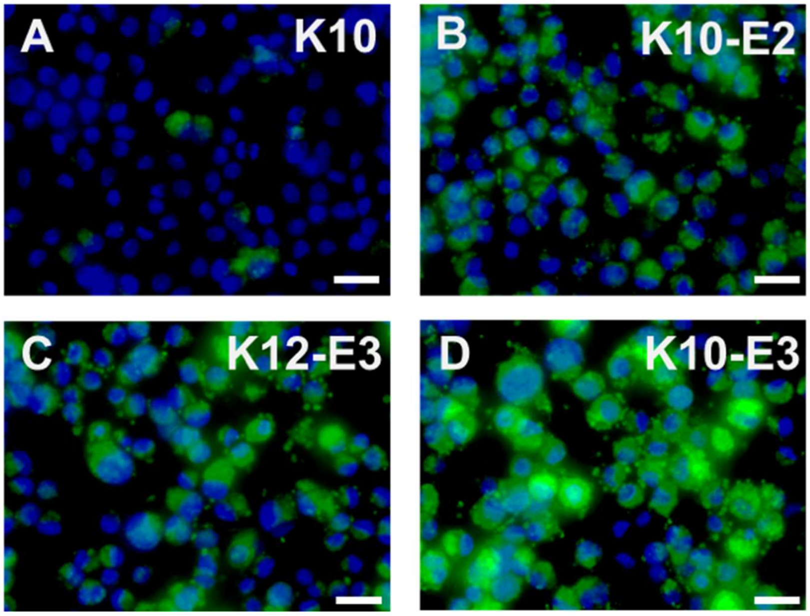

Figure 3.9 Fluorescence microscopic images of HeLa cells incubated with (A) K10, (B) K10-E2, (C) K12-E3 and (D) K10-E3 for 24 hs. Green: FITC labeled peptide, blue: nucleus staining. Scale bar = 25 μm.

Flow cytometry was used to qualitatively compare the cell uptake rate by measuring the mean fluorescence intensity of individual HeLa cells incubated with different MDPs for 24 hs (**Fig. 3.10**). Consistent with the fluorescence imaging results, HeLa cells treated with K10-E3 showed the highest fluorescence intensity, followed by K10-E2 and K12-E3 which have comparable fluorescence. All self-assembling MDPs demonstrated significantly higher cell uptake than the mostly monomeric peptide K10.

Notably, the four peptides have different charge densities and therefore different amphiphilicity.

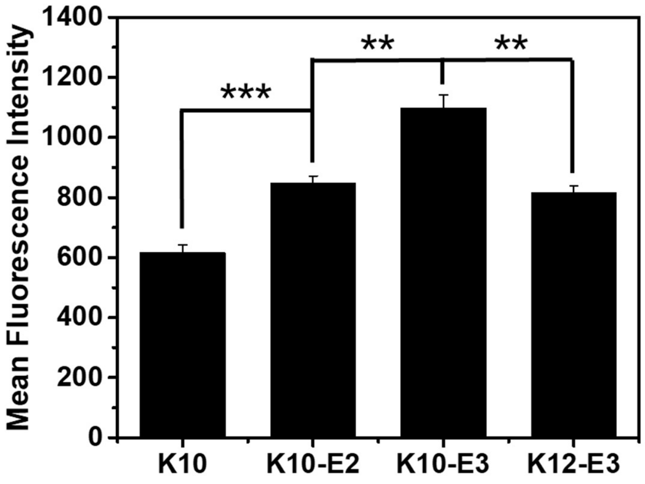

Figure 3.10 Fluorescence mean intensity of HeLa cells upon incubation with different MDPs as measured by flow cytometry. Peptide concentration: 20 μM. Statistically significant differences are indicated by $^{**}p<0.01$, $^{***}p<0.001$.

To investigate whether amphiphilicity plays an important role in increasing cell penetrating activity of K10-E3, we synthesized another multidomain peptide, $K_7(QW)_6$ (abbreviated as K7) which has the same net positive charges as K10-E3, while formed a different supramolecular nanostructure. Based on the physical characterization results (**Fig. 3.11A-C**), K7 was dementated to share similar self-assembly behavior as K10-E2 and K12-E3 by forming β-strand spherical micelles which were composed of 14 mers. Cell uptake results suggested dramatically less fluorescence (**Fig. 3.11D**) compared to that of K10-E3 (**Fig. 3.9D**), further supporting the important role of fiber-like nanostructure on cell penetrating activity.

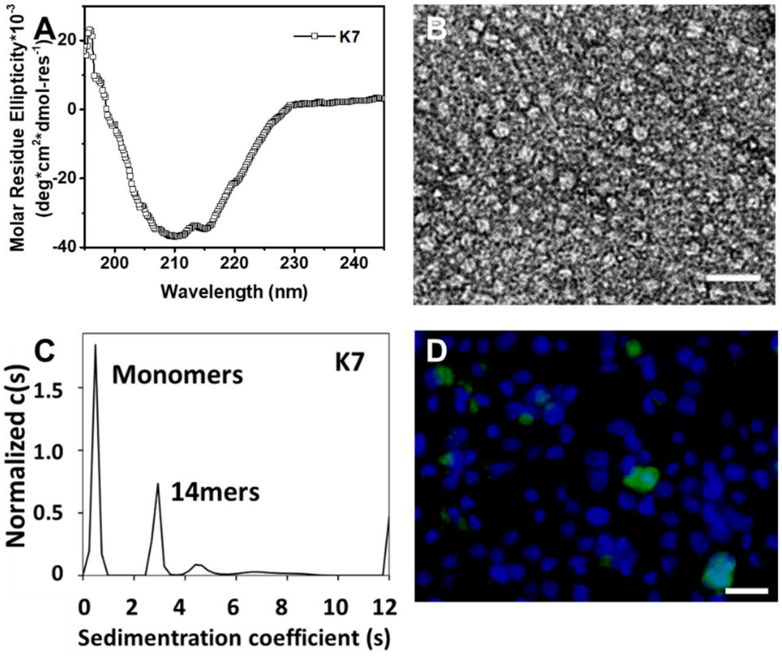

Figure 3.11 (A) CD spectrum of K7 in Tris buffer (pH 7.4, 20 mM). Peptide concentration: 20 μM. (B) Negatively stained TEM image of K7. Scale bar = 50 nm. (C) Sedimentation velocity data of K7 as a semi-quantitative measure of the assembly state. Peptide concentration: 20 μM in Tris buffer (20 mM, pH = 7.4). (D) Fluorescence microscopic images of HeLa cells incubated with co-assembled K7 (95%) and FITC-K10 (5%) for 24 hs. Green: FITC labeled peptide, blue: nucleus staining. Scale bar = 25 μm.

Based on the above results, we believe a large supramolecular assembly structure can enhance the cell penetrating activity of MDPs. However, we also found that the activity of different self-assembled morphology MDPs varied significantly. The result seemed highly impacted by the supramolecular structures and possibly the intermolecular packing of MDPs within the assembly. First of all, compared with a spherical micellar structure, a nanofiber can accommodate a larger number of cationic building blocks. This led to an increase in cationic charge multi-valency to achieve the multivalent interactions with the phosphate group on the negatively charged cell membrane. Secondly, in a nanofiber, the polycationic chain of MDPs is organized into brush-like nanostructures in which the cationic charges are more structurally confined at the fiber-solvent interface.

Such an organization could enhance the availability of the cationic clusters for corporative membrane binding. Thirdly, we expect the larger self-assemble structure, nanofibers, to be more kinetically stable than spherical micelles because of the highly cooperative non-covalent interactions involved in the formation and stabilization of supramolecular nanofibers. For example, nanofibers are stabilized by the directional hydrogen bonding between the amide bond along the long fiber axis while it does not exist or is relatively weak in spherical micelles because of the non-parallel structure. These interactions could help improve the kinetic stability of nanofibers in an enzyme-rich cellular culture environment and increase their biological availability. As part of future endeavors, experiments about quantitative kinetic stability measurement will be rationally designed and explored for these supramolecular assemblies.

3.2.4 Investigation of Cell Uptake Mechanism

Cytotoxicity of cell penetrating macromolecules has been a major concern for their application in biomedical and medical applications. Nature cell penetrating peptides which have dramatically high cell penetrating ability also been reported to cause cell damage and significant toxicity with low doses. Engineering polymer degradability has been used as an effective method to improve the cytocompatibility of cell penetrating polymers.[36-39] The cytotoxicity of these supramolecular peptides was evaluated in HeLa cell culture and the cell viability was quantified by the CCK8 assay after 24 hs of incubation of cells with each peptide. As shown in **Fig. 3.12**, all MDPs showed cell viability at > 70% up to 80 μM. The result suggested peptide self-assemble could also achieve good cytocompatibility with good cell penetrating ability. For all the natural monomeric cell penetrating peptides, the internalization mechanism is mostly directly embedded into cell membrane, the process induces membrane damage. So the discovery of low cytotoxicity for peptide self-assembly is of great interest, which is presumably related to the internalization mechanism employed by these supramolecular assemblies.

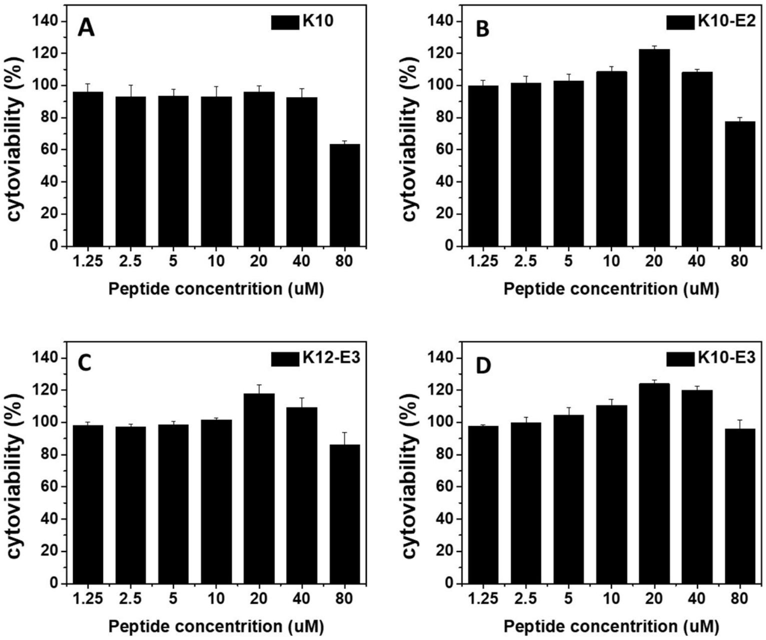

Figure 3.12 Viability of HeLa cells upon incubation with (A) K10, (B) K10-E2, (C) K12-E3 and (D) K10-E3. The cell viability assay was performed after 24 hs of incubation of HeLa cells with peptides with concentrations ranging from 1.25 μM to 80 μM.

Endocytosis is a much more preferred route for cell penetrating macromolecules to be internalized because it imposed less physical disruption on the cell membrane.[40-41] To investigate the internalization mechanism employed by these supramolecular peptides, we pre-incubated HeLa cells using three common endocytosis inhibitors for 2 hs before treated with peptide. The endocytosis inhibitors we picked are methyl-β-cyclodextrin (MβCD) for clathrin-mediated endocytosis, filipin III for caveolae-dependent endocytosis, and amiloride for macropinocytosis.[42-43] After removing the inhibitors, the most active cell penetrating assembly, K10-E3, was added to the cell culture and incubated for 24 hs before fluorescence imaging. As shown in **Fig. 3.13** (compared with **Fig. 3.9D**), while MβCD had no inhibitory effect on the cell uptake of K10-E3, both filipin III and amiloride treatment reduced fluorescence of HeLa cells upon K10-E3 treatment. The result suggested endocytosis as the predominant cell uptake mechanism for peptide assembly. In particular, dramatically fluorescence reduction was shown for amiloride treated cells, supporting that cell uptake is mostly mediated through macropinocytosis.

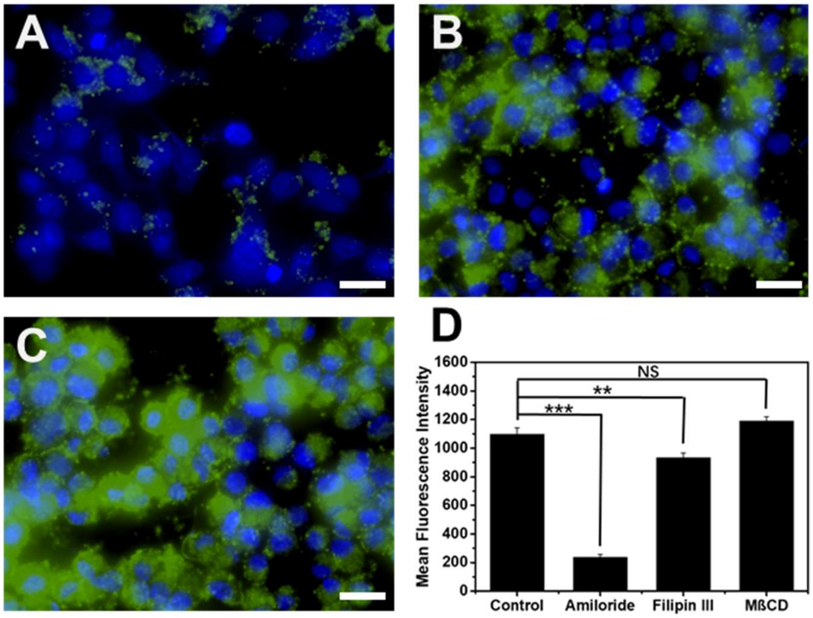

Figure 3.13 Fluorescence microscopic images of HeLa cells pre-incubated with (A) amiloride, (B) filipin III and (C) MβCD followed by the addition of FITC-labeled K10-E3 for fluorescence cell imaging. Green: FITC labeled K10-E3, blue: nucleus staining. Scale bar = 25 μm. Peptide concentration: 20 μM.

More interestingly, we observed diffuse intracellular distribution for the internalized K10-E3, rather than the punctate pattern commonly observed for materials that are trapped within the endosome or lysosome. Indeed, the majority of internalized K10-E3 did not co-localize with the Lysotracker (**Fig. 3.14**), indicating the ability of these supramolecular peptides to escape from the lysosome to reach the cytoplasm, which is an important attribute for the design of highly effective intracellular therapeutic delivery vehicles. It is also worth noting that the current work aims to establish a rationale for a fundamental peptide self-assembly mechanism by which cytocompatible SPCNs can be generated. For future practical biomedical and medical applications, by introducing various chemical functionalities, we can easily modify these MDPs to establish a specific response to a range of disease-specific microenvironments for triggered cell penetrating activity. Such efforts would be greatly beneficial for the development of smart SPCNs as disease-specific molecular therapy and imaging agents with high biocompatibility.

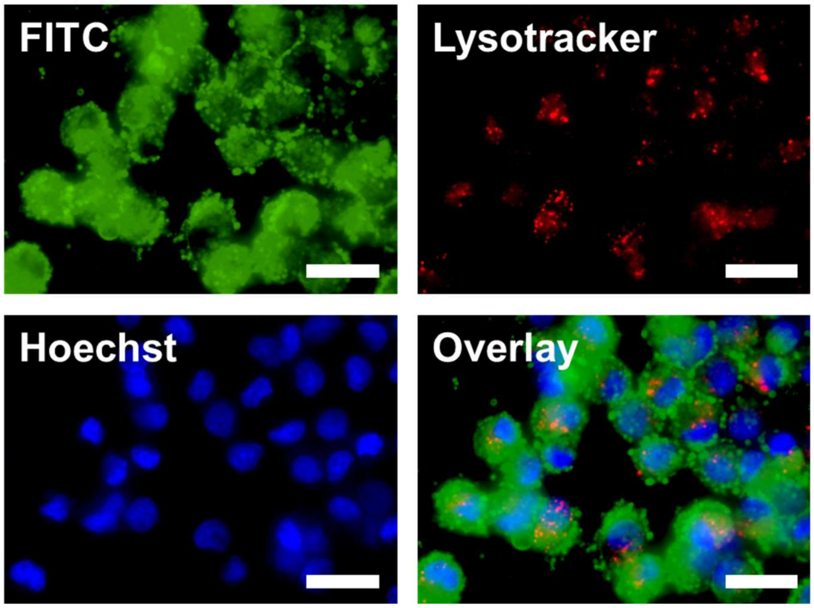

Figure 3.14 Fluorescence microscopic images of co-assembled K10-E3 (95%) and FITC-K10 (5%) for 24 hs. Scale bar = 25 mm.

3.3 Conclusions

In conclusion, modularly designed MDPs as the molecular building block was used to study supramolecular peptides' self-assemble correlated cell penetrating activity. The supramolecular nanostructure is designed to be tuned by the ratio of the cationic and anion domain on MDPs to control the energetic balance between the attractive and repulsive interactions involved in the self-assembly. AUC and TEM confirmed the peptide nanostructure formation of nanofibers and spherical micelles for different MDPs and both supramolecular assemblies exhibit much higher cell penetrating activity than monomeric MDPs. It was found that supramolecular nanofibers can further enhance the cell penetrating activity of MDPs while showing excellent cytocompatibility. Through these preliminary findings, we have established a rationale for a peptide self-assembly mechanism by which SPCNs can be generated. Future efforts will focus on expanding the library of MDPs with diverse chemical functionality for further activity optimization as well as the development of disease-responsive SPCNs for targeted molecular imaging and therapy applications.

3.4 Experimental Section

General Methods

4-Methylbenzhydrylamine (MBHA) rink amide resin, Fmoc-protected amino acids, 2-(1H-benzotriazol-1-yl)-1,1,3,3-tetramethyluronium hexafluorophosphate (HBTU), 5(6)-carboxylfluoresceinpiperidine, diisopropylethylamine (DIPEA), α-cyano-4-hydroxycinnamic acid, methyl-b-cyclodextrin, amiloride and filipin III were purchased from Sigma-Aldrich. Trifluoroacetic acid (TFA), triisopropylsilane (TIS), acetonitrile (ACN), dimethylformamide (DMF), acetic anhydride were purchased from Fisher Scientific and used as received. Dulbecco's modified Eagle medium (DMEM), LysoTracker Red DND-99 and Hoechst

33342 were purchased from Life Technologies. Fetal Bovine Serum (FBS) was purchased from VWR. CCK8 assay kit was obtained from Dojindo Molecular Technologies (Rockville, MD). Transmission Electron Microscopy (TEM) grids and uranium acetate dihydrate were purchased from Ted Pella, Inc.

Peptides Synthesis and Purification

The synthetic procedure followed the standard Fmoc-solid phase peptide synthesis method on a *Prelude*® peptide synthesizer. In brief, the synthesis was set up for either 30 μmol scale using MBHA rink amide resin. The Fmoc group was deprotected in the presence of 20% (V/V) piperidine/DMF for 5 minutes and repeated once. The coupling reaction was carried out for 30 mins by adding Fmoc-protected amino acids, HBTU and DIPEA with a molar ratio of 4:4:8 with respect to the amino groups on the MBHA rink amide resin. After the completion of the synthesis, the N-terminus of the MDPs was acetylated using DIPEA and acetic anhydride in DMF for 1 h. Kaiser test was performed to confirm the completion of the acetylation reaction. The acetylated peptide was cleaved in a mixture of TFA/TIS/ H_2O (95/2.5/2.5 by volume) for 3 hs. The cleavage solution was filtered, and the filtrates were collected. The resin was washed three times with neat TFA, and all filtrate solutions were combined and evaporated under airflow. The residual peptide solution was precipitated in cold diethyl ether, followed by centrifugation and washing with cold diethyl ether for three times. The crude peptide was dried under vacuum overnight for HPLC purification. Peptides were purified using a preparative reverse phase C4 column with a linear gradient of H_2O/ACN (5% to 95% of acetonitrile in 30 mins) containing 0.05% TFA and the elution was monitored at both 230 nm and 280 nm. The HPLC fraction was collected, combined and lyophilized for 2 days. Fluorescein terminated peptides were synthesized as follows. After the final deprotection of the Fmoc group, peptide resin was treated with 4 equivalents of 5(6)-carboxyl fluorescein (FITC), 4 equivalents of HBTU and 8 equivalents of DIPEA in DMF. The reaction mixture was stirred overnight. The completion of the coupling reaction was confirmed by the Kaiser test. The cleavage and purification steps followed the same procedure as described above. The molecular weight of each peptide was characterized and confirmed by MALDI-TOF mass spectrometry using α-cyano-4-hydroxycinnamic acid as the matrix. K10: expected $[M+H]^+$: 3225.8, observed $[M+H]^+$: 3226.7; K10-E2: expected $[M+H]^+$: 3483,9, observed $[M+H]^+$: 3482.5; K12-E3: expected $[M+H]^+$: 3869.1, observed $[M+H]^+$: 3869.6; K10-E3: expected $[M+H]^+$: 3612.9, observed $[M+H]^+$: 3612.0; F-K10: expected $[M+H]^+$: 3542.1, observed $[M+H]^+$: 3544.1. For all the experiments, peptide stock solution was prepared by dissolving lyophilized peptide powder in Tris buffer (20 mM, pH=7.4) to reach a final concentration at 1 mM and left at 4°C for a day.

Circular Dichroism (CD) Spectroscopy

Peptide solutions were diluted to 20 μM in Tris buffer (pH 7.4, 20 mM) for CD measurements on a Jasco-J710 spectrometer. The CD spectra were collected from 250 nm to 190 nm at room temperature using a 2 mm cuvette, a bandwidth at 0.1 nm, scan rate at 100 nm/min and a response time of 2 sec. Each spectrum was averaged from three scans. The mDeg of rotation was converted to the molar residual ellipticity using the following formula

$\theta = \frac{1000 \times mDeg}{c * n * l}$, where c is the concentration of the peptide solution in mM, n is the number of amino acids in the peptide sequence and l is the path length of the cell used in mm.

Transmission Electron Microscopy (TEM)

TEM was performed on a Hitachi H-9500 High-resolution TEM instrument. Peptide solutions were diluted to 100 µM in Tris buffer (pH 7.4, 20 mM) for TEM examination. 10 µl of the peptide solution was pipetted onto a holey carbon grid (TED PELLA 01824). After 2 mins, the excess solution was carefully removed with filter paper. 10 µl of 2 wt% uranyl acetate solution was dropped onto the grid for negative staining. The excess staining solution was removed with filter paper after 2 mins. The TEM sample was dried overnight before imaging.

Critical Aggregation Concentration (CAC) Measurement

CACs were determined using a previous protocol based on the fluorescence intensity change of tryptophan.[29-30] Fluorescence measurements were taken on a Varian Cary Eclipse fluorescence spectrophotometer Increments of 2 µL of a 400 µM peptide solution was added to 500 µL Tris buffer (pH 7.4, 20 mM). Fluorescence emission spectra were acquired after each peptide addition from 295 nm to 440 nm using an excitation wavelength at 280 nm. Fluorescence intensity at 350 nm was plotted as a function of peptide concentrations for CAC determination.

Analytical Ultracentrifugation

Sedimentation velocity experiments were performed on a Beckman-Coulter Optima XL-I analytical ultracentrifuge equipped with an An-50 Ti 8-hole rotor. Double-sector centerpieces sandwiched between sapphire windows in a standard cell housing were loaded with 400 μL of sample and an equal volume of reference buffer (20 mM Tris buffer, pH 7.4). After 2 hs of equilibration under vacuum at 20 °C, samples were centrifuged at 50,000 rpm. Data was acquired using UV absorbance optics tuned to 280 nm for each sample. Sedimentation velocity data was fitted to a continuous *c(s)* distribution model using SEDFIT software. The buffer density and viscosity at room temperature were determined to be 0.99880 g/mL and 0.01007 cP, respectively using SEDNTERP. The partial-specific volume was estimated at 0.75330 mL/g for K10, 0.74610 mL/g for K10-E2, 0.74790 mL/g for K12-E3 and 0.74290 mL/g for K10-E3. A resolution of 50 was utilized with a regularization level of 0.68. Time-invariant noise elements were removed from the data. All figures featuring *c(s)* distributions were generated in GUSSI software.[44]

Cell Uptake

DMEM containing 10% FBS was used as the culture medium for all *in vitro* experiments**.** For the cell uptake study, peptide samples were prepared as follows. Each peptide, namely K10, K10-E2, K12-E3 and K10-E3 was mixed with FITC-labeled K10 with a molar ratio of 95:5 in a mixed solvent of water and acetonitrile (1:1 by volume). The mixture was lyophilized and rehydrated in Tris buffer (pH 7.4, 20 mM) to form FITC-labeled co-assembly at a final concentration of 1 mM and left at 4°C for a day. HeLa cells were seeded onto a confocal dish at a density of 10^5 cells/well and incubated overnight at 37 °C in an incubator with 5% of CO_2. After 24 hs, DMEM culture medium was refreshed. Co-assembled peptides were diluted in Tris buffer to reach a final concentration at 200 μM. 20 μL of the diluted peptide solution was added to the culture medium to reach a final concentration at 20 μM. After 2 hs and 24 hs of incubation, cells were stained with nucleus staining dye, Hoechst 33342 at 37 °C for 15 min and washed with PBS buffer for three times. For lysotracker staining, peptide containing culture medium was removed and stained with LysoTracker Red DND-99 at 37 °C for 1 h, followed by staining with the nucleus staining dye, Hoechst 33342 at 37 °C for 15 min. Images were captured using an Olympus IX71 Inverted fluorescence microscope and processed with ImageJ software.

For endocytosis-inhibition examination, HeLa cells were seeded onto a confocal dish at a density of 10^5 cells/well and incubated overnight at 37 °C in an incubator with 5% of CO_2. Co-assembled K10-E3 was prepared using the same procedure. After 24 hs, the culture medium was replaced with fresh medium containing 5 mM of methyl-b-cyclodextrin, 5 mM of amiloride or 5 mg/ml filipin III. After 1 h, the culture media containing different endocytosis inhibitors were replaced with refresh medium. FITC-labelled co-assembled K10-E3 was added into the culture to reach a final concentration of 20 μM. After 24 hs of incubation, cells were stained with nucleus staining dye, Hoechst 33342 at 37 °C for 15 min and washed three times with PBS buffer. Images were captured using an Olympus IX71 Inverted fluorescence microscope and processed with ImageJ software.

Flow Cytometry

HeLa cells were seeded onto a 24-well plate at a density of 10^5 cells/well and incubated for 24 hs at 37 °C with 5% of CO_2. Co-assembled peptides were prepared using the same procedure as cell uptake. The culture medium was replaced with 450 μL fresh DMEM medium and 50 μL of co-assembled peptides solutions (200 μM) were added. After 24 hs, the culture medium was removed, and cells were washed with PBS buffer three times. Cells were digested with trypsin and washed twice with PBS buffer. 2% paraformaldehyde was used for cell fixation. The mean fluorescence intensity of cells upon different peptide treatment was quantified using a The BD LSR II flow cytometer. A minimum of 10,000 events per sample was analyzed and data were processed using FlowJo software.

For endocytosis-inhibition examination, HeLa cells were seeded onto a 24-well plate at a density of 10^5 cells/well and incubated for 24 hs at 37 °C with 5% of CO_2. Co-assembled K10-E3 was prepared using the same procedure as cell uptake. After 24 hs, the culture medium was replaced with fresh medium containing 5 mM of methyl-b-cyclodextrin, 5 mM of amiloride or 5 mg/ml filipin III. After 1 h, the culture media containing different endocytosis inhibitors were removed and replaced with 450 μL fresh DMEM medium and 50 μL of co-assembled K10-E3 solution (200 μM). After 24 hs, culture medium was removed, and cells were washed three times with PBS buffer. Cells were digested with trypsin and washed twice with PBS buffer followed by cell fixation with 2% paraformaldehyde. The mean fluorescence intensity of cells upon different peptide treatment was quantified using a BD LSR II flow cytometer. A minimum of 10,000 events per sample was analyzed and data were processed using FlowJo software.

Cytotoxicity Measurement

HeLa cells were seeded onto a 96-well plate at a density of 10^4 cells/well and incubated at 37 °C in an incubator with 5% of CO_2. After 24 hs, DMEM culture medium (10% FBS) was removed. 10 μL of diluted peptide solution in Tris buffer (pH 7.4, 20mM) at various concentrations (800, 400, 200, 100, 50, 25, 12.5 μM) were mixed with 90 μL DMEM culture medium in the 96-well plate. After 24 hs of incubation, the CCK8 assay was performed to quantify the cell viability by monitoring the UV absorbance at 450 nm. Cells incubated with 10 μL of Tris buffer were used as a control group. All experiments were performed in four replicates.

Statistical Analysis

All data were expressed as means ± standard deviation (SD). The statistical analysis was performed using Student's T-test and one-way analysis of variance (ANOVA) at confidence levels of 95%.

3.5 References

1. Zorko, M.; Langel, U., Cell-penetrating peptides: mechanism and kinetics of cargo delivery. *Adv. Drug. Deliv. Rev.* **2005,** *57* (4), 529-45.
2. Torchilin, V. P., Tat peptide-mediated intracellular delivery of pharmaceutical nanocarriers. *Adv. Drug. Deliv. Rev.* **2008,** *60* (4-5), 548-58.
3. Frankel, A. D.; Pabo, C. O., Cellular uptake of the tat protein from human immunodeficiency virus. *Cell* **1988,** *55* (6), 1189-1193.
4. Green, M.; Loewenstein, P. M., Autonomous functional domains of chemically synthesized human immunodeficiency virus tat trans-activator protein. *Cell* **1988,** *55* (6), 1179-1188.
5. Morris, M. C.; Depollier, J.; Mery, J.; Heitz, F.; Divita, G., A peptide carrier for the delivery of biologically active proteins into mammalian cells. *Nat. Biotechnol.* **2001,** *19* (12), 1173-1176.
6. Yin, L.; Song, Z.; Kim, K. H.; Zheng, N.; Tang, H.; Lu, H.; Gabrielson, N.; Cheng, J., Reconfiguring the architectures of cationic helical polypeptides to control non-viral gene delivery. *Biomaterials* **2013,** *34* (9), 2340-9.
7. Sgolastra, F.; Deronde, B. M.; Sarapas, J. M.; Som, A.; Tew, G. N., Designing mimics of membrane active proteins. *Acc. Chem. Res.* **2013,** *46* (12), 2977-2987.
8. Fischer, D.; Li, Y.; Ahlemeyer, B.; Krieglstein, J.; Kissel, T., In vitro cytotoxicity testing of polycations: influence of polymer structure on cell viability and hemolysis. *Biomaterials* **2003,** *24* (7), 1121-1131.
9. Cai, J.; Yue, Y.; Rui, D.; Zhang, Y.; Liu, S.; Wu, C., Effect of Chain Length on Cytotoxicity and Endocytosis of Cationic Polymers. *Macromolecules* **2011,** *44* (7), 2050-2057.
10. Hauser, C. A.; Zhang, S., Designer self-assembling peptide nanofiber biological materials. *Chem. Soc. Rev.* **2010,** *39* (8), 2780-90.
11. Yan, C.; Pochan, D. J., Rheological properties of peptide-based hydrogels for biomedical and other applications. *Chem. Soc. Rev.* **2010,** *39* (9), 3528-40.
12. Wang, H.; Feng, Z.; Xu, B., Supramolecular Assemblies of Peptides or Nucleopeptides for Gene Delivery. *Theranostics* **2019,** *9* (11), 3213-3222.
13. Raymond, D. M.; Nilsson, B. L., Multicomponent peptide assemblies. *Chem. Soc. Rev.* **2018,** *47* (10), 3659-3720.
14. Hudalla, G. A.; Sun, T.; Gasiorowski, J. Z.; Han, H.; Tian, Y. F.; Chong, A. S.; Collier, J. H., Gradated assembly of multiple proteins into supramolecular nanomaterials. *Nat. Mater.* **2014,** *13* (8), 829-36.
15. Moore, A. N.; Hartgerink, J. D., Self-Assembling Multidomain Peptide Nanofibers for Delivery of Bioactive Molecules and Tissue Regeneration. *Acc. Chem. Res.* **2017,** *50* (4), 714-722.
16. Cui, H.; Webber, M. J.; Stupp, S. I., Self-assembly of peptide amphiphiles: from molecules to nanostructures to biomaterials. *Biopolymers* **2010,** *94* (1), 1-18.
17. Branco, M. C.; Sigano, D. M.; Schneider, J. P., Materials from peptide assembly: towards the treatment of cancer and transmittable disease. *Curr. Opin. Chem. Biol.* **2011,** *15* (3), 427-34.

18. Acar, H.; Srivastava, S.; Chung, E. J.; Schnorenberg, M. R.; Barrett, J. C.; LaBelle, J. L.; Tirrell, M., Self-assembling peptide-based building blocks in medical applications. *Adv. Drug Deliv. Rev.* **2017,** *110-111*, 65-79.
19. Boyle, A. L.; Woolfson, D. N., De novo designed peptides for biological applications. *Chem. Soc. Rev.* **2011,** *40* (8), 4295-306.
20. Deming, T. J., Polypeptide materials: new synthetic methods and applications. *Adv. Mater.* **1997,** *9* (4), 299-311.
21. Zhang, H.; Park, J.; Jiang, Y.; Woodrow, K. A., Rational design of charged peptides that self-assemble into robust nanofibers as immune-functional scaffolds. *Acta. Biomater.* **2017,** *55*, 183-193.
22. Yang, M.; Xu, D.; Jiang, L.; Zhang, L.; Dustin, D.; Lund, R.; Liu, L.; Dong, H., Filamentous supramolecular peptide-drug conjugates as highly efficient drug delivery vehicles. *Chem. Commun.* **2014,** *50* (37), 4827-30.
23. Zhang, S.; Holmes, T.; Lockshin, C.; Rich, A., Spontaneous assembly of a self-complementary oligopeptide to form a stable macroscopic membrane. *Proc. Natl. Acad. Sci. U.S.A.* **1993,** *90* (8), 3334-3338.
24. Rudra, J. S.; Sun, T.; Bird, K. C.; Daniels, M. D.; Gasiorowski, J. Z.; Chong, A. S.; Collier, J. H., Modulating adaptive immune responses to peptide self-assemblies. *Acs Nano* **2012,** *6* (2), 1557-1564.
25. Yang, S.; Xu, D.; Dong, H., Design and fabrication of reduction-sensitive cell penetrating nanofibers for enhanced drug efficacy. *J. Mater. Chem. A* **2018,** *6* (44), 7179-7184.
26. Xu, D.; Samways, D. S. K.; Dong, H., Fabrication of self-assembling nanofibers with optimal cell uptake and therapeutic delivery efficacy. *Bioact. Mater.* **2017,** *2* (4), 260-268.
27. Xu, D.; Jiang, L.; DeRidder, L.; Elmore, B.; Bukhari, M.; Wei, Q.; Samways, D.; Dong, H., Membrane activity of a supramolecular peptide-based chemotherapeutic enhancer. *Mol. Biosyst.* **2016,** *12* (9), 2695-2699.
28. Xu, D.; Dustin, D.; Jiang, L.; Samways, D. S.; Dong, H., Designed filamentous cell penetrating peptides: probing supramolecular structure-dependent membrane activity and transfection efficiency. *Chem. Commun.* **2015,** *51* (59), 11757-60.
29. Chen, Y.; Barkley, M. D., Toward understanding tryptophan fluorescence in proteins. *Biochemistry* **1998,** *37* (28), 9976-9982.
30. Xu, D.; Ran, Q.; Xiang, Y.; Linhai, J.; Smith, B. M.; Bou-Abdallah, F.; Lund, R.; Li, Z.; Dong, H., Toward Hemocompatible Self-assembling Antimicrobial Nanofibers: Understanding the Synergistic Effect of Supramolecular Structure and PEGylation on Hemocompatibility. *RSC Adv.* **2016,** *6* (19), 15911-15919.
31. Wang, S. T.; Lin, Y.; Spencer, R. K.; Thomas, M. R.; Nguyen, A. I.; Amdursky, N.; Pashuck, E. T.; Skaalure, S. C.; Song, C. Y.; Parmar, P. A.; Morgan, R. M.; Ercius, P.; Aloni, S.; Zuckermann, R. N.; Stevens, M. M., Sequence-Dependent Self-Assembly and Structural Diversity of Islet Amyloid Polypeptide-Derived beta-Sheet Fibrils. *ACS Nano* **2017,** *11* (9), 8579-8589.

32. Searle, M. S.; Griffiths-Jones, S. R.; Skinner-Smith, H., Energetics of weak interactions in a β-hairpin peptide: Electrostatic and hydrophobic contributions to stability from lysine salt bridges. *J. Am. Chem. Soc.* **1999,** *121* (50), 11615-11620.

33. Whitney, M.; Savariar, E. N.; Friedman, B.; Levin, R. A.; Crisp, J. L.; Glasgow, H. L.; Lefkowitz, R.; Adams, S. R.; Steinbach, P.; Nashi, N.; Nguyen, Q. T.; Tsien, R. Y., Ratiometric activatable cell-penetrating peptides provide rapid in vivo readout of thrombin activation. *Angew Chem. Int. Ed. Engl.* **2013,** *52* (1), 325-30.

34. Jiang, T.; Olson, E. S.; Nguyen, Q. T.; Roy, M.; Jennings, P. A.; Tsien, R. Y., Tumor imaging by means of proteolytic activation of cell-penetrating peptides. *Proc. Natl. Acad. Sci. U.S.A.* **2004,** *101* (51), 17867-17872.

35. Chen, W.; Yang, S.; Li, S.; Lang, J. C.; Mao, C.; Kroll, P.; Tang, L.; Dong, H., Self-Assembled Peptide Nanofibers Display Natural Antimicrobial Peptides to Selectively Kill Bacteria without Compromising Cytocompatibility. *ACS Appl. Mater. Interfaces* **2019,** *11* (32), 28681-28689.

36. Peng, H.; Varanasi, S.; Wang, D. K.; Blakey, I.; Rasoul, F.; Symons, A.; Hill, D. J. T.; Whittaker, A. K., Synthesis, swelling, degradation and cytocompatibility of crosslinked PLLA-PEG-PLLA networks with short PLLA blocks. *Eur. Polym. J.* **2016,** *84*, 448-464.

37. Chandorkar, Y.; Bhagat, R. K.; Madras, G.; Basu, B., Cross-linked, biodegradable, cytocompatible salicylic acid based polyesters for localized, sustained delivery of salicylic acid: an in vitro study. *Biomacromolecules* **2014,** *15* (3), 863-75.

38. Bera, A.; Singh Chandel, A. K.; Uday Kumar, C.; Jewrajka, S. K., Degradable/cytocompatible and pH responsive amphiphilic conetwork gels based on agarose-graft copolymers and polycaprolactone. *J. Mater. Chem. B* **2015,** *3* (43), 8548-8557.

39. Breunig, M.; Lungwitz, U.; Liebl, R.; Goepferich, A., Breaking up the correlation between efficacy and toxicity for nonviral gene delivery. *Proc. Natl. Acad. Sci. U.S.A.* **2007,** *104* (36), 14454-14459.

40. Kauffman, W. B.; Fuselier, T.; He, J.; Wimley, W. C., Mechanism Matters: A Taxonomy of Cell Penetrating Peptides. *Trends Biochem. Sci.* **2015,** *40* (12), 749-764.

41. Kauffman, W. B.; Guha, S.; Wimley, W. C., Synthetic molecular evolution of hybrid cell penetrating peptides. *Nat. Commun.* **2018,** *9* (1), 2568.

42. Lim, K. J.; Sung, B. H.; Shin, J. R.; Lee, Y. W.; Kim, D. J.; Yang, K. S.; Kim, S. C., A cancer specific cell-penetrating peptide, BR2, for the efficient delivery of an scFv into cancer cells. *PLoS One* **2013,** *8* (6), e66084.

43. Gomez, J. A.; Chen, J.; Ngo, J.; Hajkova, D.; Yeh, I. J.; Gama, V.; Miyagi, M.; Matsuyama, S., Cell-Penetrating Penta-Peptides (CPP5s): Measurement of Cell Entry and Protein-Transduction Activity. *Pharmaceuticals* **2010,** *3* (12), 3594-3613.

44. Brautigam, C. A., Calculations and Publication-Quality Illustrations for Analytical Ultracentrifugation Data. *Methods Enzymol* **2015,** *562*, 109-33.

Chapter 4. Enzyme-Responsive Peptide Self-Assembly[*]

4.1 Introduction

Membrane-active peptides are an important class of materials which function by interacting with the cell membrane to cause membrane disruption or direct translocation for cargo delivery.[1-4] The majority of these peptides adopt a global amphiphilic conformation upon membrane binding in which cationic and hydrophobic amino acids are segregated into clusters on the opposite faces of a peptide secondary structure, commonly an α-helix or β-sheet. While global amphiphiles are a common motif for the design of membrane-active molecules and polymers, recent efforts suggested preorganization of locally clustered facial or linear amphiphiles on a macromolecular backbone prior to membrane binding can be an effective approach to further increase membrane activity.[5-8] This is largely due to the reduced entropic loss associated with a membrane-induced conformational change of pre-assembled amphiphilic clusters. It was shown a rigid backbone, such as a long α-helix forming polypeptide, is more favorable for inducing an ordered global arrangement of the amphiphilic clusters while maintaining sufficient local conformational flexibility needed for effective membrane interactions. Using the approach of supramolecular peptide assembly, our group reported a library of membrane-active nanofibers in which local amphiphilic clusters are presented on a rigid self-assembled β-sheet peptide nanofibers to induce potent membrane activity.[9-13]

---

[*] This chapter is based on Su Yang et al. Modular Design of Supramolecular Ionic Peptides with Cell-Selective Membrane Activity. *Chembiochem.*, **2021**, 22, 3164-3168. Some sections were rearranged for continuity.

A general strategy for the construction of membrane-active nanofibers involves self-assembly of a *de novo* designed cationic multidomain peptide (MDP) which has the tendency to form supramolecular β-sheet nanofibers. As demonstrated in our previous studies, the emerging membrane activity is largely attributed to the formation of supramolecular nanofibers as constitutional peptide isomers which have the same secondary structures but exist as monomers or small oligomers had much lower membrane activity.[9, 13] Upon self-assembly, supramolecular ionic clusters are displayed on the rigid nanofiber backbone and their conformational flexibility can be further tuned by changing the numbers of cationic and anionic amino acids on MDPs to enhance the membrane activity.

4.2 Results and Discussion

4.2.1 Peptide Design

Inspired by the work on proteolytically activated cell penetrating peptides along with recent advances in trigger-responsive peptide self-assembly,[14-26] in this work, we aim to fabricate nanofibers with control over membrane activity in a cell-selective manner by trigger-responsive. The design of peptide precursors is to achieve enzymatic-mediated molecular transformation and supramolecular assembly of modularly designed MDPs. Upon self-assembling of peptides, the ability of these formed nanofibers to perturb cell membranes is retrieved. It is worth mentioning that our approach to achieving cell selective membrane activity is different from the previous report of conjugation of a shielded natural cell penetrating peptide on a nanoparticle surface which is re-activated upon enzymatic cleavage at the target site.[27-28] Rather, we used a modular self-assembly approach in which monomeric peptides with low membrane activity undergo enzyme-triggered chemical transformation followed by self-assembly to form supramolecular nanofibers with enhanced membrane activity.

Fig. 4.1 shows the chemical structure of a modularly designed MDP which can undergo a selective chemical transformation and supramolecular assembly to form membrane-active nanofibers. The MDP is designed to have three modules. A key module is a membrane-active self-assembling (SA) module, the sequence of which was optimized through our previous screening studies.[13] In this work, we selected fiber forming $K_{10}(QW)_6E_3$ as the membrane-active SA module in which the subscript represents the numbers of repeating units for lysine (K), glutamic acid (E) and the alternating glutamine (Q) and tryptophan (W). A cationic capping (CC) module consisting of oligolysines is attached to the C-terminus of the SA module through a labile linker (LL) module. The hypothesis is in the presence of the cationic CC domain, due to the abundance of the cationic charges and increased electrostatic repulsion, MDPs do not self-assemble and therefore have weak membrane activity. When the external stimulus is applied under specific cellular conditions, the LL domain is cleaved to release the CC domain. Due to electrostatic repulsion, the CC domain will not have attached residue upon the cleavage. Consequently, the ability of MDPs to self-assemble is restored to form nanofibers with improved membrane activity. As a proof-of-concept study, we chose matrix metalloproteinase 2, MMP-2 as our initial cellular target due to its overexpression by multiple cancer cells.[29-30] MMPs are also known as model enzymes for the development of various targeted biomaterials.[31-33] We synthesized an MDP consisting of an MMP-2 responsive substrate (PLGLAG) as the linker, termed CS-MDP and a control MDP with a scrambled linker sequence of LALGPG but otherwise identical, termed NS-MDP. Both peptides were investigated for their enzymatic-dependent self-assembly in aqueous buffer solution and membrane activity in cancer cell lines with high and low extracellular MMP-2 levels.

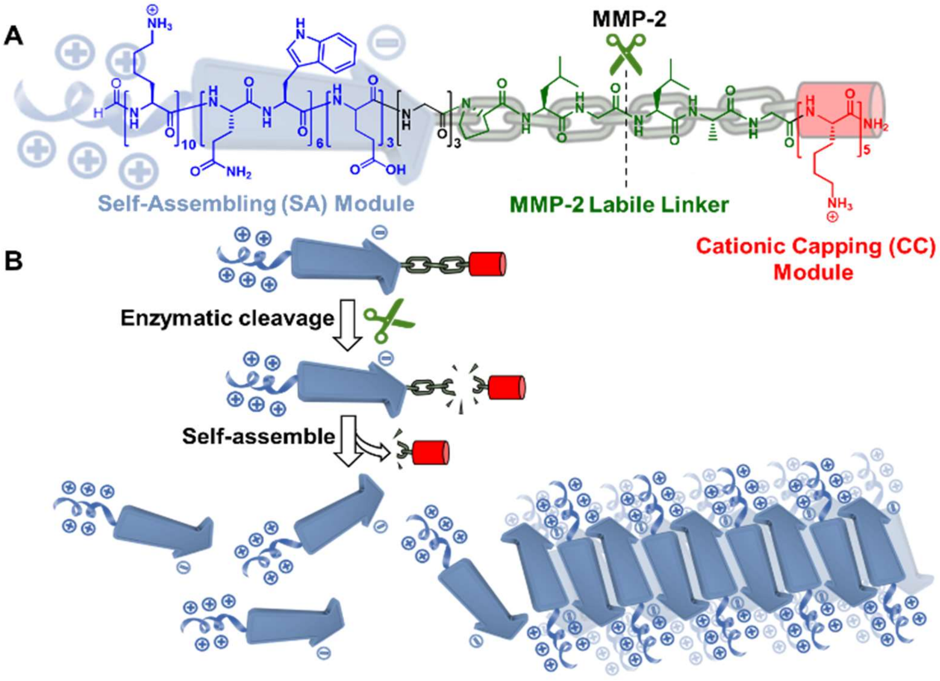

Figure 4.1 Color-coded chemical structure (A) and self-assembly (B) of a modularly designed CS-MDP to form supramolecular cationic nanofibers. Blue: self-assembling (SA) module, $K_{10}(QW)_6E_3$ which has the intrinsic membrane activity upon self-assembly. Green: MMP-2 labile linker, PLGLAG. Red: Cationic capping (CC) module consisting of five lysine residues. Black: Three glycines were included between the SA module and MMP-2 linker. The hypothesis is in the presence of the CC domain, due to the abundance of the cationic charges and electrostatic repulsion, CS-MDPs do not self-assemble and therefore have weak membrane activity. When the external stimulus is applied to remove the CC domain, the self-assembling capability of $K_{10}(QW)_6E_3$ is restored to form supramolecular nanofibers with enhanced membrane activity

4.2.2 Molecular and Supramolecular Structural Characterization

As expected, the CS-MDP is susceptible to being cleaved by MMP-2 and the mass of the peptide fragments confirms the cleavage reaction occurs between glycine and leucine in the LL domain (**Fig. 4.2A**). Using high performance liquid chromatography (HPLC), the

MMP-2 cleavage efficiency was determined to be 69% after 4 hs of enzymatic treatment, which further increased to 95% after 24 hs of incubation (**Fig. 4.2B**).

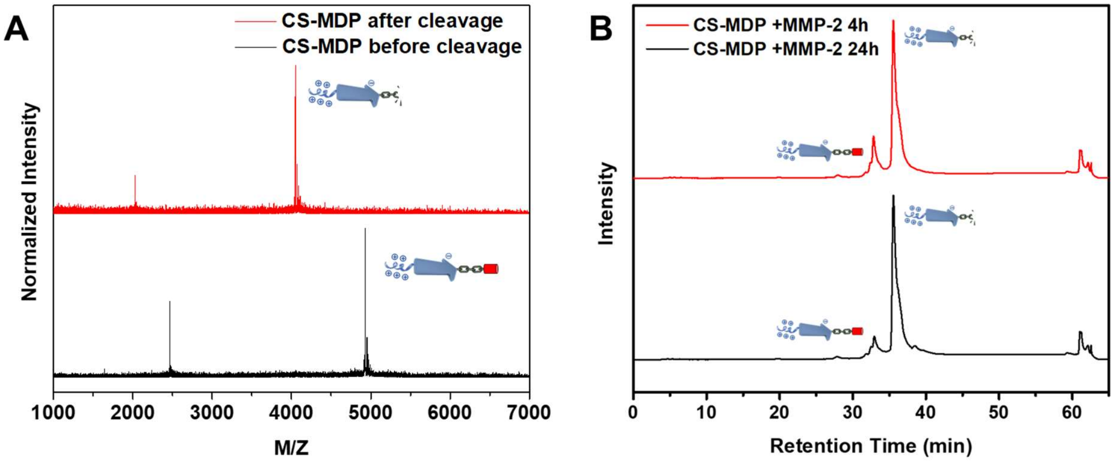

Figure 4.2 (A) MALDI mass spectrometry characterization of CS-MDP before and after MMP-2 cleavage in buffer (Tris 20 mM, $CaCl_2$ 5 mM, $ZnCl_2$ 20 mM, pH = 7.4). (B) HPLC elution profiles of CS-MDP after 4 h and 24 h of MMP-2 cleavage in Tris buffer (20 mM, pH = 7.4) containing 5 mM $CaCl_2$ 5 mM and 20 mM $ZnCl_2$.

Circular dichroism (CD) spectroscopy shows a secondary structural transition from a random coil to a predominant β-sheet conformation upon MMP-2 treatment (**Fig. 4.3A**). The minimum absorption at 215 nm became more intense and narrower with the increase in incubation time, suggesting a time-dependent structural transition process. In comparison, peptides with a scrambled MMP-2 linker, NS-MDPs adopted a random coil regardless of MMP-2 treatment (**Fig. 4.4**).

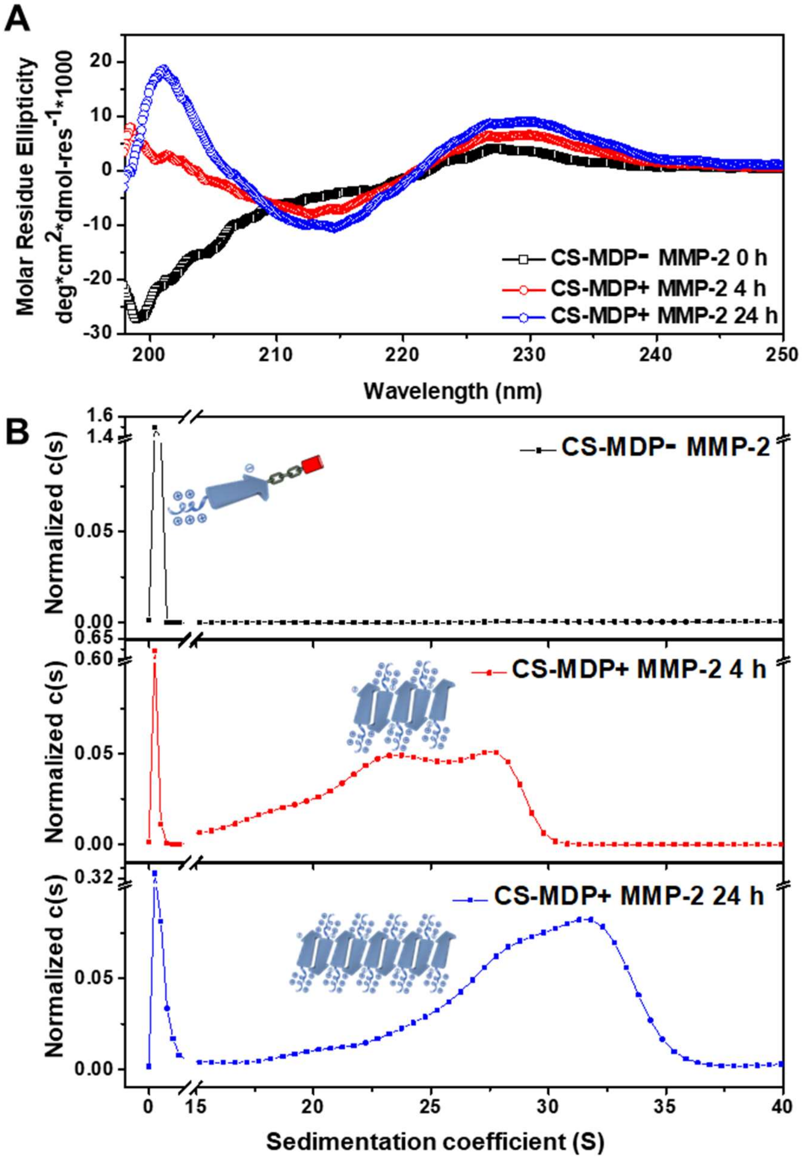

Figure 4.3 (A) CD spectra of CS-MDPs with and without MMP-2 showing enzyme-induced structural transition to β-sheets. (B) Continuous sedimentation coefficient distribution, c(s) curve showing the formation of larger species upon MMP-2 treatment. Peptides were prepared in Tris buffer (20 mM, pH=7.4) containing 5 mM $CaCl_2$ and 20 mM $ZnCl_2$ with a final peptide concentration at 20 μM.

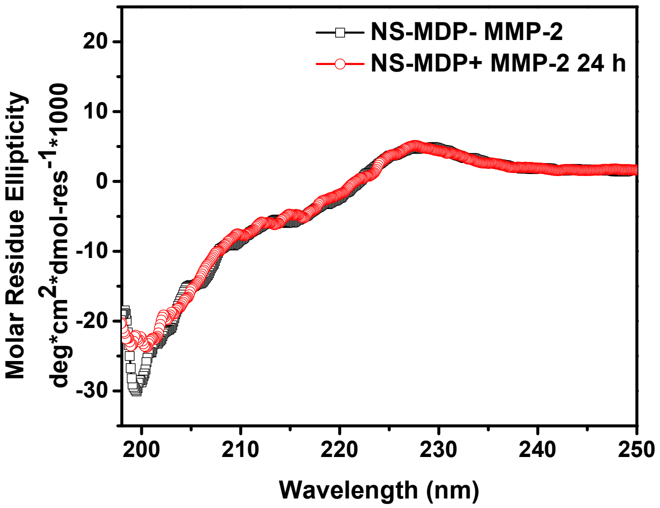

Figure 4.4 Circular dichroism spectroscopy of NS-MDPs with and without MMP-2 treatment. Peptide concentration: 20 μM.

The change in the molecular structure was accompanied by the formation of larger macromolecular species, which were identified through analytical ultracentrifugation (AUC) experiments. Specifically, we performed a sedimentation velocity (SV) experiment to estimate the apparent molecular weight and weight distribution for both CS-MDPs and NS-MDPs in the presence of MMP-2 at different time points and absence of MMP-2 (**Fig. 4.3B and Fig. 4.5**). Without MMP-2 treatment, both peptides exist as monomers with an MW at ~5.1 kDa. This result validates our hypothesis that the electrostatic repulsion among the CC domain is sufficiently strong to prevent peptides from self-assembling. Upon MMP-2 treatment, while NS-MDP still adopted monomers, new species with larger molecular weights were observed for CS-MDPs at ~ 3.4 MDa and ~ 4.9 MDa after 4 hs of incubation with MMP-2. The molecular weight further increases upon extended incubation showing the major population at ~ 4.9 MDa and ~ 5.6 MDa after 24 hs of enzymatic treatment. Based on our design principle, detaching the CC domain from the SA domain causes a reduction of the repulsive forces and therefore shifts the equilibrium toward self-assembly.

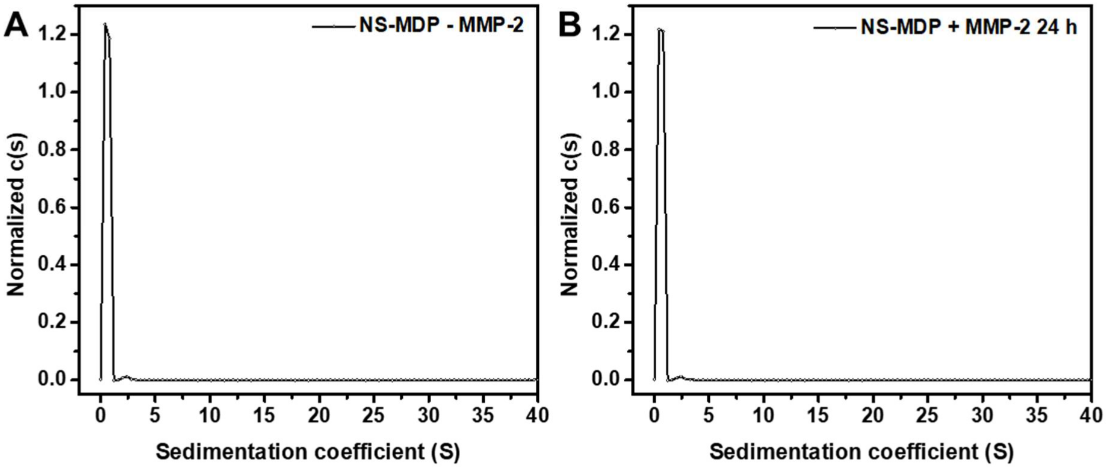

Figure 4.5 Continuous sedimentation coefficient distribution, c(s) curve of NS-MDP (A) in the absence of MMP-2, (B) upon MMP-2 (10 nM) treatment at 37 °C for 24 h. Peptides were prepared in Tris buffer (20 mM, pH=7.4) containing 5 mM $CaCl_2$ and 20 mM $ZnCl_2$ with a final peptide concentration at 20 μM.

Negatively stained transmission electron microscopy (TEM) was further used to examine the self-assembled nanostructures of CS-MDPs upon MMP-2 treatment. TEM shows spherical aggregates for both NS-MDPs and CS-MDPs without MMP-2 (**Fig. 4.6A and Fig. 4.7**), which is likely due to the non-specific aggregation of the monomeric peptides (as confirmed by the solution-state AUC analysis) under the drying sample prepare condition. Upon MMP-2 treatment, while NS-MDPs still adopted spherical aggregates (**Fig. 4.7**), nanofibers were observed for CS-MDPs (**Fig. 4.6B and 4.6C**). Extended incubation of CS-MDPs with the enzyme led to an increase in fiber length from an average of 122 nm at 4 hs to 268 nm at 24 hs (Fig. 4.6D), indicating a time-dependent self-assembly process, which is also consistent with the trend of secondary structure change observed by CD spectroscopy (Fig. 4.3A). Based on the established research, the distance of each structural repeating unit of cross-β sheets is 4.7 Å along the fiber axis,[34] and the average length of nanofibers observed here, we can then calculate the number of peptide chains in a single nanofiber, namely (268 nm/0.47 nm) x 2 in which the factor of 2 reflects the sandwich-like cross-β sheets. As a result, there are approximately 1140 peptide chains in a single nanofiber. Meantime, AUC results showed the average MW of peptide nanofiber upon MMP-2 treatment for 24 hs is at 5.3 MDa. Considering the MW of a single peptide chain at 4935 Da, the number of peptide chains within a nanofiber would be 5.3 x 106 Da/4935 Da = 1070, which is in good agreement with the TEM analysis.

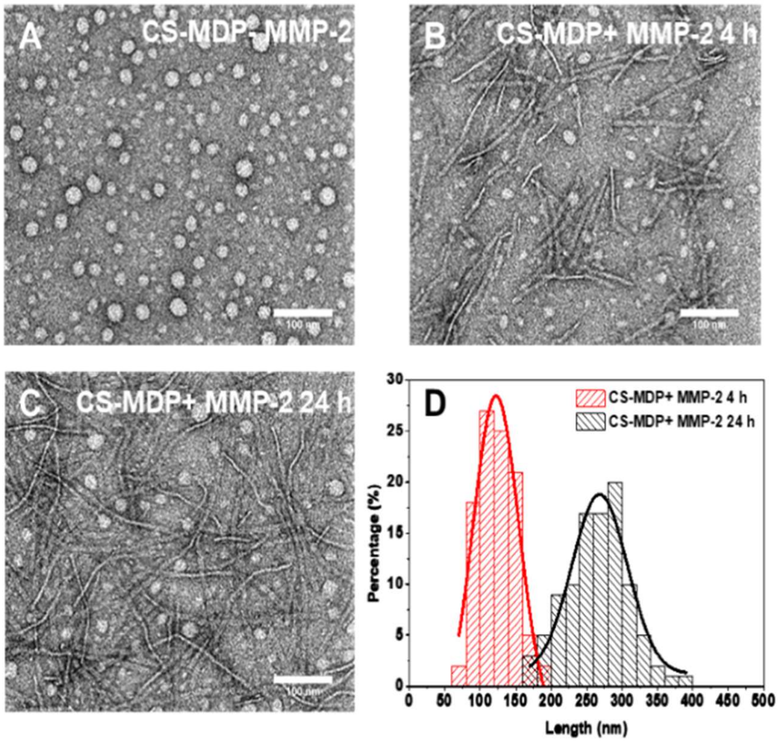

Figure 4.6 TEM images of (A) CS-MDPs in the absence of MMP-2; (B) CS-MDPs treated with MMP-2 for 4 hs; (C) CS-MDPs treated with MMP-2 for 24 hs showing MMP-2 triggered self-assembly to form nanofibers; (D) Quantification of the average fiber length by Gaussian fitting. The measurements were based on a total number of 100 fibers formed by CS-MDPs upon treatment with MMP-2 for 4 hs and 24 hs. Peptides were prepared in Tris buffer (20 mM, pH=7.4) containing 5 mM $CaCl_2$ and 20 mM $ZnCl_2$ with a final peptide concentration at 100 μM.

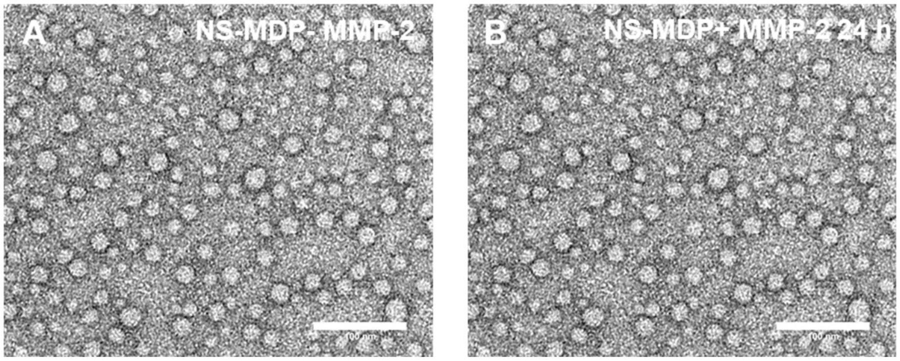

Figure 4.7 TEM images of NS-MDP (A) in the absence of MMP-2, (B) upon MMP-2 (10 nM) treatment at 37 °C for 24 h. Peptide concentration: 100 µm. Scale bar: 100 nm.

4.2.3 Investigation of the Cell-Selective Membrane activity

The peptide precursor has further tested the achievement of enzymatic-triggered formation of supramolecular peptide nanofibers for cell-selective membrane activity. Cell selectivity is largely controlled by the endogenous enzyme secreted by cells. Three cancer cell lines, i.e. esophageal cancer cells (KYSE-30), lung cancer cells (A549) and cervical cancer cells (HeLa), are known to have different levels of endogenous MMP-2, were used to investigate cell-selective membrane activity. The endogenous MMP-2 enzymatic activity in the cell culture media of the three cell lines was quantified through the SensoLyte MMP-2 assay (**Fig. 4.8**) and the results are consistent with the relative activity trend reported in the literature,[35-37] namely KYSE-30 and A549 cells have higher levels of MMP-2 than HeLa cells. It should be noted that the MMP-2 concentration determined in the KYSE-30 and A549 cell culture was ~ 10-fold lower than what is reported *in vivo* at the diseased issues.[38-40] However, despite the reduced MMP-2 activity *in vitro*, induced membrane activity of CS-MDPs was observed.

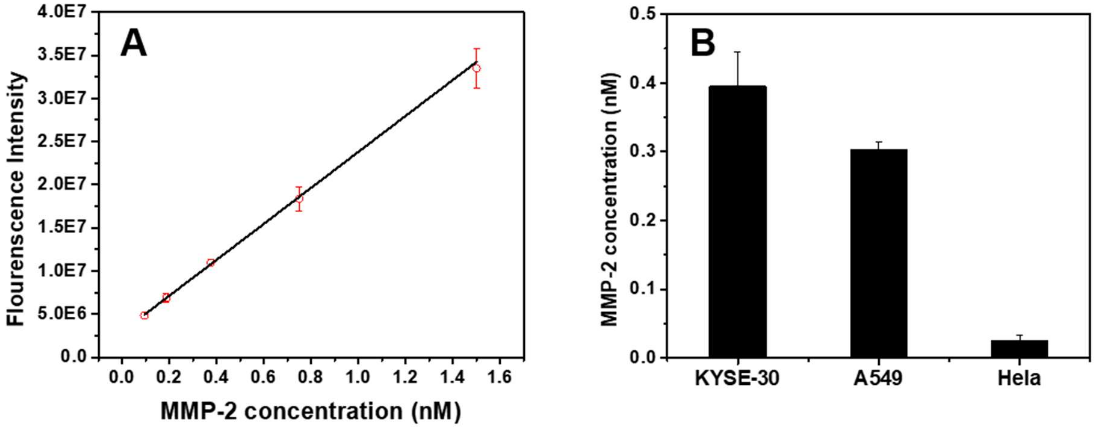

Figure 4.8 (A) standard curve of MMP-2 concentration determined by SensoLyte MMP-2 activity assay, (B) MMP-2 expression level in the culture medium of KYSE-30, A549 and HeLa cells upon 24 h incubation.

We used confocal laser scanning microscopy (CLSM) to monitor cell uptake of fluorescently labeled CS-MDPs and NS-MDPs in which an NBD fluorescence dye was appended at the N-terminus of the SA domain. Peptides were incubated with cells for 24 hs followed by thorough washing before CLSM imaging. As shown in **Fig. 4.9**, upon incubation with CS-MDPs, MMP-2 overexpressed KYSE-30 and A549 cells show much higher fluorescence intensity than HeLa cells which have a low level of endogenous MMP-2. The addition of exogenous MMP-2 to HeLa cell culture dramatically enhanced the fluorescence intensity, further confirming the important role of MMP-2 in activating the membrane activity (**Fig. 4.10**). As shown in **Fig. 4.9A**, much stronger fluorescence is observed for KYSE-30 and A549 cells treated with CS-MDPs than those treated with NS-MDPs. In contrast, fluorescence intensity is comparable between CS-MDP and NS-MDP treated HeLa cells with a low level of endogenous MMP-2. CS-MDPs and NS-MDPs have the same amino acid composition, the only difference is their MMP-2 susceptibility. The enhanced membrane activity of CS-MDPs toward KYSE-30 and A549 cells is mostly attributed to MMP-2 mediated cleavage and self-assembly to form supramolecular cationic clusters while NS-MDPs do not respond to enzymes and therefore remain intact as monomers with low membrane activity. Flow cytometry results show the same trend of fluorescence change, further supporting the role of MMP-2 in the molecular transformation and supramolecular cationic clusters with induced membrane activity (**Fig. 4.9B**). It is notable that although CS-MDPs seem to be mostly localized in the pericellular region of KYSE-30 or A549 cells, they are effective to perturb cell membranes for effective drug delivery.

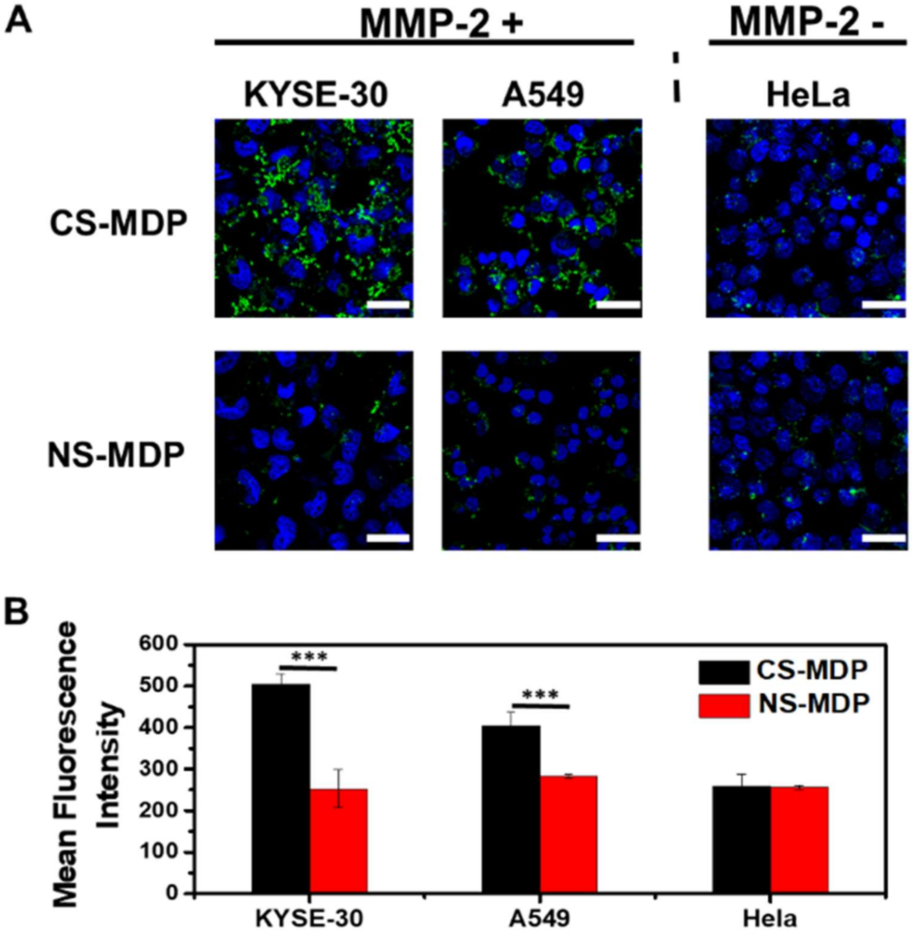

Figure 4.9 (A) CLSM images of cells upon incubation with NBD labeled CS-MDP and NS-MDP showing induced membrane activity of CS-MDP toward MMP-2 overexpressed KYSE-30 and A549 cells in comparison to HeLa cells with a low endogenous level of MMP-2. (B) Flow cytometry measurement of

different cells treated with NBD-labeled CS-MDP and NS-MDP. Incubation time: 24 hs. The final peptide concentration in the culture medium is 20 μM. Scale bar: 50 μm. Statistic significant difference is indicated by ***$p < 0.001$.

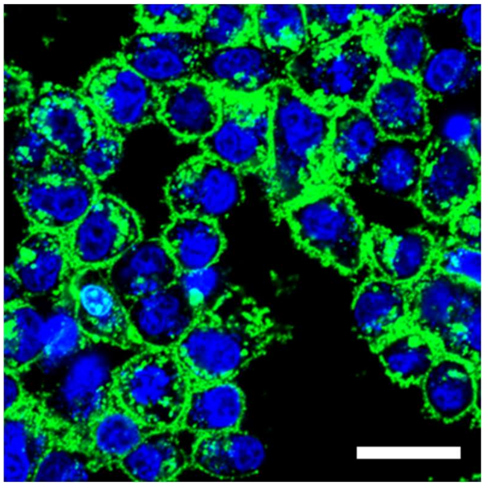

Figure 4.10 CLSM images of HeLa with 3 nM exogenous MMP-2 upon incubation with NBD labeled CS-MDP. Incubation time: 24 hs. Final peptide concentration in the culture medium: 20 μM. Scale bar: 50 μm.

To further correlate the membrane activity with β-sheet nanofiber formation, we performed Congo Red (CR) staining assay in which CR is used to selectively stain cross β-sheet nanofibers.[41-44] In this study due to the toxic of CR to KYSE-30 cell, A549 cell was used as a model cell for this study. As shown in **Fig. 4.11** much higher CR fluorescence is observed for CS-MDP treated A549 than NS-MDP treated cells, suggesting the formation of nanofiber by CS-MDPs and showing the correlation between supramolecular nanofibers and their membrane activity. The absence of green fluorescence is mostly due to the quench by CR.

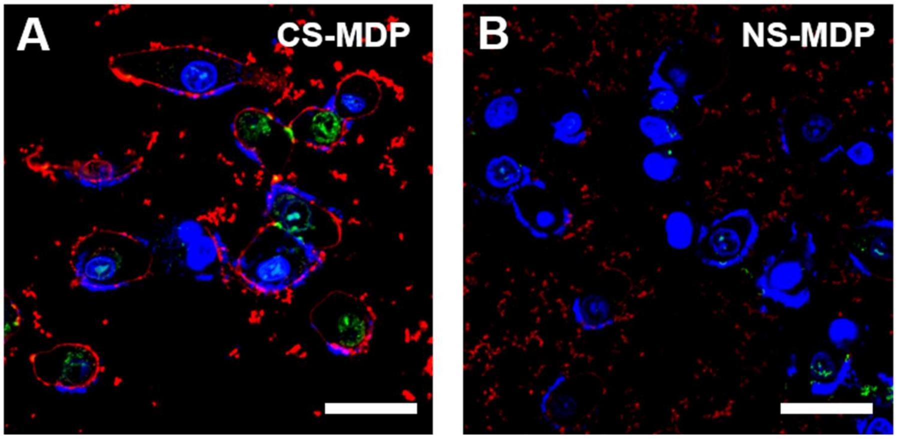

Figure 4.11 CLSM images of A549 cells after incubation with (A) NBD-CS-MDP and (B) NBD-NS-MDP followed by Congo red staining. Peptide concentration: 20 μm. Congo red concentration: 5 μm. Scale bar: 50 μm.

4.2.4 Evaluation of Therapeutic Delivery Efficacy

A preliminary study of *in vitro* drug delivery efficacy was performed using doxorubicin (DOX) as a model anticancer drug molecule to take the benefit of its red fluorescence. A disulfide linker was introduced between DOX and the SA domain in order to release drugs in tumor special reducing cellular microenvironment upon cell uptake or cell membrane interrupt.[12, 44-45] DOX conjugated CS-MDP and NS-MDP termed as DOX-CS-MDP and DOX-NS-MDP (**Table 4.1**) were synthesized through an established procedure using a thiol-disulfide exchange reaction (**Fig. 4.12**).[46] The drug modification strategy has been reported to have no effect on the cytotoxicity of DOX. The disulfide DOX derivative compound used for peptide conjugation was confirmed by 1H-NMR and electrospray ionization mass spectrometry (ESI-MS) (**Fig. 4.13**) and DOX peptide conjugates were confirmed by ESI-MS (**Fig. A-S1(5) and Fig. A-S1(6)**).

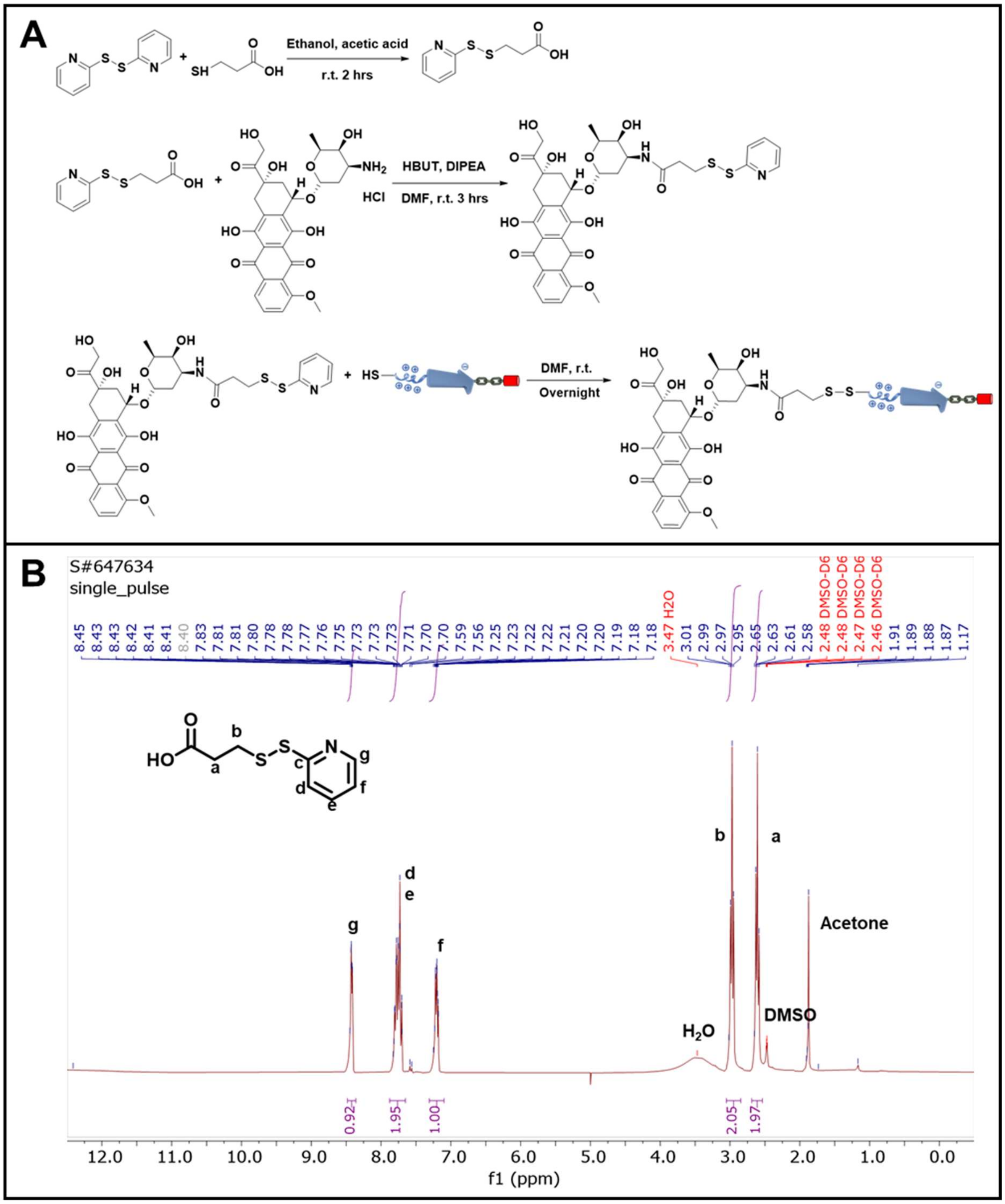

Figure 4.12 (A) Synthetic routes of all the molecular components used for the synthesis of DOX-CS-MDP through thiol-disulfide exchange reaction. (B) ^{1}H-NMR spectrum of Py-SS-MPA in DMSO-D$_6$.

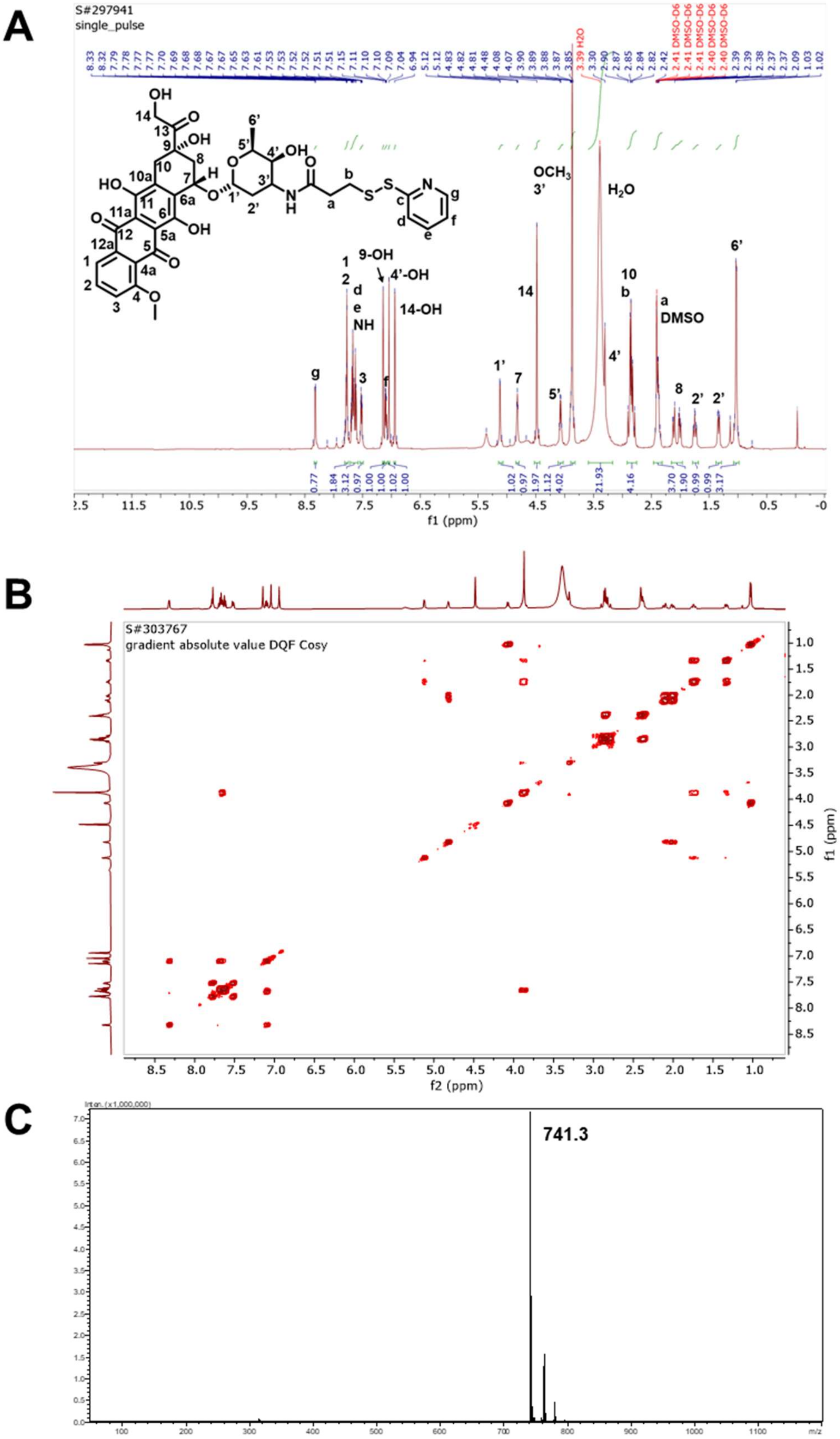

Figure 4.13 (A) ^{1}H NMR of DOX-SS-Py in DMSO-D$_6$. (B) COSY spectrum of DOX-SS-Py in DMSO-D$_6$ and (C) ESI of DOX-SS-Py

Intracellular DOX cleavage and release were confirmed by CLSM showing minimum co-localization of green and red fluorescence in KYSE-30 and A549 cells treated with dual NBD and DOX labeled CS-MDPs, named as DOX-(NBD)CS-MDP (**Table 4.1 and Fig. A-S1(7)**) in which NBD was covalently linked at the N-terminus of CS-MDP (**Fig. 4.14**). The cell periphery localized green fluorescence represents the peptide carrier which is mostly stuck in the cell membrane area, while the cytoplasm and nucleus periphery localized red fluorescence represent the cleaved DOX which was successfully reached the functional region (cell nucleus).

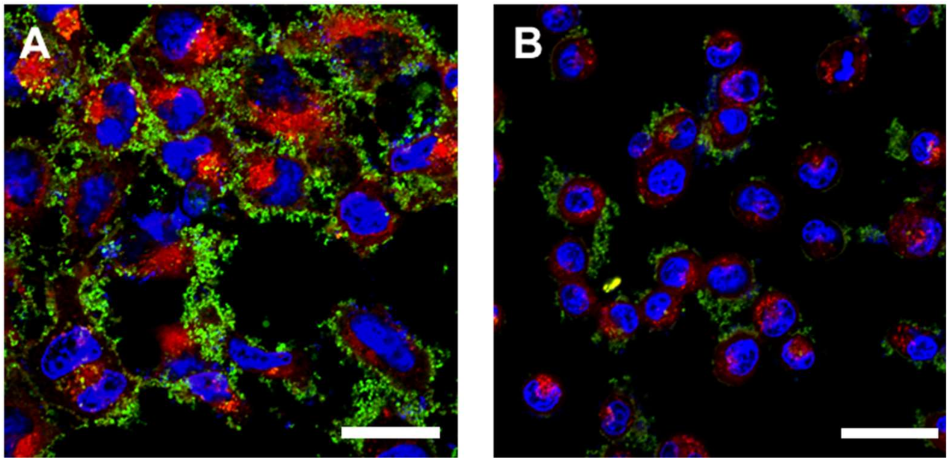

Figure 4.14 CLSM images of (A) KYSE-30 and (B) A549 with 3 nM exogenous MMP-2 upon incubation with NBD labeled DOX conjugated CS-MDP Incubation time: 24 hs. The final peptide concentration in the culture medium: 10 μM. Scale bar: 50 μm.

Cytotoxicity of free DOX, DOX-CS-MDP and DOX-NS-MDP were evaluated against all three cell lines. As shown in **Fig. 4.15A**, while DOX alone elicits moderate cytotoxicity toward three cell lines, DOX-CS-MDP had much higher toxicity toward MMP-2 overexpressed cell lines than low-expression cells, showing cell viability at 23% toward A549, 20% toward KYSE-30 but 90% toward HeLa cells, respectively. In contrast, no prominent selectivity was achieved for DOX-NS-MDP. Also by comparing each cell line, in the MMP-2 overexpressed cell lines, it shown 2.7 fold more cell viability for DOX-NS-MDP compared to DOX-CS-MDP, which demonstrated the presence of MMP-2 is the dominate factor for selective killing tumor cell. Notably, CS-MDP and NS-MDP alone show comparable cell viability against all three cells (**Fig. 4.15B**) at ~70%-80%.

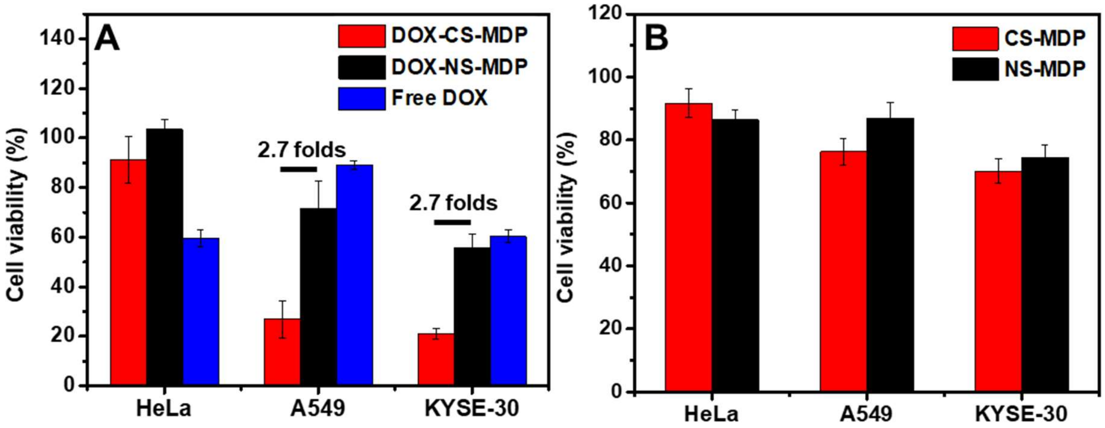

Figure 4.15 (A) Cell viability assay of HeLa cell, A549 cell and KYSE-30 cell upon incubation with free DOX, DOX conjugated CS-MDPs and NS-MDPs. (B) Cell viability assay of HeLa cell, A549 cell and KYSE-30 cell upon incubation with CS-MDPs and NS-MDPs. The assay was performed after 48 hs of incubation of cells with peptides with a total peptide concentration of 20 μM.

The cell-selective drug efficacy/toxicity is largely attributed to the enhanced membrane activity of CS-MDPs upon enzyme-mediated supramolecular assembly that can facilitate the transport and release of DOX to the cytoplasm as confirmed by flow cytometry showing much higher intracellular DOX fluorescence for cells treated with DOX-CS-MDP than those treated with DOX-NS-MDP (**Fig. 4.16**).

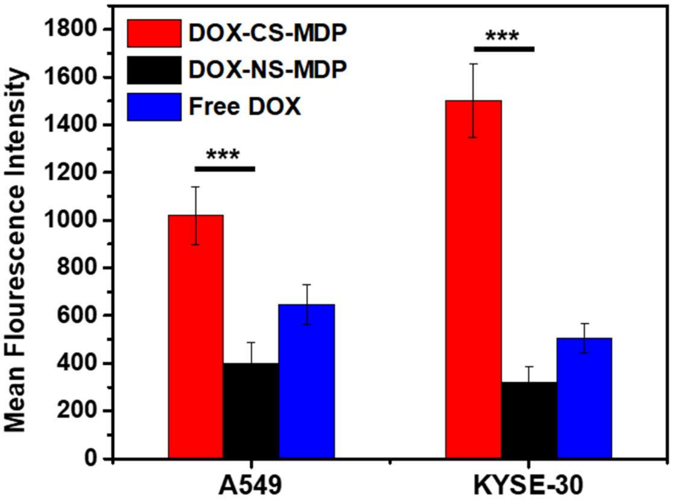

Figure 4.16 Flow cytometry of HeLa cell, A549 cell and KYSE-30 cell treated with DOX conjugated CS-MDP and NS-MDP. Incubation time: 24 hs. Final peptide concentration in the culture medium: 20 μM. Statistic significant difference is indicated by ***$p < 0.001$.

4.3 Conclusion

We demonstrated a modular design approach to the fabrication of supramolecular peptide assembly with enzymatic triggered cell-selective membrane activity. The approach is driven by our recent discovery that supramolecular ionic clusters on a β-sheet nanofiber scaffold can effectively perturb the cell membrane compared to their monomeric counterparts. In this work, cell selectivity is achieved through the rational design of MDPs that can undergo cell-selective enzyme-mediated molecular and supramolecular transformation from a monomeric peptide with low membrane activity to nanofibers with enhanced membrane activity. The targeted cargo delivery was also tested by module drug of DOX, and significant selectivity is clearly shown in the delivery. Because the design of MDP building blocks is highly modular, we can readily change the LL domain in the linear peptide sequence to respond to different disease-specific physiological conditions, such as reactive oxygen species and hypoxia for targeted molecular imaging and therapy for diseases not limited to cancer.

4.4 Experimental Section

Materials

4-Methylbenzhydrylamine (MBHA) rink amide resin, Fmoc-protected amino acids, 2-(1H-benzotriazol-1-yl)-1,1,3,3-tetramethyluronium hexafluorophosphate (HBTU), 5(6)-carboxylfluoresceinpiperidine, diisopropylethylamine (DIPEA), 6-(7-nitrobenzofurazan-4-ylamino) hexanoic acid (NBD-hexanoic acid), Active Human MMP-2 enzyme, and Congo red were purchased from Sigma-Aldrich. Trifluoroacetic acid (TFA), triisopropylsilane (TIS), acetonitrile (CH3CN), dimethylformamide (DMF), acetic anhydride, DOX hydrochloride, 3-Mercaptopropionic acid (MPA), 2,2-Dithiodipyridine (Py-SS-Py), Dulbecco's modified Eagle medium (DMEM), Gibco Roswell Park Memorial Institute (RPMI) 1640 Medium, Ham's F-12 Nutrient Mixture and glutathione (reduced) were purchased from Fisher Scientific and used as received. Hoechst 33342 were purchased from Life Technologies. Fetal Bovine Serum (FBS) was purchased from VWR. SensoLyte ® 520 MMP - 2 Assay Kit *Fluorimetric* was purchased from AnaSpec, Inc. CCK8 assay kit was obtained from Dojindo Molecular Technologies (Rockville, MD). Transmission Electron Microscopy (TEM) grids and uranium acetate dihydrate were purchased from Ted Pella, Inc.

Peptides Synthesis and Purification

The synthesis was performed on on a *Prelude*® peptide synthesizer at a 30 μmol scale using MBHA rink amide resin as the solid support. The synthetic procedure followed the standard Fmocs solid-phase peptide synthesis method. Generally, the Fmoc group was deprotected in the presence of 2 mL of 20% (V/V) piperidine/DMF for 5 minutes and repeated once. 1 mL of 120 mM Fmoc-protected amino acids in DMF was mixed with 0.3 mL of 400 mM HBTU and 0.3 mL of 800 mM of DIPEA in DMF. The mixture was added to the reaction vessel and the coupling reaction was carried out for 30 mins. After the completion of the synthesis, the N-terminus of the MDPs was acetylated using 50 μL of DIPEA and 330 μL of acetic anhydride in DMF (2 mL) for 1 h. Kaiser test was performed to confirm the completion of the acetylation reaction. The acetylated peptide was cleaved in a mixture of 2 mL of TFA/TIS/ H2O (95/2.5/2.5 by volume) for 3 hs. The cleavage solution was filtered, and the filtrates were collected. The resin was washed three times with neat TFA, and all filtrate solutions were combined and evaporated under airflow. The residual peptide solution was precipitated in cold diethyl ether, followed by centrifugation and washing with cold diethyl ether three times. The crude peptide was dried under vacuum overnight for HPLC purification. Peptides were purified using a preparative reverse phase C4 column with a linear gradient of H2O/CH3CN (5% to 95% of acetonitrile in 30 mins) containing 0.05% TFA and the elution was monitored at both 230 nm and 280 nm. The HPLC fraction was collected, combined and lyophilized for 2 days yielding while powders with an overall yield at ~ 40%. NBD labeled peptides were synthesized as follows. After the final deprotection of the Fmoc group, peptide resin (typically 15 μmol based on the loading number of the original amino groups on the MBHA resin) was treated with 4 equivalents (i.e. 60 μmol) of 6-(7-nitrobenzofurazan-4-ylamino) hexanoic acid (NBD-hexanoic acid), 4 equivalents of HBTU and 8 equivalents of DIPEA in 2 mL of DMF. The reaction mixture was stirred overnight.

The completion of the coupling reaction was confirmed by the Kaiser test. The cleavage and purification steps followed the same procedure as described above yielding yellow powders with an overall yield of ~ 20%. The molecular weight of each peptide was characterized and confirmed by ESI mass spectrometry.

Table 0.1 List of peptides used in the study.

Name	Peptide Sequence	Mass calculated [M+3H]+	Mass found [M+3H]+
CS-MDP	Acetyl-K10(QW)6E3G3PLGLAGK5	1645.3	1645.8
NS-MDP	Acetyl-K10(QW)6E3G3LALGPGK5	1645.3	1645.8
NBD-CS-MDP	NBD-K10(QW)6E3G3PLGLAGK5	1723.3	1723.9
NBD-NS-MDP	NBD-K10(QW)6E3G3LALGPGK5	1723.3	1723.8
DOX-CS-MDP	DOX-SS-CK10(QW)6E3G3PLGLAGK5	1890.0	1890.1
DOX-NS-MDP	DOX-SS-CK10(QW)6E3G3LALGPGK5	1890.0	1890.2
DOX-(NBD)CS-MDP	DOX-SS-C(NBD)K10(QW)6E3G3PLGLAGK5	1967.7	1968.3
DOX-(NBD)NS-MDP	DOX-SS-C(NBD)K10(QW)6E3G3LALGPGK5	1967.7	1968.2

Synthesis of 2-pyridyl-2-carboxyethyl disulfide (Py-SS-MPA)

Py-SS-MPA was synthesized and purified according to a literature method.[46] 0.2 mL of acetic acid was added to a 10 mL of ethanol solution of Py-SS-Py (1 mmol, 220 mg). 42 μL (0.5 mmol) of MPA was dissolved in 10 mL of ethanol and added dropwise through an addition funnel. The reaction mixture was stirred at room temperature for 2 hs. The solvent was evaporated with a rotary evaporator. The crude product was purified on a silica gel column using hexane/ethyle acetate (v/v = 3/2) as the eluent to afford the product. After removing the solvent with a rotary evaporator, a colorless viscous oil was produced with a yield at 45%. This product was characterized by 1H NMR (Jeol eca 500) (**Fig. S10**). 1H

NMR (500 MHz, DMSO-d6) δ 8.56 – 8.30 (m, 1H), 7.89 – 7.63 (m, 2H), 7.34 – 7.06 (m, 1H), 2.97 (t, J = 6.9 Hz, 2Hz), 2.61 (t, J = 6.8 Hz, 2Hz).

Synthesis of Py-SS-DOX

Py-SS-DOX was synthesized according to a literature method.[46] Py-SS-MPA (21.5 mg, 0.1 mmol) and HBTU (37.9 mg, 0.1 mmol) were dissolved in 5 mL of DMF and stirred for 30 mins to activate the carboxyl group on the Py-SS-MPA. DOX•HCl (87 mg, 0.15 mmol) was dissolved in 5 mL of DMF and was added dropwise to the reaction mixture. 0.2 mL of DIPEA was added to the reaction mixture. The reaction mixture was stirred at room temperature for 3 hs. The reaction mixture was precipitated in 300 mL of cold anhydrous diethyl ether. The crude product was purified on a silica gel column using DCM/methanol (30/1) as the eluents with an overall yield at ~20%. The product was characterized by 1H NMR and ESI/MS (Fig. S11). 1H NMR (500 MHz, DMSO-D6) δ 8.32 (d, J = 4.8 Hz, 1H), 7.81 – 7.75 (m, 2H), 7.71 – 7.58 (m, 3H), 7.52 (dt, J = 7.3, 2.0 Hz, 1H), 7.15 (s, 1H), 7.12 – 7.08 (m, 1H), 7.04 (s, 1H), 6.94 (s, 1H), 5.12 (d, J = 3.7 Hz, 1H), 4.82 (t, J = 4.5 Hz, 1H), 4.48 (s, 2H), 4.07 (q, J = 6.6 Hz, 1H), 3.87 (s, 4H), 3.30 (s, 22H), 2.92 – 2.76 (m, 4H), 2.38 (dhept, J = 14.9, 6.9 Hz, 4H), 2.15 – 1.96 (m, 2H), 1.74 (td, J = 13.0, 4.1 Hz, 1H), 1.33 (dd, J = 12.6, 4.5 Hz, 1H), 1.03 (d, J = 6.4 Hz, 3H). ESI/MS: expected 740.8, observed 741.3.

Synthesis of DOX-peptide Conjugates.

DOX-CS-MDP and DOX-NS-MDP were prepared through a thiol-disulfide reaction between Py-SS-DOX and a cysteine containing MDP, denoted as Cys-CS-MDP or Cys-NS-MDP. Experimentally, 7.0 mg (1.6 μmol) of Py-SS-DOX and ~ 1.0 mg (1.2 μmol) of Cys-

CS-MDP or Cys-NS-MDP were dissolved in 1 mL of DMF. The reaction was stirred at room temperature for 24 hs. The reaction mixture was directly injected on a semi-preparative reverse phase HPLC using a C4 column and a linear gradient of H2O/CH3CN (5% to 95% of CH3CN in 30 mins) containing 0.05% TFA. The HPLC elutions as monitored by UV at 230 nm and 280 nm were collected for lyophilization, which yielded red powder products with an overall yield at ~ 33%. The product was characterized and confirmed by ESI/MS. For the synthesis of DOX-(NBD)CS-MDP and DOX-(NBD)NS-MDP, NBD was first conjugated on the N-terminus of Cys-CS-MDP following the procedure described in the section of "Peptide Synthesis and Purification". DOX was attached using the same procedure through thiol-disulfide reaction to generate DOX-(NBD)CS-MDP and DOX-(NBD)NS-MDP. The reaction mixture was directly injected on a semi-preparative reverse phase HPLC using a C4 column and a linear gradient of H2O/CH3CN (5% to 95% of CH3CN in 30 mins) containing 0.05% TFA. The HPLC elutions as monitored by UV at 230 nm and 280 nm were collected for lyophilization, which yielded red powder products with an overall yield at ~ 15%.

Determination of the MMP-2 Cleavage Efficiency

Solutions of CS-MDP or NS-MDP were freshly prepared at a concentration of 100 μM in 1 mL of buffer (Tris 20 mM, CaCl2 5 mM, ZnCl2 20 mM, pH = 7.4). 6.5 μL of 0.1 μg/ μL active MMP-2 enzyme stock solution was added to the peptide solution to reach a final concentration of 10 nM. The reaction mixture was incubated at 37 °C for 4 hs and 24 hs and then injected onto the HPLC. The area of the elution peaks corresponding to the intact peptide and the fragment were integrated and used to calculate the cleavage efficiency.

Circular Dichroism (CD) Spectroscopy

The CD spectra were collected on a Jasco-J710 spectrometer. To prepare samples for CD measurements, stock solutions of CS-MDP or NS-MDP (~ 1 mM) were dilute to 100 μM in the following buffer (Tris 20 mM, CaCl2 5 mM, ZnCl2 20 mM, pH = 7.4). Active MMP-2 enzyme stock solution in the same buffer (0.1 μg/ μL) was added to the peptide solution to reach a final concentration at 10 nM. After incubation for 4 hs and 24 hs, peptides were further diluted to 20 μM in the same buffer (Tris 20 mM, CaCl2 5 mM, ZnCl2 20 mM, pH = 7.4) for CD spectra acquisition. CD spectra were collected from 250 nm to 190 nm at room temperature using a 2 mm cuvette, a bandwidth at 0.1 nm, scan rate at 100 nm/min and a response time of 2 sec. The final CD spectrum is the average of five consecutive scans. The mDeg of rotation was converted to the mean residual ellipticity using the following formula $\theta = \frac{1000 \times mDeg}{c * n * l}$, where c is the concentration of the peptide solution in mM, n is the number of amino acids in the peptide sequence and l is the path length of the cell used in mm.

Transmission Electron Microscopy (TEM)

TEM was performed on a Hitachi H-9500 High-resolution TEM instrument. For TEM sample preparation, stock solutions of CS-MDP or NS-MDP (~ 1 mM) were dilute to 100 μM in the following buffer (Tris 20 mM, CaCl2 5 mM, ZnCl2 20 mM, pH = 7.4). Active MMP-2 enzyme stock solution in the same buffer (0.1 μg/ μL) was added to the peptide solution to reach a final concentration at 10 nM. After incubation for 4 hs and 24 hs, 10 μL of the respective peptide solution was pipetted onto a holey carbon grid (TED PELLA 01824). After 2 mins, the excess solution was carefully removed with filter paper. 10 μL of 2 wt% uranyl acetate solution was dropped onto the grid for negative staining. The excess staining solution was removed with filter paper after 2 mins. The TEM sample was air-dried overnight before imaging.

Analytical Ultracentrifugation (AUC)

To prepare samples for AUC measurements, stock solutions of CS-MDP or NS-MDP (~ 1 mM) were dilute to 100 μM in the following buffer (Tris 20 mM, CaCl2 5 mM, ZnCl2 20 mM, pH = 7.4). Active MMP-2 enzyme stock solution in the same buffer (0.1 μg/ μL) was added to the peptide solution to reach a final concentration at 10 nM. After incubation for 4 hs and 24 hs, peptides were further diluted to 20 μM in the same buffer (Tris 20 mM, CaCl2 5 mM, ZnCl2 20 mM, pH = 7.4) prior to measurements. Sedimentation velocity experiments were performed on a Beckman-Coulter Optima XL-I analytical ultracentrifuge equipped with an An-50 Ti 8-hole rotor. Double-sector centerpieces sandwiched between sapphire windows in a standard cell housing were loaded with 400 μL of sample (in the sample sector) and an equal volume of reference buffer , i. e. Tris buffer (20 mM, pH = 7.4) containing 5 mM of CaCl2 and 20 mM of ZnCl2 (in the reference sector). After 2 hs of equilibration under vacuum at the experimental temperature (20 °C), samples were centrifuged at 50,000 rpm or 15,000 rpm. Data were acquired using UV absorbance optics tuned to 280 nm for each sample. Sedimentation velocity data was fitted to a continuous *c(s)* distribution model using SEDFIT. The buffer density and viscosity at room temperature were determined to be 0.99939 g/mL and 0.01009 cP, respectively using SEDNTERP. The partial-specific volume was estimated at 0.75613 mL/g. A resolution of 100 was utilized with a regularization level of 0.68. Time-invariant noise elements were removed from the data. All figures featuring *c(s)* distributions were generated in GUSSI.[47]

Cell Culture

HeLa cell was maintained in DMEM containing 10% FBS. A549 cell was maintained in RPMI1640 containing 10% FBS. KYSE-30 cell was maintained in a medium mixture of 45% RPMI1640, 45% Ham's F-12 and 10% FBS.

MMP-2 Activity Assay

SensoLyte ® 520 MMP - 2 Assay Kit *Fluorimetric* was standardized with an active MMP-2 enzyme. The active MMP-2 enzyme was prepared in 25 μL of analysis buffer with the following working concentration (0.2 nM, 0.4 nM, 0.8 nM, 1.6 nM and 3.0 nM) (three replicates for each concentration) in a 96 well-plate. 25 μL of MMP-2 substate was added to each well. The reaction mixture was incubated at 37 °C for 1 h followed by fluorescence measurement at ex/em = 490 nm / 520 nm. A standard curve for MMP-2 quantification was generated by plotting the fluorescence intensity against the MMP-2 working concentrations (**Fig. 4.9A**). To quantify the endogenous MMP-2 concentrations in different cell cultures, HeLa cell, A549 cell and KYSE-30 cell were seeded onto a 96-well plate at a density of 104 cells/well and incubated at 37 °C in an incubator with 5% of CO2. After 24 hs, HeLa cells were refreshed with DMEM medium, A549 and KYSE-30 cells were refreshed with RPMI1640 medium. After 24 hs of incubation at 37 °C in an incubator with 5% of CO2, the culture medium was removed for MMP-2 activity assay following the same procedure detailed above. Three replicates were performed for each cell line.

Cell Uptake

For the cell uptake study, cells were seeded onto a petri dish with a cover glass on the bottom at a density of 105 cells/well and incubated overnight at 37 °C in an incubator with 5% of CO_2. After 24 hs, HeLa cells were refreshed with 180 μL of DMEM medium, and A549 and KYSE-30 cells were refreshed with 180 μL of RPMI1640 medium. 20 μL of 200 μM NBD-CS-MDP or NBD-NS-MDP (in Tris buffer (20 mM, pH 7.4)) were added to the culture medium to reach a final concentration at 20 μM. For samples with the addition of exogenous MMP-2, 0.4 μL of 0.1 μg /μL active MMP-2 enzyme was added to the culture medium to reach a final concentration of 3 nM before adding the peptide. After 24 hs of incubation, the culture medium was removed and washed three times with PBS buffer. Cells were stained with nucleus staining dye, Hoechst 33342 at 37 °C for 15 min and washed with PBS buffer three times. Cells were imaged by an Ti2 inverted A1R HD25 confocal laser scanning microscope (Nikon, Japan) with a 40X objective (NA 1.3) and fluorescence images were processed using ImageJ.

Congo Red (CR) Staining Study

A549 cells were seeded in a petri dish with a cover glass bottom at a density of 105 cells/well and incubated at 37 °C for 24 hs. 20 μL of 200 μM NBD-CS-MDP or NBD-NS-MDP (in Tris buffer (20 mM, pH 7.4)) was mixed with 180 μL of fresh cell culture RPMI1640 medium. After incubation at 37 °C for 24 hs, the culture medium was removed and washed three times with PBS buffer. Cells were stained Hoechst 33342 at room temperature for 15 min and followed by washing three times with PBS buffer. 200 μL of 5 µM CR solution was added to cell culture for staining at 37 °C for 1 h. After removing CR solution and washing three times with PBS buffer, cells were imaged by an Ti2 inverted A1R HD25 confocal laser scanning microscope (Nikon, Japan) with a 40X objective (NA 1.3) and fluorescence images were processed using ImageJ.

Flow Cytometry

Cells were seeded onto a 24-well plate at a density of 105 cells/well and incubated for 24 hs at 37 °C with 5% of CO_2. HeLa cell was refreshed with 450 µL of DMEM medium while A549 and KYSE-30 were refreshed with 450 µL of RPMI1640 medium. 50 µL of NBD-CS-MDP or NBD-NS-MDP solutions (200 µM in Tris buffer (20 mM, pH 7.4)) were added. Three replicates was performed for each sample. After 24 hs, the culture medium was removed and cells were washed with PBS buffer for three times. Cells were digested with trypsin and washed twice with PBS buffer. 2% paraformaldehyde was used for cell fixation. The mean fluorescence intensity of cells upon different peptide treatments was quantified using the BD LSR II flow cytometer. A minimum of 10,000 events per sample was analyzed and data were processed using FlowJo software.

Cytotoxicity Measurement

Cells were seeded onto a 96-well plate at a density of 104 cells/well and incubated at 37 °C in an incubator with 5% of CO_2. After 24 hs, HeLa cell was refreshed with 90 µL of DMEM medium and A549 and KYSE-30 were refreshed with 90 µL of RPMI1640 medium. 10 µL of freshly prepared DOX, DOX-CS-MDP, DOX-NS-MDP (200 µM), CS-MDP or NS-MDP were added to each reach a final concentration at 20 µM. Cells incubated with 10 µL of

Tris buffer (20 mM, pH 7.4) were used as a control group. The culture medium was refreshed after 24 hs. After 48 hs of incubation, the culture medium was removed and the mixture of 90 μL fresh medium and 10 μL of CCK8 assay solution was added to each well.[48-49] After 1 h of incubation at 37 °C, UV absorbance was measured at 450 nm and the cell viability was calculated using the following equation. All experiments were performed in four replicates.

$$\% \text{ cell viability} = (A_{\text{peptide}} / A_{\text{Tris}} \text{ control}) \text{ x}100$$

Statistical Analysis

All data were expressed as means ± standard deviation (SD). The statistical analysis was performed using Student's T-test and one-way analysis of variance (ANOVA) at confidence levels of 95%.

4.5 References

1. Frankel, A. D.; Pabo, C. O., Cellular uptake of the tat protein from human immunodeficiency virus. *Cell* **1988,** *55* (6), 1189-1193.
2. Green, M.; Loewenstein, P. M., Autonomous functional domains of chemically synthesized human immunodeficiency virus tat trans-activator protein. *Cell* **1988,** *55* (6), 1179-1188.
3. Zorko, M.; Langel, U., Cell-penetrating peptides: mechanism and kinetics of cargo delivery. *Adv. Drug Deliv. Rev.* **2005,** *57* (4), 529-45.
4. McErlean, E. M.; Ziminska, M.; McCrudden, C. M.; McBride, J. W.; Loughran, S. P.; Cole, G.; Mulholland, E. J.; Kett, V.; Buckley, N. E.; Robson, T.; Dunne, N. J.; McCarthy, H. O., Rational design and characterisation of a linear cell penetrating peptide for non-viral gene delivery. *J. Control. Release* **2021,** *330*, 1288-1299.
5. Jiang, Y.; Han, M.; Bo, Y.; Feng, Y.; Li, W.; Wu, J. R.; Song, Z.; Zhao, Z.; Tan, Z.; Chen, Y.; Xue, T.; Fu, Z.; Kuo, S. H.; Lau, G. W.; Luijten, E.; Cheng, J., "Metaphilic" Cell-Penetrating Polypeptide-Vancomycin Conjugate Efficiently Eradicates Intracellular Bacteria via a Dual Mechanism. *ACS Cent. Sci.* **2020,** *6* (12), 2267-2276.
6. Lu, H.; Wang, J.; Bai, Y.; Lang, J. W.; Liu, S.; Lin, Y.; Cheng, J., Ionic polypeptides with unusual helical stability. *Nat. Commun.* **2011,** *2*, 206.
7. Rahman, M. A.; Jui, M. S.; Bam, M.; Cha, Y.; Luat, E.; Alabresm, A.; Nagarkatti, M.; Decho, A. W.; Tang, C., Facial Amphiphilicity-Induced Polymer Nanostructures for Antimicrobial Applications. *ACS Appl. Mater. Interfaces* **2020,** *12* (19), 21221-21230.
8. Rahman, M. A.; Bam, M.; Luat, E.; Jui, M. S.; Ganewatta, M. S.; Shokfai, T.; Nagarkatti, M.; Decho, A. W.; Tang, C., Macromolecular-clustered facial amphiphilic antimicrobials. *Nat. Commun.* **2018,** *9* (1), 5231.
9. Xu, D.; Dustin, D.; Jiang, L.; Samways, D. S.; Dong, H., Designed filamentous cell penetrating peptides: probing supramolecular structure-dependent membrane activity and transfection efficiency. *Chem. Commun.* **2015,** *51* (59), 11757-60.
10. Xu, D.; Jiang, L.; DeRidder, L.; Elmore, B.; Bukhari, M.; Wei, Q.; Samways, D. S. K.; Dong, H., Membrane activity of a supramolecular peptide-based chemotherapeutic enhancer. *Mol. Biosyst.* **2016,** *12* (9), 2695-2699.
11. Xu, D.; Samways, D. S. K.; Dong, H., Fabrication of self-assembling nanofibers with optimal cell uptake and therapeutic delivery efficacy. *Bioact. Mater.* **2017,** *2* (4), 260-268.
12. Yang, S.; Xu, D.; Dong, H., Design and fabrication of reduction-sensitive cell penetrating nanofibers for enhanced drug efficacy. *J. Mater. Chem. B* **2018,** *6* (44), 7179-7184.
13. Yang, S.; Dong, H., Modular design and self-assembly of multidomain peptides towards cytocompatible supramolecular cell penetrating nanofibers. *RSC Adv.* **2020,** *10* (49), 29469-29474.
14. Jiang, T.; Olson, E. S.; Nguyen, Q. T.; Roy, M.; Jennings, P. A.; Tsien, R. Y., Tumor imaging by means of proteolytic activation of cell-penetrating peptides. *Proc. Natl. Acad. Sci. U.S.A.* **2004,** *101* (51), 17867-17872.

15. Shi, J.; Schneider, J. P., De novo Design of Selective Membrane-Active Peptides by Enzymatic Control of Their Conformational Bias on the Cell Surface. *Angew Chem. Int. Ed. Engl.* **2019,** *58* (39), 13706-13710.
16. Kalafatovic, D.; Nobis, M.; Son, J.; Anderson, K. I.; Ulijn, R. V., MMP-9 triggered self-assembly of doxorubicin nanofiber depots halts tumor growth. *Biomaterials* **2016,** *98*, 192-202.
17. Wang, Y.; Zhan, J.; Chen, Y.; Ai, S.; Li, L.; Wang, L.; Shi, Y.; Zheng, J.; Yang, Z., Selective pericellular hydrogelation by the overexpression of an enzyme and a membrane receptor. *Nanoscale* **2019,** *11* (29), 13714-13719.
18. Ji, W.; Yuan, C.; Chakraborty, P.; Makam, P.; Bera, S.; Rencus-Lazar, S.; Li, J.; Yan, X.; Gazit, E., Coassembly-Induced Transformation of Dipeptide Amyloid-Like Structures into Stimuli-Responsive Supramolecular Materials. *ACS Nano* **2020,** *14* (6), 7181-7190.
19. Lin, Y. A.; Ou, Y. C.; Cheetham, A. G.; Cui, H., Rational design of MMP degradable peptide-based supramolecular filaments. *Biomacromolecules* **2014,** *15* (4), 1419-27.
20. Webber, M. J.; Newcomb, C. J.; Bitton, R.; Stupp, S. I., Switching of Self-Assembly in a Peptide Nanostructure with a Specific Enzyme. *Soft Matter.* **2011,** *7* (20), 9665-9672.
21. Lin, B. F.; Megley, K. A.; Viswanathan, N.; Krogstad, D. V.; Drews, L. B.; Kade, M. J.; Qian, Y.; Tirrell, M. V., pH-responsive branched peptide amphiphile hydrogel designed for applications in regenerative medicine with potential as injectable tissue scaffolds. *J. Mater. Chem.* **2012,** *22* (37).
22. Tanaka, A.; Fukuoka, Y.; Morimoto, Y.; Honjo, T.; Koda, D.; Goto, M.; Maruyama, T., Cancer cell death induced by the intracellular self-assembly of an enzyme-responsive supramolecular gelator. *J. Am. Chem. Soc.* **2015,** *137* (2), 770-5.
23. Wang, H.; Feng, Z.; Wang, Y.; Zhou, R.; Yang, Z.; Xu, B., Integrating Enzymatic Self-Assembly and Mitochondria Targeting for Selectively Killing Cancer Cells without Acquired Drug Resistance. *J. Am. Chem. Soc.* **2016,** *138* (49), 16046-16055.
24. Bellomo, E. G.; Wyrsta, M. D.; Pakstis, L.; Pochan, D. J.; Deming, T. J., Stimuli-responsive polypeptide vesicles by conformation-specific assembly. *Nat. Mater.* **2004,** *3* (4), 244-8.
25. Collier, J. H.; Hu, B. H.; Ruberti, J. W.; Zhang, J.; Shum, P.; Thompson, D. H.; Messersmith, P. B., Thermally and photochemically triggered self-assembly of peptide hydrogels. *J. Am. Chem. Soc.* **2001,** *123* (38), 9463-9464.
26. Bowerman, C. J.; Nilsson, B. L., A reductive trigger for peptide self-assembly and hydrogelation. *J. Am. Chem. Soc.* **2010,** *132* (28), 9526-9527.
27. Jiang, T.; Zhang, Z.; Zhang, Y.; Lv, H.; Zhou, J.; Li, C.; Hou, L.; Zhang, Q., Dual-functional liposomes based on pH-responsive cell-penetrating peptide and hyaluronic acid for tumor-targeted anticancer drug delivery. *Biomaterials* **2012,** *33* (36), 9246-58.
28. Li, J.; Liu, F.; Shao, Q.; Min, Y.; Costa, M.; Yeow, E. K.; Xing, B., Enzyme-responsive cell-penetrating peptide conjugated mesoporous silica quantum dot nanocarriers for controlled release of nucleus-targeted drug molecules and real-time intracellular fluorescence imaging of tumor cells. *Adv. Healthc. Mater.* **2014,** *3* (8), 1230-9.

29. Kessenbrock, K.; Plaks, V.; Werb, Z., Matrix metalloproteinases: regulators of the tumor microenvironment. *Cell* **2010,** *141* (1), 52-67.

30. Noel, A.; Jost, M.; Maquoi, E., Matrix metalloproteinases at cancer tumor-host interface. *Semin. Cell Dev. Biol.* **2008,** *19* (1), 52-60.

31. Sun, Z.; Li, R.; Sun, J.; Peng, Y.; Xiao, L.; Zhang, X.; Xu, Y.; Wang, M., Matrix Metalloproteinase Cleavable Nanoparticles for Tumor Microenvironment and Tumor Cell Dual-Targeting Drug Delivery. *ACS Appl. Mater. Interfaces* **2017,** *9* (46), 40614-40627.

32. Son, J.; Kalafatovic, D.; Kumar, M.; Yoo, B.; Cornejo, M. A.; Contel, M.; Ulijn, R. V., Customizing Morphology, Size, and Response Kinetics of Matrix Metalloproteinase-Responsive Nanostructures by Systematic Peptide Design. *ACS Nano* **2019,** *13* (2), 1555-1562.

33. Yang, Z.; Ma, M.; Xu, B., Using matrix metalloprotease-9 (MMP-9) to trigger supramolecular hydrogelation. *Soft Matter* **2009,** *5* (13), 2546-2548.

34. Kirschner, D. A.; Abraham, C.; Selkoe, D. J., X-ray diffraction from intraneuronal paired helical filaments and extraneuronal amyloid fibers in Alzheimer disease indicates cross-beta conformation. *Proc. Natl. Acad. Sci. U.S.A.* **1986,** *83* (2), 503-507.

35. Mohammadi, F.; Javid, H.; Afshari, A. R.; Mashkani, B.; Hashemy, S. I., Substance P accelerates the progression of human esophageal squamous cell carcinoma via MMP-2, MMP-9, VEGF-A, and VEGFR1 overexpression. *Mol. Biol. Rep.* **2020,** *47* (6), 4263-4272.

36. Wang, Y.; Lin, T.; Zhang, W.; Jiang, Y.; Jin, H.; He, H.; Yang, V. C.; Chen, Y.; Huang, Y., A Prodrug-type, MMP-2-targeting Nanoprobe for Tumor Detection and Imaging. *Theranostics* **2015,** *5* (8), 787-95.

37. Han, M.; Huang-Fu, M.-Y.; Guo, W.-W.; Guo, N.-N.; Chen, J.; Liu, H.-N.; Xie, Z.-Q.; Lin, M.-T.; Wei, Q.-C.; Gao, J.-Q., MMP-2-Sensitive HA End-Conjugated Poly(amidoamine) Dendrimers via Click Reaction To Enhance Drug Penetration into Solid Tumor. *ACS Appl. Mater. Interfaces* **2017,** *9* (49), 42459-42470.

38. Morgia, G.; Falsaperla, M.; Malaponte, G.; Madonia, M.; Indelicato, M.; Travali, S.; Mazzarino, M. C., Matrix metalloproteinases as diagnostic (MMP-13) and prognostic (MMP-2, MMP-9) markers of prostate cancer. *Urol. Res.* **2005,** *33* (1), 44-50.

39. Groblewska, M.; Mroczko, B.; Gryko, M.; Pryczynicz, A.; Guzinska-Ustymowicz, K.; Kedra, B.; Kemona, A.; Szmitkowski, M., Serum levels and tissue expression of matrix metalloproteinase 2 (MMP-2) and tissue inhibitor of metalloproteinases 2 (TIMP-2) in colorectal cancer patients. *Tumour Biol.* **2014,** *35* (4), 3793-802.

40. Isaacson, K. J.; Martin Jensen, M.; Subrahmanyam, N. B.; Ghandehari, H., Matrix-metalloproteinases as targets for controlled delivery in cancer: An analysis of upregulation and expression. *J. Control. Release* **2017,** *259*, 62-75.

41. Williams, R. J.; Smith, A. M.; Collins, R.; Hodson, N.; Das, A. K.; Ulijn, R. V., Enzyme-assisted self-assembly under thermodynamic control. *Nat. Nanotechnol.* **2009,** *4* (1), 19-24.

42. Espargaro, A.; Llabres, S.; Saupe, S. J.; Curutchet, C.; Luque, F. J.; Sabate, R., On the Binding of Congo Red to Amyloid Fibrils. *Angew Chem. Int. Ed. Engl.* **2020,** *59* (21), 8104-8107.

43. Khurana, R.; Uversky, V. N.; Nielsen, L.; Fink, A. L., Is Congo red an amyloid-specific dye? *J. Biol. Chem.* **2001,** *276* (25), 22715-21.
44. Chen, W.; Li, S.; Lang, J. C.; Chang, Y.; Pan, Z.; Kroll, P.; Sun, X.; Tang, L.; Dong, H., Combined Tumor Environment Triggered Self-Assembling Peptide Nanofibers and Inducible Multivalent Ligand Display for Cancer Cell Targeting with Enhanced Sensitivity and Specificity. *Small* **2020,** *16* (38), e2002780.
45. Guo, W. W.; Zhang, Z. T.; Wei, Q.; Zhou, Y.; Lin, M. T.; Chen, J. J.; Wang, T. T.; Guo, N. N.; Zhong, X. C.; Lu, Y. Y.; Yang, Q. Y.; Han, M.; Gao, J., Intracellular Restructured Reduced Glutathione-Responsive Peptide Nanofibers for Synergetic Tumor Chemotherapy. *Biomacromolecules* **2020,** *21* (2), 444-453.
46. Song, Q.; Chuan, X.; Chen, B.; He, B.; Zhang, H.; Dai, W.; Wang, X.; Zhang, Q., A smart tumor targeting peptide-drug conjugate, pHLIP-SS-DOX: synthesis and cellular uptake on MCF-7 and MCF-7/Adr cells. *Drug Deliv.* **2016,** *23* (5), 1734-46.
47. Brautigam, C. A., Calculations and Publication-Quality Illustrations for Analytical Ultracentrifugation Data. *Methods Enzymol* **2015,** *562*, 109-33.
48. Ishiyama, M.; Miyazono, Y.; Sasamoto, K.; Ohkura, Y.; Ueno, K., A highly water-soluble disulfonated tetrazolium salt as a chromogenic indicator for NADH as well as cell viability. *Talanta* **1997,** *44* (7), 1299-1305.
49. Tominaga, H.; Ishiyama, M.; Ohseto, F.; Sasamoto, K.; Hamamoto, T.; Suzuki, K.; Watanabe, M., A water-soluble tetrazolium salt useful for colorimetric cell viability assay. *Anal. Commun.* **1999,** *36* (2), 47-50.

Chapter 5. pH-Responsive Peptide Self-Assembly*

5.1 Introduction

There have been growing interests in the development of pH-responsive materials for a number of biomedical and biotechnological applications ranging from targeted cancer therapy to proton transport and energy transduction.[1-5] Among various strategies, non-covalent self-assembly offers a versatile and modular approach to generating dynamic pH-responsive nanoscale structures with increased structural complexity and tunability. A wide range of molecular building blocks including lipids, peptides and polymers have been designed which can change charge and/or hydrophilicity based on the pH of the environment in order to induce a physical or structural change of the self-assembled nanostructures.[6-10] Compared to lipid and polymeric materials, self-assembled peptides offer key advantages in terms of precise control over the molecular definition of monomeric subunits, supramolecular nanostructure and the localization of each functional group.[11-24] Amino acids with an ionizable side chain, such as lysine or glutamic acid have been commonly selected and placed in a hydrophilic domain of a synthetic peptide to control the pH-dependent self-assembly process.[6, 9, 25-34] Although there have been successful examples of pH-responsive peptide self-assembly, most systems require a custom-design approach through fine-balancing the number of acidic and basic residues in the solvent exposed region. Tuning the pH-responsiveness of peptides with water-exposed amino acids may not be trivial because the intrinsic pK_a of most

---

[*] This chapter is based on Su Yang et al. Self-assembling Peptides with Internal Ionizable Unnatural Amino Acids: A New and General Approach to pH-responsive Peptide Materials. *Chem.: Asian J.*, Submitted. Some sections were rearranged for continuity.

natural ionic amino acids are relatively far from the biologically relevant pH range and may not shift much in a hydrated environment. Furthermore, the pH-sensing ability could be easily affected by the ion-pair interactions of these external ionic residues with various ionic species present in the complex biological environment. Therefore, a simple, effective, and widely applicable approach is highly needed for the development of pH-responsive peptide self-assembly to probe various complex biological processes in which pH gradient plays an important role.

In contrast to self-assembled peptides, many natural proteins contain ionic amino acids in the interior. These internal residues experience different microenvironments from those in the solvent-exposed regions, leading to significant changes in pK_a values and charged states. It was reported that the lysine residues located in the interior of an engineered staphylococcal nuclease have reduced pK_a values as low as 5.3.[35] While some proteins can withstand the charged states and do not change their conformation upon ionization, many proteins undergo a local or global structural change and in some cases, unfold globally. The structural basis for which the ionization of an internal group is coupled to sub-global or global protein structural change could serve as a new structure-based approach for the rational design and synthesis of pH-responsive peptide materials. Compared to the traditional method in which solvent-exposed residues are used to tune pH-responsiveness, the new approach based on internal ionizable amino acids has unique advantages in terms of the control over pK_a tunability and reduced interference from various ionic species existing in the biological environment. It is noted that for the first time this has been conceptualized for peptide self-assembly, but there are precedents with polymer systems in which ionizable monomers triggered self-assembled micelles.[36]

While natural basic amino acids such as lysine or arginine could be stabilized in a protein interior through intricate molecular interaction networks, peptide self-assembly has a confined hydrophobic core which makes it an unfavorable process to accommodate the extended aliphatic primary amine on lysines and guanidinium moiety on arginines. Therefore, there is a need for a new design and synthesis of unnatural amino acids that can present chemically diverse ionizable side chains for the construction of pH-responsive materials with enhanced pH tunability. In this work, we report the synthesis of two unnatural amino acids with a tertiary amine group, i.e. dialkylamino methyl on the side chain. Compared to lysine and arginine, these unnatural amino acids are more hydrophobic and therefore could be better accommodated in a hydrophobic compartment of a self-assembled peptide. As a proof-of-concept demonstration, we introduced these residues in a multidomain peptide (MDP). This peptide is known to self-assemble into a sandwich-like β-sheet nanofiber in which the hydrophobic residues are buried within the sandwich structure and shielded from the aqueous environment.[37-41] By replacing some of the hydrophobic residues on MDPs with these ionizable amino acids, nanofibers with an ionizable hydrophobic core can be generated to undergo pH-induced self-assembly or disassembly. While the pK_a of a free tertiary amine is typically found in the basic region, we anticipate the local hydrophobic environment can shift the pK_a of these tertiary-amine containing residues toward the biologically relevant pH at a near neutral or weakly acidic range, which is critical for practical applications such as tumor-acidity targeted drug delivery or proton transport. Although the proof-of-concept experiments are conducted through MDP design and self-assembly, the ionizable amino acids developed here can be readily incorporated in any other amphiphilic peptide to form functional peptide self-assembly but with built-in pH-responsiveness for applications ranging from disease targeted therapy to proton transport.

5.2 Results and Discussion

5.2.1 Peptide Design

While natural basic amino acids such as lysine or arginine could be stabilized in a protein interior through intricate molecular interaction networks. Peptide self-assembly has a confined hydrophobic β-sheet core which makes it an unfavorable process to accommodate the extended helix preferred aliphatic primary amine on lysines and guanidinium moiety on arginines. Therefore, there is a need for a new design of unnatural amino acids that can present chemically diverse ionizable side chains and also fit into the hydrophobic core to establish enhanced pH tunability. In this work, we report the synthesis of two unnatural amino acids with a tertiary amine group, i.e. dialkylamino methyl on the side chain. This design is inspired by β-sheet preferred leucine structure. Compared to lysine and arginine, these unnatural amino acids are more hydrophobic due to the carbon chains and therefore could be better accommodated in a hydrophobic compartment of a self-assembled peptide while it is deprotonated. As a proof-of-concept demonstration, we introduced these residues in a multidomain peptide (MDP). This peptide is known to self-assemble into a sandwich-like β-sheet nanofiber in which the hydrophobic residues are buried within the sandwich structure and shielded from the aqueous environment.[37-41] By replacing some of the hydrophobic residues on MDPs with these unnatural amino acids, nanofibers are able to undergo pH-induced self-assembly or disassembly. As widely known, the pK_a of a free tertiary amine is typically at 10, we anticipate the local hydrophobic environment can shift the pK_a of these tertiary-amine containing residues toward the acidic range. Ideally, the pKa of the self-assembly could be a shift to the biologically relevant pH at a near neutral or weakly acidic range, which is critical for practical applications such as acidity related disease targeted drug delivery or proton transport. Although the proof-of-concept experiments are conducted through MDP design and self-assembly, the ionizable amino acids developed here can be readily incorporated in any other amphiphilic peptide to form functional peptide self-assembly but with built-in pH-responsiveness for applications ranging from disease targeted therapy to proton transport.

The primary sequences of the MDPs used in this study are shown in **Table 5.1**. These sequences are generated based on our previous study of MDP which contains six repeating units of an alternating hydrophilic-hydrophobic residue, namely $(QW)(QL)_5$ (Q: glutamine, L: leucine, W: tryptophan; 5 refers to the number of repeating units of QL). Tryptophan was included as a UV-Vis probe for accurate concentration determination. As shown in our previous work, the polar-nonpolar repeating units of leucines and glutamines drive the formation of sandwich-like nanofibers in which leucines are embedded in the hydrophobic pocket of the assembly.[13] To enable pH-responsiveness of MDPs, as shown in **Table 5.1**, we replaced two of the leucine residues with a synthetic unnatural amino acid, denoted as X which contains a dialkylamino methyl group on the side chain. In this study we synthesized two variants of X containing two different alkyl groups on the tertiary amine side chain, *i. e.* dibutylamino methyl denoted as X_b and dipropylamino methyl denoted as X_p. The MDPs with X_b and X_p are terminated with polyethylene glycol (PEG of MW at 750 Da) to increase their solubility in the aqueous solution without changing the ionization status, and they are termed PEG-X_b and PEG-X_p. It is worth noting that PEGylated MDPs with mono-substitution of X_b or X_p led to insoluble materials across the entire pH range from 1 to 13, therefore continuing efforts for study on the mono-substituted peptides were not pursued. A control peptide was synthesized by replacing the same leucine residues with lysines, termed PEG-K. MDP terminated with consecutive lysine residues, denoted as K_4G_5-X_b was also synthesized to accommodate the need for specific physical characterization and biological activity evaluation. The non-substituted MDP is referred to as K_4G_5-L.

Table 0.1 Primary MDP sequences used in the study

Name	N-	Sequences	C-
PEG-X_b	PEG	(QW)(QL)(Q**X_b**)(QL)(Q**X_b**)(QL)	$CONH_2$
PEG-X_p	PEG	(QW)(QL)(Q**X_p**)(QL)(Q**X_p**)(QL)	$CONH_2$
PEG-K	PEG	(QW)(QL)(Q**K**)(QL)(Q**K**)(QL)	$CONH_2$
K_4G_5-X_b	CH_3CO	KKKKGGGGG(QW)(QL)(Q**X_b**)(QL)(Q**X_b**)(QL)	$CONH_2$
K_4G_5-L	CH_3CO	KKKKGGGGG(QW)(QL)(QL)(QL)(QL)(QL)	$CONH_2$

The highlighted residues represent the mutations made from leucine residues to different ionizable amino acids.

The synthesis of fluorenylmethyloxycarbonyl (Fmoc) protected X_b and X_p involves a reductive amination reaction of (S)-3-amino-2-(tert-butoxycarbonylamino) propanoic acid with butyraldehyde or propionaldehyde, followed by Boc deprotection and Fmoc protection of the amino group, the product is confirmed with NMR (**Fig. 5.1**).

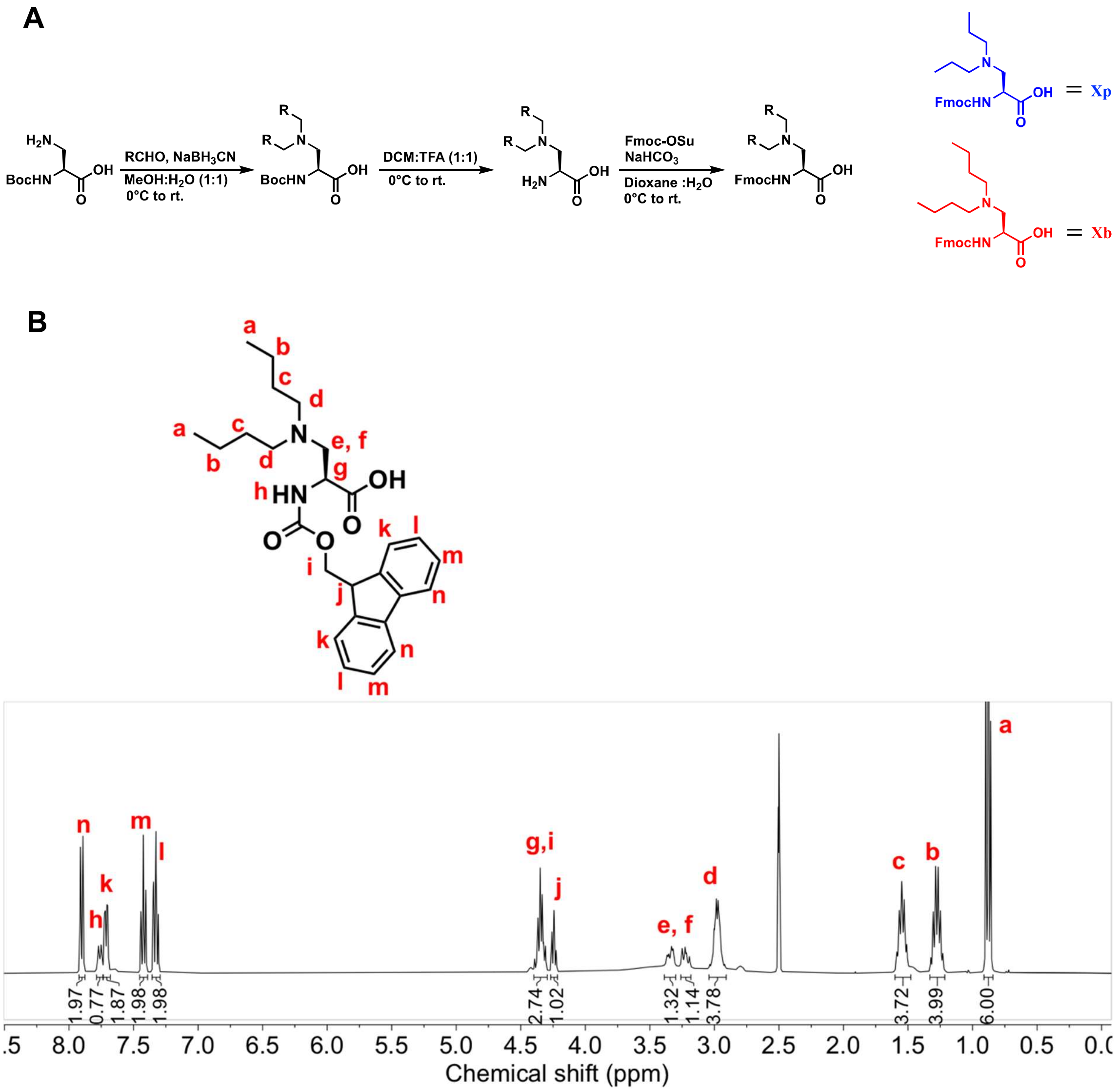

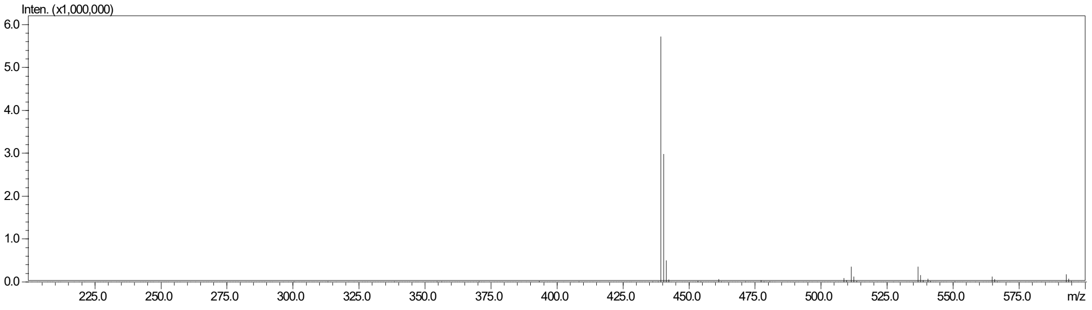

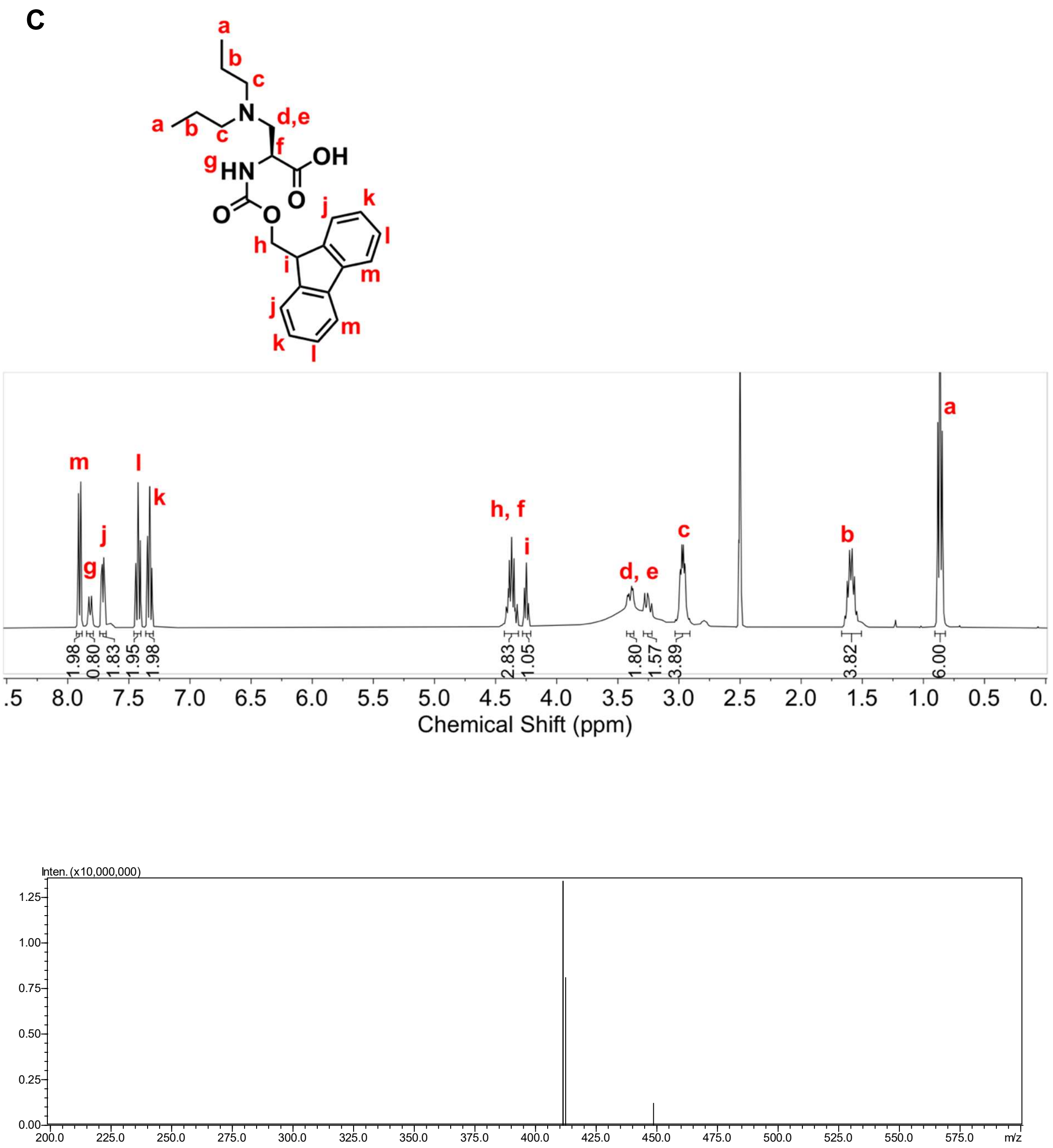

Figure 5.1 (A) Synthetic routes for Fmoc-X_b and Fmoc-X_p. (B) NMR and ESI spectra of Fmoc-X_b. (C) NMR and ESI spectra of Fmoc-X_p.

The Fmoc protected amino acids can be readily incorporated at specific sites of MDPs through solid-phase peptide synthesis. **Fig. 5.2A** shows the primary structure of the MDP with X_b, namely PEG-X_b and its ionization-dependent self-assembly process. The hypothesis is that upon self-assembly, the hydrophobic pocket can stabilize the neutral status of X_b and shift the equilibrium of the ionization process of peptide nanofiber. The design resulted in a significant reduction of the pK_a of the tertiary amine group on X_b to a near neutral or weakly acidic range. In contrast, the pK_a of a free X_b or X_b on an unassembled peptide is typically found in the basic pH range (**Fig. 5.2B**). The pK_a of the ionizable amino acids and therefore the ionization-dependent self-assembly process can be readily tuned by adjusting the hydrophobicity of the ionizable amino acids and the repeating unit of the self-assembly domain. While the current work is aimed to validate the hypothesis using PEG-X_b and PEG-X_p, future study is targeted at systematic synthesis and characterization of an expanded library of MDPs containing various X_b and X_p analogs.

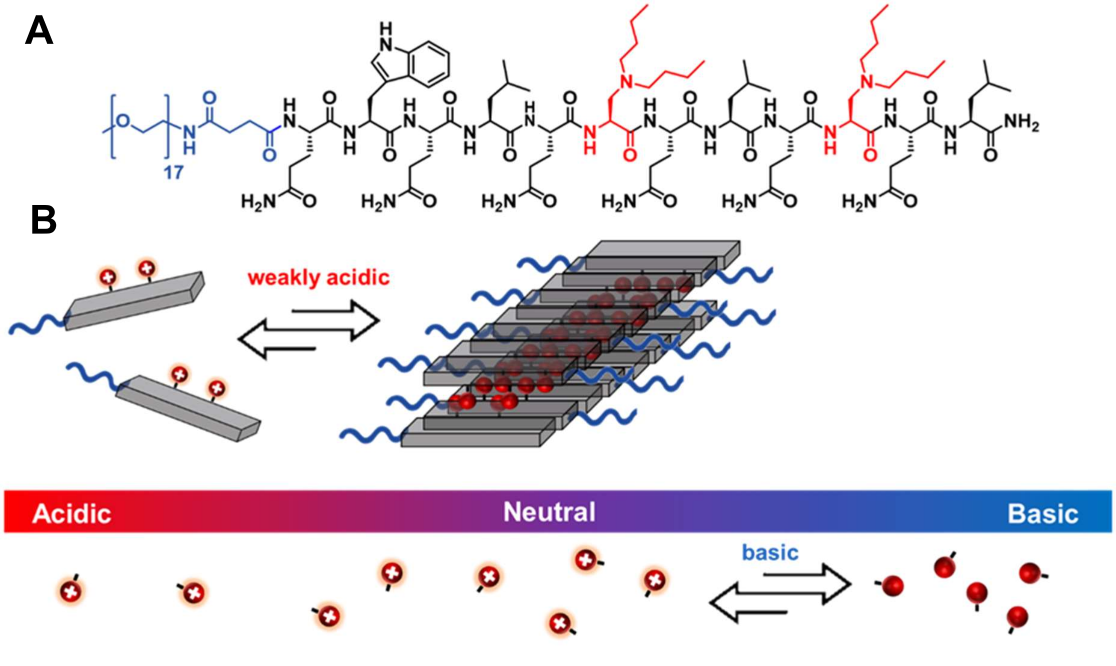

Figure 5.2 (A) Chemical structure of PEG-X_b with alternating hydrophilic (Q) and hydrophobic residue (W, L, or X_b) repeating units. (B) Schematic representation of self-assembly of PEG-X_b into a sandwich-like supramolecular nanofiber with X_b embedded in the hydrophobic pocket between the two sheets. The hydrophobic microenvironment shifts the pK_a of X_b to a weakly acidic range compared to that of unassembled peptide, which in turn facilitates self-assembly/disassembly to occur at a biologically relevant pH.

5.2.2 Determination of pKa

All peptides were synthesized in the solid-phase and purified by HPLC and characterized by mass spectrometry (**Fig. B-S1A-H**). pH titration was first conducted to determine the pK_a of PEG-X_b and PEG-X_p. The peptide solution is prepared in HCl solution to achieve monomeric status. As the base was added to the peptide solution, the generated cloudiness indicating self-assembly occurs as the positive charges on the tertiary amine groups are neutralized. As shown in **Fig. 5.3A**, both peptides exhibit a buffering capacity in the weakly acidic range between pH 5 and 6, which is much lower than that of an isolated tertiary amine group typically found above pH 9. Incomparison, PEG-K with lysine substituting leucine did not establish self-assembly and no apparent pK_a was identified upon titration up to pH 8, which indicated the lysine can't be imbedded into the hydrophobic core as expected. Fitting of the acid-base titration curves to a Hill plot yields a pK_a of 5.05 for PEG-X_b and pK_a of 5.54 for PEG-X_p (**Fig. 5.3B**). Importantly, the pK_a of PEG-X_b is shifted further to the acidic range compared to that of PEG-X_p, consistent with the higher hydrophobicity of the dibutylamino methyl group and therefore offering a pK_a tunability of the synthesized moiety for further exploration. The Hill plots also suggest positive cooperativity of the deprotonation process for both peptides. The Hill coefficient is 3.4 for PEG-X_b and 2.4 for PEG-X_p. The positive cooperativity reflects a close coupling process between deprotonation and self-assembly. Deprotonation triggers self-assembly to form nanofibers with a hydrophobic pocket, which in turn facilitates and accelerates the deprotonation process. The result suggested that X_b has a higher preference for self-assembly compared to X_p, X_b has more potential for further study.

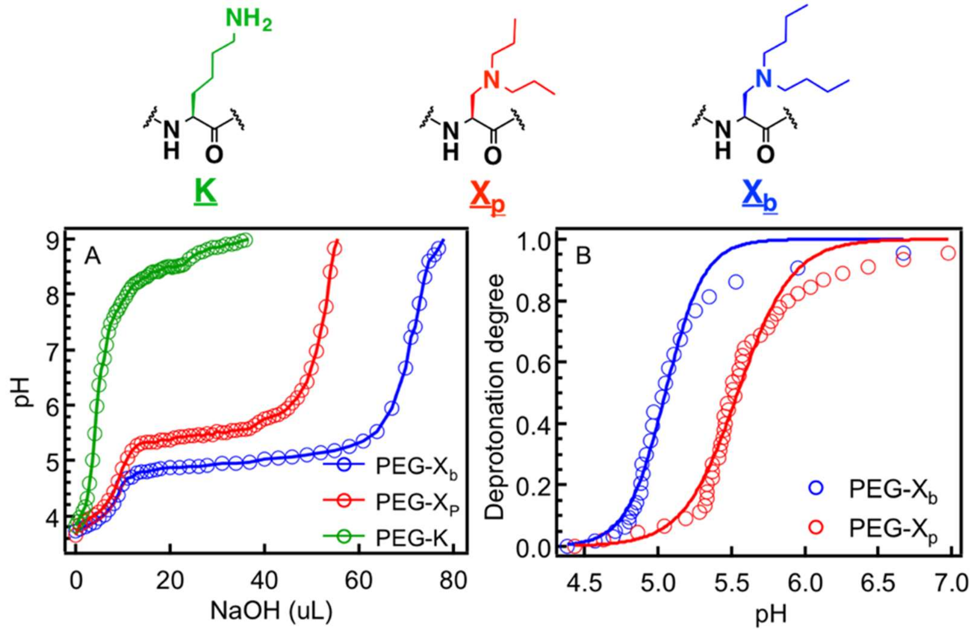

Figure 5.3 (A) Acid-base titration curves of MDPs containing different ionizable amino acids. (B) Hill plots of the acid-base titration of PEG-X_b and PEG-X_p yield a pK_a of 5.05 for PEG-X_b and a pK_a of 5.54 for PEG-X_p. The Hill coefficients were determined to be 3.4 for PEG-X_b and 2.4 for PEG-X_p, suggesting positive cooperativity of the deprotonation process to drive self-assembly. Circles: experimental data extracted from the titration curve. Solid lines: Hill plot fitting using the fitting equation $\theta = {}^{1}\!/_{1\,+\,10^{n\times(m-pH)}}$ in which θ is the deprotonation degree, n is the Hill coefficient and m is the pK_a.

There are two levels of structural change on X_p or X_b and both factors could lead to a pK_a shift. First of all, on the molecular level, the incorporation of X_p or X_b as a peptide can potentially increase their rigidity and therefore change their ionization capability. Secondly, on the supramolecular structural level, X_p or X_b is embedded in a total hydrophobic microenvironment upon MDP self-assembly. Similar to these natural proteins with internal ionizable amino acids, the local hydrophobic environment could drastically change the equilibrium of the protonation process and further cause a significant reduction of their pK_a. To decouple the two structural effects, we synthesized another peptide with the sequence of PEG-X_bGSSX_bGS (G: glycine, S: serine). The peptide is not capable of self-assembling into supramolecular nanofibers, which is confirmed by transmission electron microscopy (TEM) (**Fig. 5.4**).

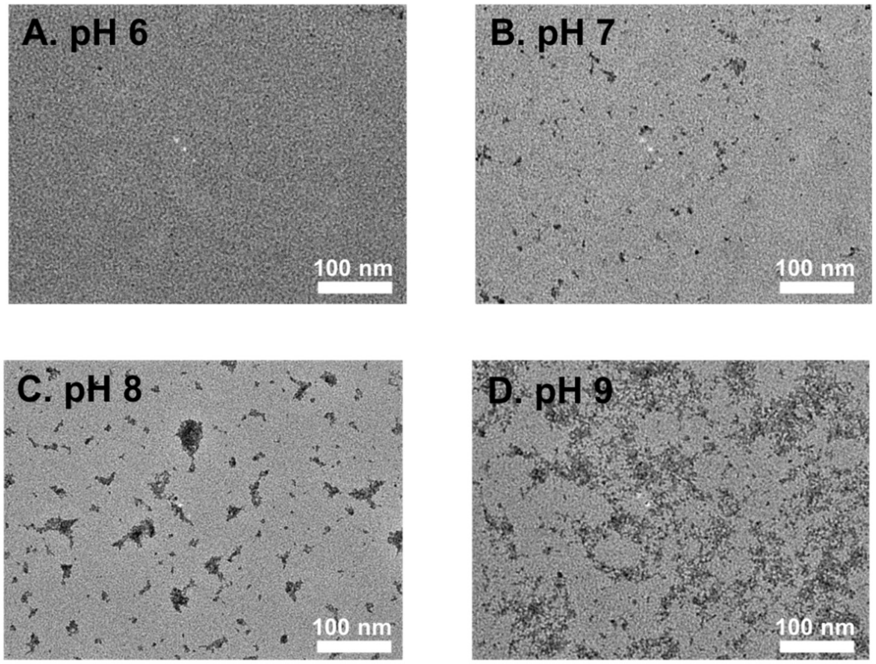

Figure 5.4 TEM of PEG-X_bGSSX_bGS at different pHs showing irregular aggregates.

As shown in **Fig. 5.5**, the peptide displays a broad pH transition range during the titration experiment, and there is no clear buffering capacity range that can identify up to a pH of 9. The results suggest that the shift of the pK_a to the weakly acidic range is majorly caused by the change of self-assemble structures, rather than the molecular conformational constraint in peptides. Collectively, these results provide important evidence that the unnatural ionizable residues didn't affect the self-assembly efficiency based on their reduced pK_a to a more biologically relevant pH range. For the following structural studies, we will primarily focus on peptides with X_b substitution which shows stronger positive cooperativity in the deprotonation-driven self-assembly process.

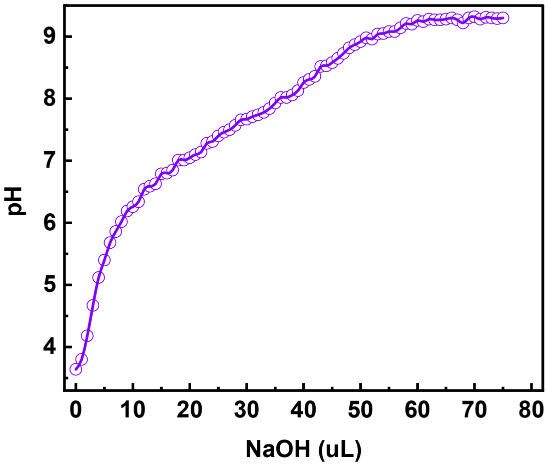

Figure 5.5 pH titration curve of PEG-X_bGSSX_bGS (1 mM, 300 μL) in DI water titrated against 0.01 M NaOH solution.

5.2.3 Structural Characterization of pH-dependent Self-assembly

It is hypothesized that X_b is compatible with the existing MDP design rule and therefore can be accommodated into the hydrophobic compartment of the supramolecular nanofiber. Here, we attempted to validate the supramolecular structure and packing of the designed MDP with a combined computational and experimental investigation. As the first step, the pH-dependent self-assembly/disassembly process was examined using several biophysical characterization methods. Circular dichroism (CD) spectroscopy was used to monitor the secondary structure of PEG-X_b at different pHs. As shown in **Fig. 5.6A**, above its pK_a of 5.05, PEG-X_b forms a well-defined β-sheet as characterized by a single minimum peak at 215 nm (solid lines). As the solution acidifies (i.e., pH ≤ 5.0), protonation of X_b triggers nanofiber disassembly and simultaneously a secondary structural transition from β-sheets to disordered random coils which have a minimum peak at 205 nm (dotted lines).

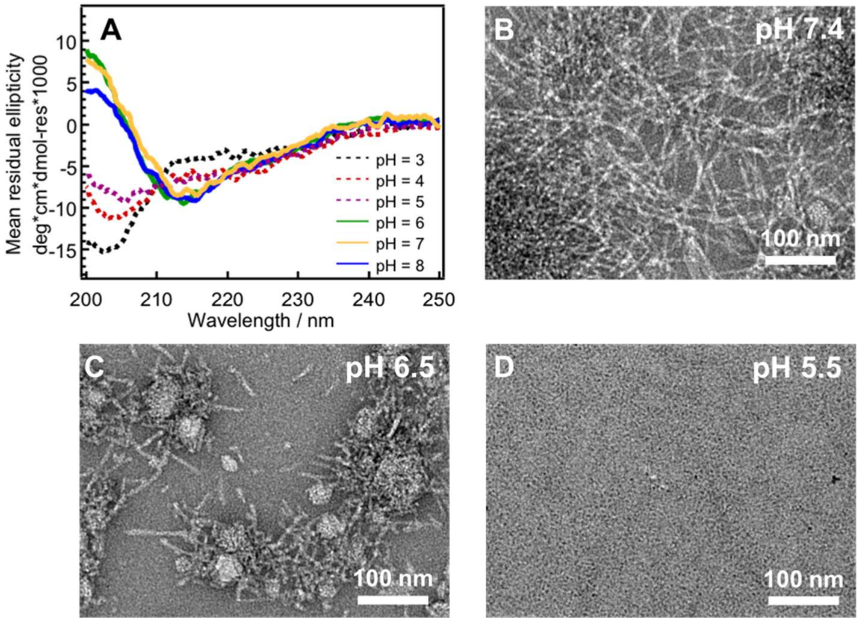

Figure 5.6 (A) CD spectra of PEG-X_b at different pHs showing a pH-dependent secondary structural transition from well-defined β-sheets (solid lines) to random coils (dotted lines) as the solution acidifies. TEM of PEG-X_b at (B) pH 7.5 shows a high density of fibers, (C) pH 6.5 showing a mixture of short fibers and spherical aggregates, and (D) pH 5.5 upon disassembly. Peptide solutions were prepared at 50 μM in BR buffer and PB buffer for CD measurements and 100 μM for TEM experiments.

Plotting the ellipticity at 205 nm (a characteristic wavelength used to monitor the structural transition of amyloid mimetic peptides[42]) as a function of the solution pH, we estimated the transition pH of PEG-X_b at ~ 5.5 (**Fig. 5.7**). It is interesting to see the mismatch between the pK_a (5.05) calculated by the acid-base titration experiment and the transition pH (5.5) determined by pH-dependent CD spectroscopy. This result suggests the hydrophobic core of the assembly is able the hold protonated X_b up to 24%. TEM imaging further confirmed the pH-dependent self-assembly as evidenced by the formation of the elongated nanofibers at pH 7.4 (**Fig. 5.6B**). As the pH decreases to 6.5, although CD shows a predominant β-sheet secondary structure, PEG-X_b started to disassemble into a mixture of short fibers and spherical aggregates (**Fig. 5.6C**). Further reduction of pH to 5.5 caused disassembly of the majority of peptides and nanostructures were rarely identified on the TEM grid (**Fig. 5.6D**). In particular, the nanofibers formed at pH 7.4 tend to form a network that has rarely been observed for regular MDPs with leucine residues in the hydrophobic core. The network may be triggered by the hydrogen bond between the X_b. The formation of elongated fibers at pH 7.4 convinced that X_b is fully compatible with the MDP design principle toward higher-ordered supramolecular nanofibers but with emerging pH-responsive properties.

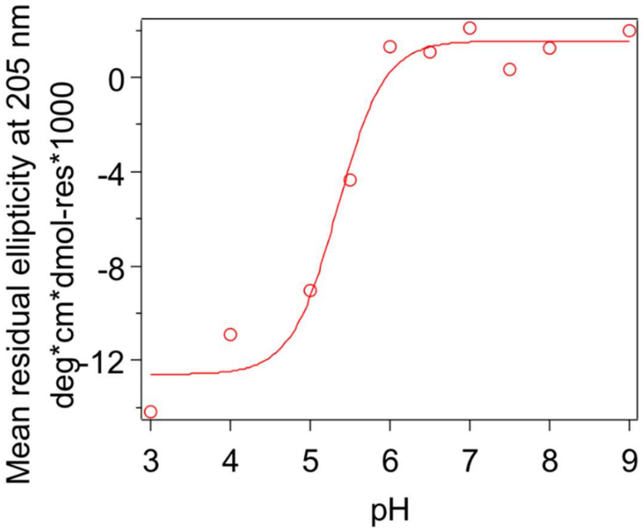

Figure 5.7 The plot of CD ellipticity at 205 nm as a function of solution pH to determine the secondary structural transition pH for PEG-X_b.

We conducted a preliminary solution-state NMR experiment to confirm the pH-dependent self-assembly process. For the NMR studies, peptides were acetylated at the N-terminus to avoid potential peak overlaps between the protons on the peptide and on the PEG moiety. Lyophilized peptide powders were first dissolved in pure D_2O with an initial pH of ~ 3.5 - 4.0 and NaOD was added to adjust the pH. Both 1D ^{1}H-NMR and 2D COSY NMR experiments were performed. Based on the chemical shift on the 1D spectrum and the correlation peaks on the 2D spectrum, all the protons on the backbone and side chains were identified, and complete assignments of the NMR peaks to each proton are shown in **Fig. 5.9** in particular, the diastereotopic methylene protons on the two X_b residues appear at 3.53 - 3.55 ppm and 3.24 - 3.28 ppm based on their correlation with the α protons at 4.66 ppm and 4.74 ppm (**Fig. 5.8 and Fig. 5.9**). The addition of NaOD triggered self-assembly leading to suppression of the NMR signals for all protons including the diastereotopic methylene group on the X_b residues.

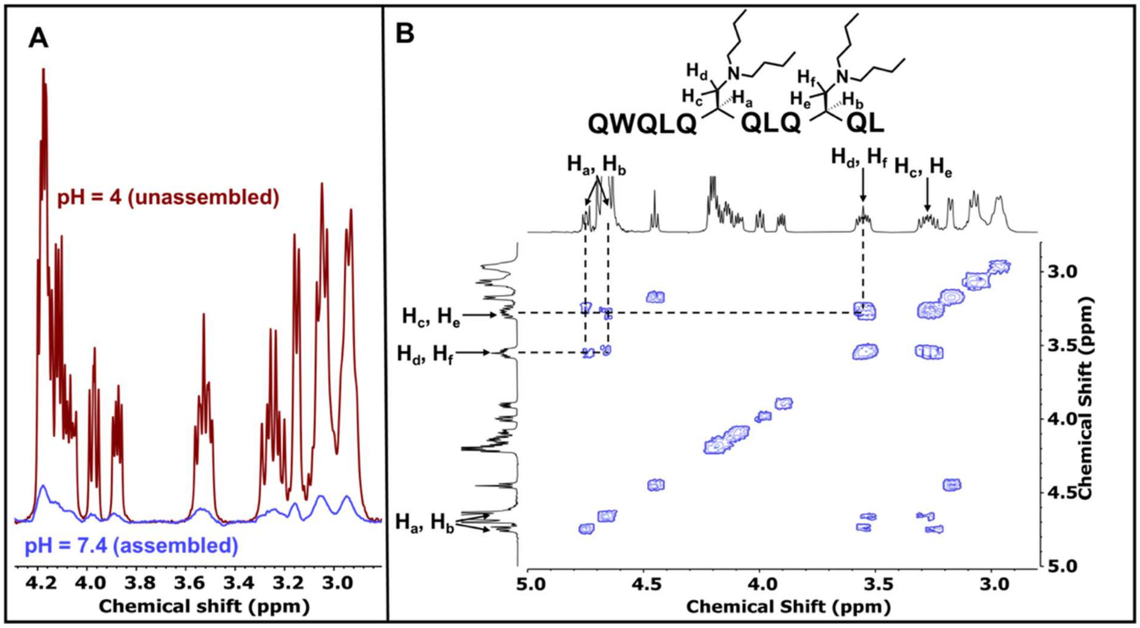

Figure 5.8 (A) 1D ^{1}H-NMR spectra of unassembled and assembled peptides at a pH below and above its pK_a. (B) 2D COSY NMR spectrum showing the correlation of the α hydrogens on the X_b residues with their respective diastereotopic β hydrogens. The full range spectrum and complete peak assignments are shown in Figure S6.

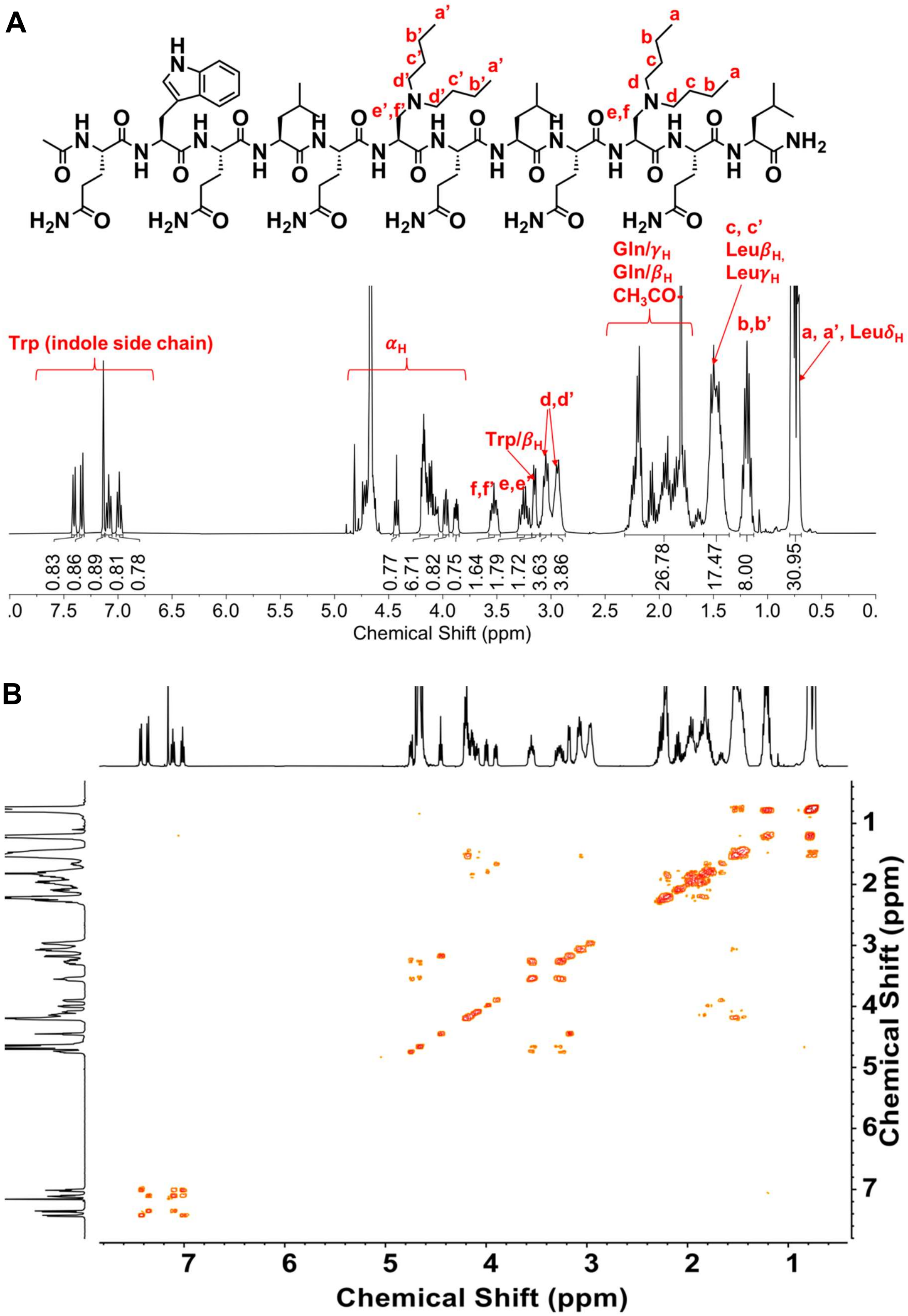

Figure 5.9 (A) 1D ^{1}H-NMR and (B) 2D COSY NMR spectra of unassembled peptides (CH_3CONH-QWQLQX$_b$QLQX$_b$QL) in D_2O.

To gain more quantitative insights into the pH-driven self-assembly and disassembly process in the solution state, we performed analytical ultracentrifugation – sedimentation velocity (AUC-SV) experiments to quantitatively determine the apparent molecular weights of the species formed at different pHs. To accommodate the technical conditions of the AUC experiment which typically runs at a high centrifugation speed for an extended time, we replaced the PEG moiety with consecutive lysine residues to further enhance their solubility. No visible precipitates were observed upon 1 h centrifugation (50,000 rpm) for K_4G_5-X_b while solutions of PEG-X_b show white precipitation generated at the same time under the same testing condition. We attempted to run AUC at three different pHs, however, K_4G_5-X_b prepared at pH 7.5 and 6.5 underwent fast sedimentation even at the lowest centrifugation speed of 3,000 rpm suggesting an enormously large species formed under those conditions (data not shown). In comparison, fitting of the AUC trace at pH 5.5 yielded a good quality distribution of sedimentation coefficients, and average molecular weight at 2.8 kDa was estimated for K_4G_5-X_b under this condition (**Fig. 5.10A and 5.10C**). The fitted-out observed molecular weight is consistent with the peptide monomer molecular weight. The result suggests protonation of X_b drives nanofiber disassembly to form predominantly monomers.

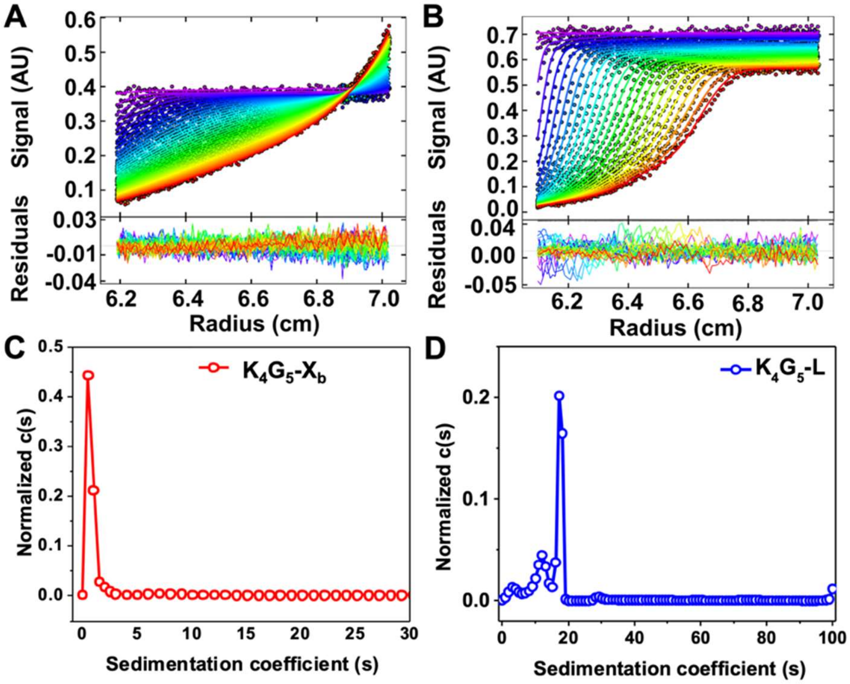

Figure 5.10 (A) Raw sedimentation profiles of absorbance at 230 nm versus cell radius and residual plot supplied by SEDFIT software for K_4G_5-X_b. (B) Raw sedimentation profiles of absorbance at 230 nm versus cell radius and residual plot supplied by SEDFIT software for K_4G_5-L. Continuous sedimentation coefficient distribution, c(s) curve of (C) K_4G_5-X_b showing predominant monomers (MW = 2.8 kDa) as a result of acidity-triggered disassembly at pH 5.5 and (D) K_4G_5-L showing predominantly a large assembly with a molecular weight at 3.4 MDa. Peptide solutions were prepared in PB buffer with a final concentration of 20 μM.

To further confirm the self-assembly status of the new involved peptide is also characterized by TEM and CD. TEM of K_4G_5-X_b showed the same trend of pH-dependent supramolecular assembly and disassembly (**Fig. 5.11**). CD spectroscopy further supported a pH-dependent secondary structural transition from β-sheets to random coils as pH decreases to 5.5 (**Fig. 5.12**).

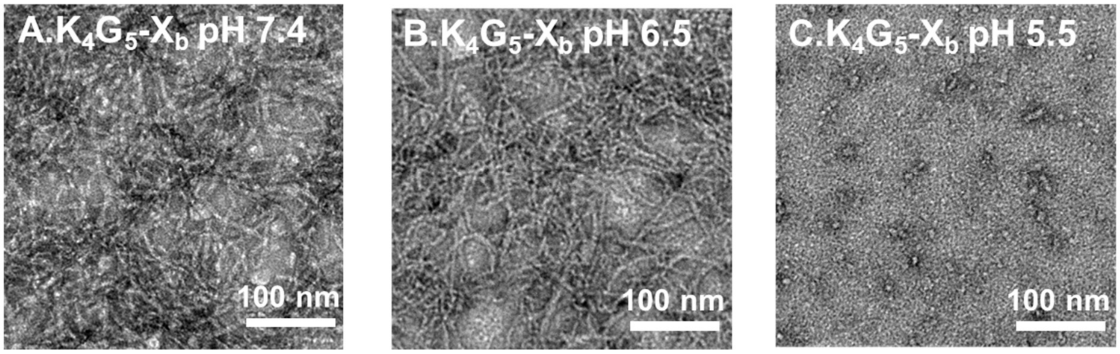

Figure 5.11 TEM of K_4G_5-X_b at (A) pH of 7.4, (B) pH of 6.5 and (C) pH of 5.5. The peptide was dissolved in 10 mM PB buffer at a concentration of 100 μM.

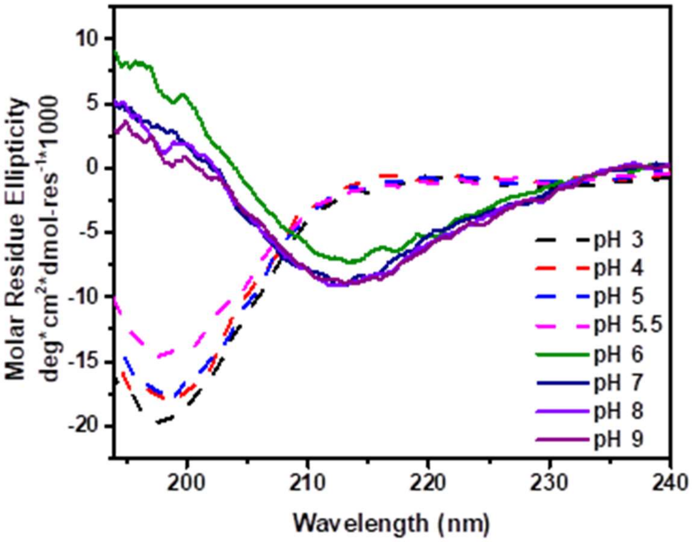

Figure 5.12 CD spectra of K_4G_5-X_b at different pHs in Britton–Robinson buffer with a final concentration at 50 μM.

To further confirm it is the internal ionizable X_b, rather than the external lysine residues, that drive peptide disassembly upon different solution acidifies, we synthesized another control peptide, denoted as K_4G_5-L (the sequence is shown in **Table 5.1**) with leucine and tryptophan occupying the hydrophobic domain. Fitting the sedimentation traces shows predominantly large assemblies at pH 5.5 for K_4G_5-L that do not have internal ionic amino acids (**Fig. 5.8B and 5.8D**). CD spectroscopy shows a predominant β-sheet secondary structure under all pH conditions tested (**Fig. 5.13**). While TEM result is consistent with the AUC results and CD results showing nanofibers formed at all tested pHs although the length of fibers was reduced at pH 5.5 due to the effect of lysine protonation (**Fig. 5.14)**.

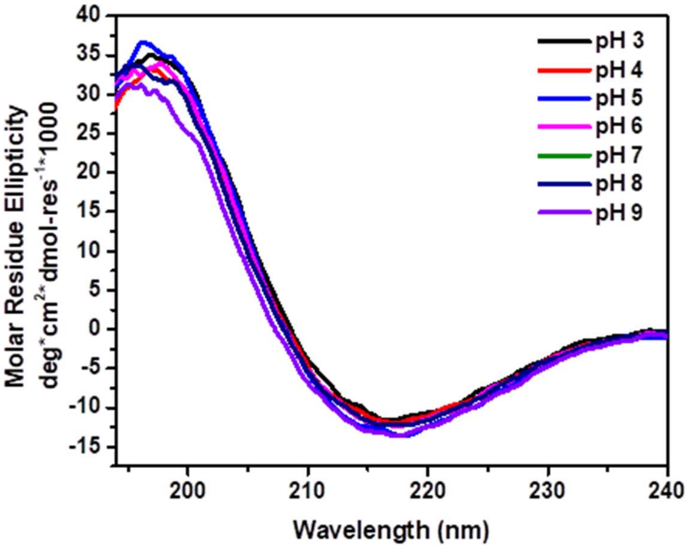

Figure 5.13 CD spectra of K_4G_5-L at different pHs in Britton–Robinson buffer with a final concentration at 50 μM.

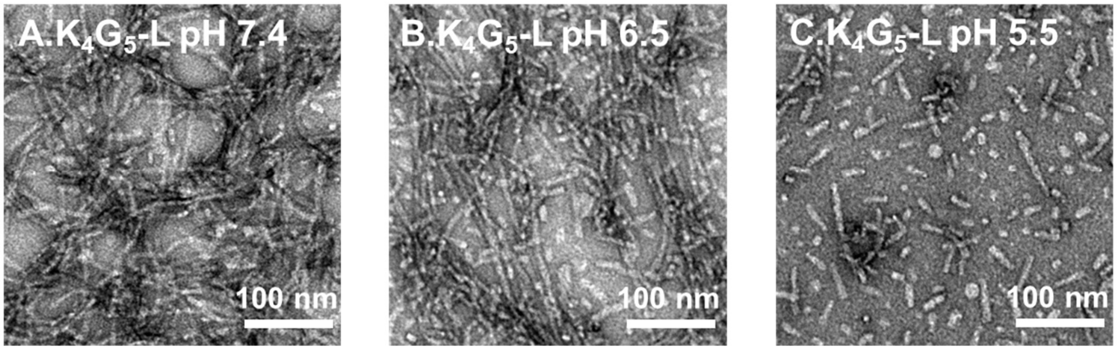

Figure 5.14 TEM of K_4G_5-L at (A) pH of 7.4, (B) pH of 6.5 and (C) pH of 5.5. The peptide was dissolved in 10 mM PB buffer at a concentration of 100 μM.

The supramolecular packing of MDPs with internal X_b was further investigated by the all-atom explicit water molecular dynamics (MD) simulations. The simulations reveal that the MDPs with deprotonated X_b remained in the β-sheet conformation for the duration of the 100 ns MD simulations (**Fig. 5.15**). In contrast, for the protonated X_b, the two β-sheet layers first separate from each other, followed by the loss of β-sheet nature in each strand (**Fig. 5.16A**). This suggests that the rapid β-sheet disassembly (of the protonated system) is driven by the repulsion between X_b residues at the interface of the two layers. The same results were also obtained for the X_p systems as well as between the systems with Leu versus Lys. For example, in **Fig. 5.16B**, we compare the evolution of β-sheet content during MD simulations between the different systems simulated. The figure clearly shows that all systems with positively charged residues lose their β-sheet nature within the first 25 ns, while the corresponding neutral systems remained in the β-sheet conformation. Taken together, these results support the important role and the effectiveness of having ionizable amino acids in the hydrophobic core to control the pH-dependent self-assembly and disassembly process.

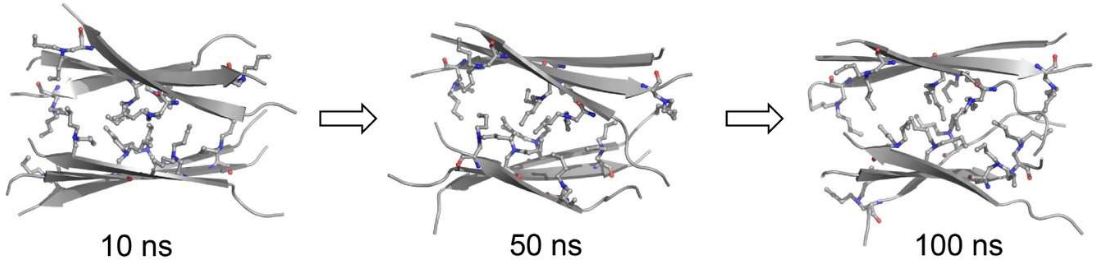

Figure 5.15 Snapshots were taken from the protonated X_b system at different times during the MD simulation. For clarity, the peptides are shown in the cartoon, but the X_b residues in the stick and all waters in the simulated system are not shown.

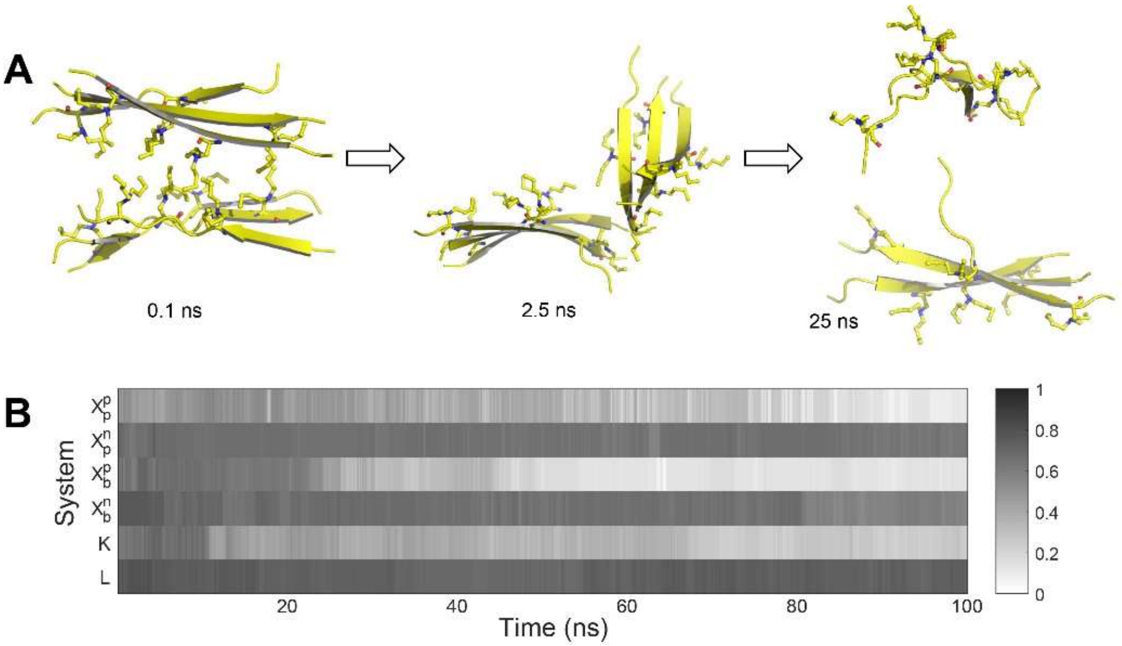

Figure 5.16 (A) Snapshots taken from the protonated X_b system at different times during the MD simulation. For clarity, the peptides are shown in the cartoon, but the X_b residues in the stick and all waters in the simulated system are not shown. (B) The change of β-sheet content during the 100 ns MD simulations. The β-sheet content varies between 0 for the random-coil structure and 1 for the perfect β-sheet conformation. For X_b and X_p, the superscript "n" and "p" refer to the neutral and protonated form residues, respectively.

5.2.4 Evaluation of pH-Dependent Antimicrobial Activity

The pH-responsive nanofibers with internal ionizable amino acids have a wide range of applications from acidity-targeted drug delivery to proton transport. In our previous study, we demonstrated that nanofibers with a natural ionizable amino acid, histidine, underwent acidity-triggered disassembly to release monomeric antimicrobial peptides to kill bacteria.[25] However, the antimicrobial activity of previous nanofibers against gram-negative bacteria is not potent enough. This is most likely because the disassembly process is not fully achieved due to solvent-exposed histidines having limited inefficient of disassemble. Even though we added 9 histidines to improve the triggered protonation, there are still peptide oligomers that limited the antimicrobial activity. With the new design of embedding ionizable unnatural amino acid into the hydrophobic core, we achieved the pH responsive peptide with fully disassembling under acidic conditions. The hypophysis is the fully disassemble will result in better antibacterial activity.

In an effort the development of more effective, responsive antimicrobial materials, we tested the antimicrobial activity of K_4G_5-X_b against a gram-negative bacterial, *e. coli* using the standard minimum inhibitory concentration (MIC) assay.(**Table 5.2**) The MIC of K_4G_5-X_b against *e. coli* at pH 5.5 was found at 2.5 μM which is four times lower than that of the most potent histidine-containing peptides tested previously at 10 μM. Meantime, the control peptide K_4G_5-L didn’t show any antibacterial activity at any pH. The result demonstrated the antimicrobial activity is all depending on the released monomeric peptide instead of the self-assemble peptide nanofiber.

Table 0.2 minimum inhibitory concentration (MIC) assay against *e.coli*

Name	pH 7.5	pH 6.5	pH 5.5
K_4G_5-X_b	>160 μM	20 μM	2.5 μM
K_4G_5-L	>160 μM	>160 μM	>160 μM

The acidity-triggered antimicrobial activity was further confirmed through a bacterial live-dead assay of *e. coli* treated with K_4G_5-X_b or the non-responsive peptide, K_4G_5-L. As shown in Fig **5.17A-C**, significantly more red fluorescence was shown for *e. coli* treated with K_4G_5-X_b at pH 5.5 which demonstrated bacterial cell death. While the antimicrobial activity of the same peptide is reduced as the pH got higher and closer to the near-neutral range. Bacteria treated with K_4G_5-L without the unnatural amino acid were found to show strong green fluorescence under all tested pH conditions (**Fig. 5.17D-F**). The result suggested K_4G_5-L has no antibacterial activity at all pH.

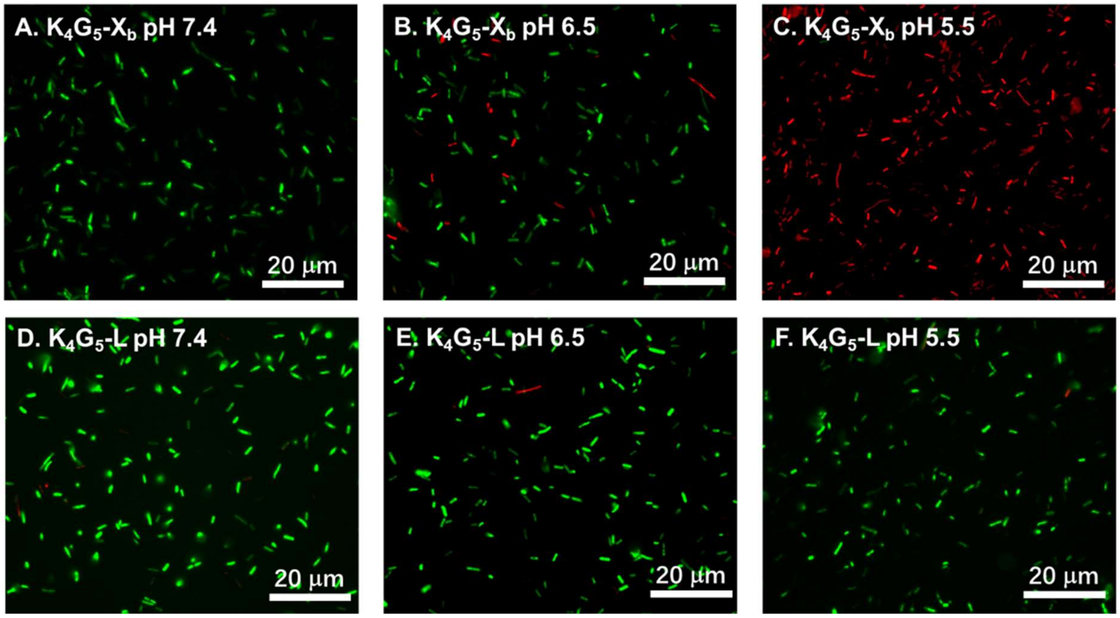

Figure 5.17 Fluorescence microscopic images of *e. coli* through live and dead bacterial assay. Top panel: *E.coli* treated with 10 µM K_4G_5-X_b at (A) pH 7.4, (B) pH 6.5 and (C) pH 5.5 for 3 h. Bottom panel: *E.coli* treated with 10 µM K_4G_5-L at (D) pH 7.4, (E) pH 6.5 and (F) pH 5.5 for 3 h. Live bacteria were stained with SYTO9 (green) and dead bacteria were stained with PI (red).

The physical interaction between K_4G_5-X_b and bacteria was studied by fluorescence microscopy upon incubation of nitrobenzoxadiazole (NBD)-labeled K_4G_5-X_b (20 µM) with *e. coli* for 3 h at different pHs. As shown in **Fig. 5.18**, peptide localization was represented by green fluorescence, the green fluorescence is co-localized with the bacterial cell membrane which suggested the peptide functionalizes on cell membrane. The green fluorescence is much higher for bacteria treated with NBD- K_4G_5-X_b at pH 5.5 compared to those at pH 6.5 and 7.5. The results suggested an enhanced binding affinity of peptides toward bacteria when they are disassembled upon acidification. The release of monomeric peptide further triggered antimicrobial activity at the acidic condition by membrane disruption.

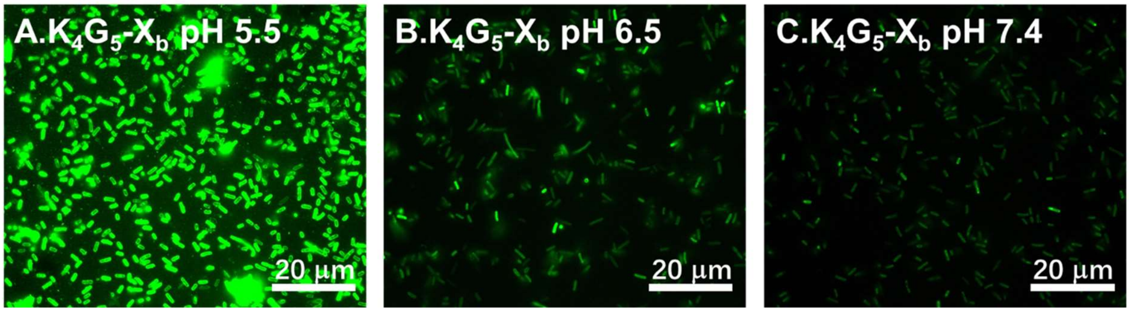

Figure 5.18 Fluorescence microscopic images of *E.coli* treated with NBD labeled K_4G_5-X_b at (A) pH 5.5, (B) pH 6.5 and (C) pH 7.4. NBD- K_4G_5-X_b was found to have enhanced attachment on the bacterial membrane in the acidic condition.

We further evaluated the cytotoxicity of K_4G_5-X_b toward healthy cell line NIH/3T3 fibroblasts by incubating cells with peptides at different concentrations for 24 h. The cell viability was quantified by the CCK8 assay. The results show that K_4G_5-X_b exhibited good cytocompatibility with IC (50) at ~ 80 μM at the neutral physiological condition (**Fig. 5.19**). The IC (50) is 32-fold higher than the MIC, peptide could be used for antibacterial application with minimum cytotoxic.

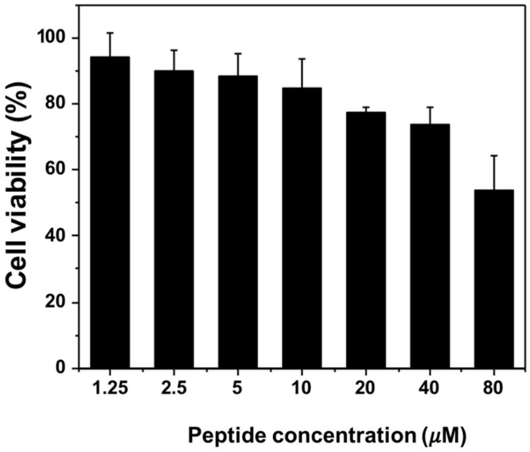

Figure 5.19 Cell viability of NIH/3T3 cells treated with K_4G_5-X_b at various concentrations for 24 h.

5.3 Conclusion

In summary, we demonstrated a new approach to the fabrication of pH-responsive self-assembled peptides composed of unnatural amino acids with ionizable tertiary amine side chains. These ionizable residues were positioned at specific sites of a *de novo* designed MDP. Upon self-assembly, they are buried in the hydrophobic pocket of the sandwich-like nanofiber that is formed by the MDP. The local hydrophobic microenvironment around the ionizable amino acids changed their pK_a from a basic value typically found for tertiary amino groups to a weakly acidic range. The reduction of the pK_a to a biologically relevant range has implications for many practical applications. While the proof-of-concept study was conducted through MDP design and self-assembly, the ionizable amino acids developed here can be readily applied to the synthesis and self-assembly of other amphiphilic peptide systems which have shown great promise toward a range of applications from vaccine and drug delivery to proton transport and energy transduction.

5.4 Experimental Section

Materials

Reagents used for the synthesis of Fmoc-X_p and Fmoc-X_b including (S)-3-Amino-2-(tert-butoxycarbonylamino) propionic acid, butyraldehyde, propionaldehyde, sodium cyanoborohydride, N-(9-fluorenylmethoxycarbonyloxy) succinimide were purchased from Fisher Scientific and used as received. Reagents related to peptide synthesis including Fmoc-amino acids, 6-(7-nitrobenzofurazan-4-ylamino) hexanoic acid, 4-methylbenzhydrylamine

(MBHA) rink amide resin, 2-(1H-benzotriazol-1-yl)-1,1,3,3-tetramethyluronium hexafluorophosphate (HBTU), piperidine, diisopropylethylamine (DIPEA), trifluoroacetic acid (TFA), triisopropylsilane (TIS), acetic anhydride and all solvents used in the synthesis, purification of amino acids and peptides as well as deuterated solvents for the NMR experiments were obtained from commercial sources and used without further treatment. Mueller Hinton Broth (MHB) medium was purchased from Sigma-Aldrich. Bacterial live-dead assay kit, agar, and Dulbecco's modified eagle medium (DMEM) were purchased from Fisher Scientific and used as received. CCK8 cell viability assay kit was obtained from Dojindo Molecular Technologies (Rockville, MD). α-methoxy-ω-carboxy PEG (MW = 750 Da) was purchased from Rapp Polymere. Fetal bovine serum (FBS) was purchased from VWR. Transmission Electron Microscopy (TEM) grids and uranium acetate dihydrate were purchased from Ted Pella, Inc. *Escherichia coli* (ATCC 25922) was purchased from ATCC.

Synthesis and Purification of Fmoc-X_p and Fmoc-X_b

Fmoc-X_b was synthesized from commercially available (*S*)-3-amino-2-(*tert*-butoxycarbonylamino) propionic acid in three steps. In the first step, (*S*)-3-amino-2-(*tert*-butoxycarbonylamino) propionic acid (2.00 g, 9.79 mmol) was dissolved in MeOH-water (1:1, 24 mL) mixture and cooled to 0°C. Then $NaBH_3CN$ (1.54 g, 24.5 mmol) was added in small batches over 5 mins. Butyraldehyde (4.4 mL, 49.0 mmol) was added dropwise over 2 mins, the cooling bath was removed, and the reaction was allowed to proceed at room temperature. After 24 h the solvent was evaporated completely and redissolved in 20 mL of DCM. 20 mL of cold TFA was added to the reaction mixture and stirred for 2 h at room temperature before evaporating the solvent and azeotroping with chloroform to remove the residual TFA. The crude was kept under high vacuum overnight before proceeding to the next step. The crude was dissolved in 46 mL of water and the pH was adjusted to 8-9 using $NaHCO_3$ (4.1 g, 49 mmol). A solution of *N*-(9-fluorenylmethoxycarbonyloxy) succinimide (3.6 g, 10.7 mmol) in dioxane (234 mL) was slowly added to the stirring solution of the amino acid. After the completion of the reaction, dioxane was evaporated and the residue was dissolved in water and acidified the solution with 6 M HCl. The product was extracted into the organic layer by washing with dichloromethane. The organic layer was combined, dried using anhydrous sodium sulfate and evaporated. The product was purified by flash column chromatography using 4% MeOH in DCM as the solvent system. The product is white powder (3.56 g, 8.12 mmol, 83% yield, $R_f = 0.4$ in 5% MeOH in DCM). ^1H NMR (400 MHz, DMSO-d_6) δ 7.90 (d, $J = 7.5$ Hz, 2H), 7.76 (d, $J = 8.4$ Hz, 1H), 7.71 (dd, $J = 7.6$, 2.9 Hz, 2H), 7.45 – 7.39 (m, 2H), 7.33 (td, $J = 7.5$, 1.2 Hz, 2H), 4.40 – 4.30 (m, 3H), 4.24 (t, $J = 6.7$ Hz, 1H), 3.34 (dd, $J = 13.5$, 5.3 Hz, 1H), 3.22 (dd, $J = 13.5$, 8.9 Hz, 1H), 2.98 (m, 4H), 1.55 (p, $J = 7.7$ Hz, 4H), 1.28 (h, $J = 7.4$ Hz, 4H), 0.88 (t, $J = 7.3$ Hz, 6H). $C_{26}H_{34}N_2O_4$ (ESI/MS): Expected $[M+H]^+$: 439.26, observed $[M+H]^+$: 439.30. Fmoc-X_p was synthesized using the same procedure for Fmoc-X_b but with propionaldehyde (3.5 mL, 49.0 mmol). The product was purified by flash column chromatography using 4% MeOH in DCM as the solvent system. The product is white powder (3.17 g, 7.7 mmol, 79% yield, $R_f = 0.3$ in 5% MeOH in DCM). ^1H NMR (400 MHz, DMSO-d_6) δ 7.90 (d, $J = 7.5$ Hz, 2H), 7.82 (d, $J = 8.6$ Hz, 1H), 7.71 (dd, $J = 7.6$, 2.9 Hz, 2H), 7.45 – 7.40 (m, 2H), 7.33 (td, $J = 7.5$, 1.2 Hz, 2H), 4.37 (m, 3H), 4.25 (t, $J = 6.7$ Hz, 1H), 3.40 (dd, $J = 13.7$, 4.8 Hz, 1H), 3.25 (dd, $J = 13.6$, 9.1 Hz, 1H), 2.97 (m, 4H), 1.59 (h, *J* = 7.3 Hz, 4H), 0.86 (t, *J* = 7.3 Hz, 6H). $C_{24}H_{30}N_2O_4$ (ESI/MS): Expected $[M+H]^+$: 411.23, observed $[M+H]^+$: 411.35.

Synthesis and Purification of Peptides

Peptides used were synthesized on a *Prelude*® peptide synthesizer at a 30 μmol scale using MBHA rink amide resin as the solid support using standard Fmoc solid-phase peptide synthesis procedures. Fmoc groups were deprotected by 20% (V/V) piperidine in DMF for 5 min (2 times). Fmoc protected amino acids, HBTU, and DIPEA (1:1:2) were dissolved in DMF and added to the resin reservoir. Upon completion of the synthesis, the N-terminus of the peptides were either PEGylated or acetylated. PEGylation was carried out using PEG-750, HBTU and DIPEA (1:1:2) in DMF, and acetylation was carried out in the presence of acetic anhydride and DIPEA in DMF. The peptides were cleaved from the resin using a mixture of TFA/TIS/H_2O (95/2.5/2.5 by volume) for 3 h. The cleavage solution was collected through filtration and neat TFA was used to wash the resin twice. Residual TFA was removed under moderate airflow. Cold diethyl ether was used to precipitate the residual peptide solution, followed by centrifugation four times. The crude peptide was dried under the vacuum overnight before HPLC purification. The peptide was purified using a preparative reversed-phase C4 column with a linear gradient of water/acetonitrile containing 0.05% TFA. Elution was monitored at 230 nm and 280 nm. The mass of all the peptides was confirmed by ESI/MS.

Circular Dichroism (CD) Spectroscopy

Samples were prepared by dilution from a 1 mM peptide stock solution in DI water to a concentration of 50 μM in Britton–Robinson buffer at variable pH of 3, 4, 5, 6, 7, 8, 9. The samples were incubated at 4 °C overnight. Data were collected from 250 nm to 190 nm at room temperature (RT) using a 1 mm cuvette, a bandwidth at 1 nm, scan rate at 100 nm/min, and a response time of 1 sec. Each spectrum was averaged from ten scans. The mDeg of rotation was converted to molar residual ellipticity via the formula $\theta = (mDeg \times 1000)/(c \times n \times l)$ where c is the concentration of the peptide solution expressed in mM, n is the number of amino acids in the peptide sequence and l is the path length of the cell used in mm.

NMR Spectroscopy

Samples were prepared by dissolving 5 mg peptides (sequence: CH_3CONH-$QWQLQX_bQLQX_bQL$) in 500 μL of D_2O. 10 times diluted solutions of deuterium chloride (35 wt % in D_2O) and sodium deuteroxide (30 wt % in D_2O) in D_2O were used to adjust to the desired pH. 1D NMR spectra were collected and accumulated from 16 scans on a Jeol JNM-ECZ400S/L1 FT NMR System Spectrometer and the 2D NMR spectra were collected and accumulated from 32 scans on a JEOL ECA-500 spectrometer. 1H-NMR chemical shifts are referenced to D_2O (4.65 ppm) and DMSO-d_6 (2.50 ppm). NMR data are reported as follows: chemical shift, multiplicity (s = singlet, d = doublet, t = triplet, q = quartet, p = pentet, m = multiplet), coupling constants (*J*) were reported in hertz (Hz), integration.

Transmission Electron Microscopy (TEM)

Samples were prepared by dilution from a 1 mM peptide stock solution in DI water to a concentration of 100 μM in PB buffer at variable pH. The samples were incubated overnight at 4 °C. 10 μL of peptide solutions was dropped onto a holey carbon grid. After 2 minutes, excess solution was carefully removed with filter paper. 10 μL of 2 wt % uranyl acetate aqueous solution was dropped onto the grid for negative staining. After ~ 2 minutes, the excess staining solution was removed, and the TEM samples were dried overnight before imaging.

Analytical Ultracentrifugation

Sedimentation velocity experiments were performed on a Beckman-Coulter Optima XL-I analytical ultracentrifuge equipped with an An-50 Ti 8-hole rotor. Double-sector centerpieces sandwiched between sapphire windows in a standard cell housing were loaded with 400 μL of sample and an equal volume of reference buffer (10 mM PB buffer at pH of 5.5). After 2 h of equilibration under vacuum at 20 °C, samples were centrifuged at 50,000 rpm or 10,000 rpm. Data was acquired using UV absorbance optics tuned to 230 nm for each sample. Sedimentation velocity data was fitted to a continuous *c(s)* distribution model using SEDFIT software. The buffer density and viscosity at room temperature were determined to be 0.99943 g/mL and 0.01005 cP, respectively using SEDNTERP. The partial-specific volume was estimated at 0.76122 mL/g for all peptides with sequence input through the Sednterp software. A resolution of 100 was utilized with a regularization level of 0.68. Time-invariant noise elements were removed from the data. All figures featuring *c(s)* distributions were generated in GUSSI software.

Molecular Dynamics (MD) Simulation

The starting structure of the MD simualtions was modeled for the $(QW)(QL)_5$ peptide in the β-sheet conformation and aligned the peptide as the three-stranded antiparallel orientation. Two three-straned β sheets were then placed relative to each other to form the (β-sheet) dimer, based on the tenascin fibronectic III domain structure (PDB ID: 1TEN[43]). Based on the resulting structure, five additional systems were model built by mutating the third and fifth residues into different residues: i.e., Lys, neutral X_b and X_p, and positively charged X_b and X_p residues, respectively. Each system was solvated with a 76 Å cubic box of TIP3P waters;[44] The protonated residue systems were also neutralized with Cl^- ions placed at random positions. The CHARMM36m force fields[45-47] were used to represent protein residues and the CHARMM general force field (CGenFF)[48] for X_b and X_p residues, respectively. Each system was first energetically minimized for 5000 steps and equilibrated for 100 ps at 298 K. Then, 100 ns MD simulations were performed at 300 K and 1 bar. The temperature and presseure of the system were maintained using the extended system Hoover thermostat[49] and Andersen barostat,[50] respectively. The system was integrated using the leapfrog Verlet and 2 fs time integration with SHAKE[51] applied to all bonds involing hydrogen atoms. The particle mesh Ewald (PME) summation method[52] was used for long-range electrostatic interactions and van der Waals interactions were evaluated up to 12 Å. All simulations were performed using CHARMM DOMDEC-GPU[53] and coordinates were saved at 10 ps intervals for post-processing analysis.

Minimum Inhibitory Concentration (MIC) Determination

E.coli was cultured in MHB media under constant shaking at 100 rpm at 37 ℃ for 8 h to reach the mid-exponential growth phase. The stock bacterial solution was plated on an agar plate for colony-forming unit (CFU) counting. Bacterial suspensions were diluted to approximately $2x10^5$ CFU/mL in MHB media at different pHs of 7.4, 6.5, and 5.5. Solutions of K_4G_5-X_b and K_4G_5-L at various concentrations (320, 160, 80, 40, 20, 10, 5, 2.5 μM) were prepared in different buffers, including Tris buffer (pH = 7.4, 20 mM), Tris buffer (pH = 6.5, 20 mM) and MES buffer (pH = 5.5, 20 mM). 50 μL of each peptide solution was mixed with 50 μL of bacterial solution in a 96-well plate and each sample was prepared with 3 replicates. The plates were incubated at 37 °C under constant shaking at 100 rpm for 18 h and the optical density at 600 nm was measured on a plate reader. MIC was determined as the minimum inhibitory concentration at which the OD value is equal to or less than 0.07.

Bacterial Viability Assay

Solutions of K_4G_5-X_b and K_4G_5-L were prepared at a final concentration of 20 μM in Tris buffers (20 mM) at pH of 7.4 and pH of 6.5 and MES buffer at pH of 5.5. respectively. 400 μL of *e.coli* suspensions at 10^8 CFU/mL was added to the confocal dish and incubated overnight at 37 °C without shaking. Bacterial suspensions were removed from the confocal dish and washed with PBS buffer (pH = 7.4) three times to remove any non-adherent bacteria. 100 μL of fresh MHB media was mixed with 100 μL of 20 μM peptide solutions in each respective buffer in the confocal dish. After incubation at 37 °C for 3 h, the culture media was removed and washed with PBS buffer (pH = 7.4) three times. Bacteria were stained with live/dead bacteria viability assay kit solution at 37 °C for 15 min followed by washing with

PBS buffer three times. Images were captured using an epifluorescence microscope and processed with ImageJ software.

Bacterial Membrane Localization Assay

Solution of NBD labeled K_4G_5-X_b were prepared at a final concentration of 40 μM in Tris buffers (20 mM) at pH of 7.4 and pH of 6.5 and MES buffer at pH of 5.5. 400 μL of *e.coli* suspensions at 10^8 CFU/mL was added to a confocal dish and incubated overnight at 37 °C without shaking. Bacterial suspensions were removed from the confocal dish and washed with PBS buffer (pH = 7.4) three times to remove any non-adherent bacteria. 100 μL of fresh MHB media was mixed with 100 μL of 40 μM peptide solutions in each respective buffer in the confocal dish. After 3 h of incubation, bacteria were washed with PBS buffer (pH = 7.4) three times. Images were captured using an epifluorescence microscope and processed with ImageJ software.

Cell Viability Assay

Solutions of K_4G_5-X_b were prepared at a final concentration of 1 mM in Tris buffers (pH = 7.4, 20 mM). NIH/3T3 cells were seeded onto a 96-well plate with a density of 10^4 cells/well and incubated at 37 °C in an incubator with 5% of CO_2 for 24 h. Cell culture suspension was removed and refreshed with 90 μL of DMEM medium. 10 μL of peptide at various concentrations (400, 200, 100, 50, 25, 12.5 μM) were prepared in Tris buffer (pH = 7.4, 20 mM) and added to each well to reach a final concentration at 40, 20, 10, 5, 2.5, 1.25 μM. All experiments were performed in four replicates. Cells incubated with 10 μL of Tris buffer (20 mM, pH = 7.4) were used as a control group. After 24 h of incubation, the culture medium was removed and a mixture of 90 μL fresh medium and 10 μL of CCK8 assay kit solution was added to each well. After 1 h of incubation at 37 °C, the suspension was removed and subject to UV measurement at 450 nm. Cell viability was calculated using the following equation.

$$Cell\ viability\ \% = \left({A_{peptide}}/{A_{control}}\right) \times\ 100$$

5.5 References

1. Wu, B.; Wang, X.; Yang, J.; Hua, Z.; Tian, K.; Kou, R.; Zhang, J.; Ye, S.; Luo, Y.; Craig Vincent, S. J.; Zhang, G.; Liu, G., Reorganization of hydrogen bond network makes strong polyelectrolyte brushes pH-responsive. *Sci. Adv.* **2016,** *2* (8), e1600579.
2. Tang, L.; Zeng, Z.; Wang, G.; Shen, L.; Zhu, L.; Zhang, Y.; Xue, Q., pH-Responsive Superwettability Surface: The Study of Oil Dewetting Ability from Air to Water on a Rough Surface and Selective Oil-Water Separation. *Adv. Mater. Interfaces* **2020,** *7* (22), 2001147.
3. Sonawane, S. J.; Kalhapure, R. S.; Govender, T., Hydrazone linkages in pH responsive drug delivery systems. *Eur. J. Pharm. Sci.* **2017,** *99*, 45-65.
4. Park, I.-K.; Singha, K.; Arote, R. B.; Choi, Y.-J.; Kim, W. J.; Cho, C.-S., pH-Responsive Polymers as Gene Carriers. *Macromol. Rapid Commun.* **2010,** *31* (13), 1122-1133.
5. Cui, J.; Li, Y.; Chen, D.; Zhan, T.-G.; Zhang, K.-D., Ionic Liquid-Based Stimuli-Responsive Functional Materials. *Adv. Funct. Mater.* **2020,** *30* (50), 2005522.
6. Carlini, A. S.; Choi, W.; McCallum, N. C.; Gianneschi, N. C., pH-Responsive Charge-Conversion Progelator Peptides. *Adv. Funct. Mater.* **2021,** *31* (13), 2007733.
7. Darnall, S. M.; Li, C.; Dunbar, M.; Alsina, M.; Keten, S.; Helms, B. A.; Xu, T., Organic Nanotube with Subnanometer, pH-Responsive Lumen. *J. Am. Chem. Soc.* **2019,** *141* (28), 10953-10957.
8. Kocak, G.; Tuncer, C.; Bütün, V., pH-Responsive polymers. *Polym. Chem.* **2017,** *8* (1), 144-176.
9. Lin, B. F.; Megley, K. A.; Viswanathan, N.; Krogstad, D. V.; Drews, L. B.; Kade, M. J.; Qian, Y.; Tirrell, M. V., pH-responsive branched peptide amphiphile hydrogel designed for applications in regenerative medicine with potential as injectable tissue scaffolds. *J. Mater. Chem.* **2012,** *22* (37), 19447-19454.
10. Yatvin, M. B.; Kreutz, W.; Horwitz, B. A.; Shinitzky, M., pH-Sensitive Liposomes: Possible Clinical Implications. *Science* **1980,** *210* (4475), 1253-1255.
11. Cheetham, A. G.; Zhang, P.; Lin, Y.-a.; Lock, L. L.; Cui, H., Supramolecular Nanostructures Formed by Anticancer Drug Assembly. *J. Am. Chem. Soc.* **2013,** *135* (8), 2907-2910.
12. Cui, H.; Webber, M. J.; Stupp, S. I., Self-assembly of peptide amphiphiles: From molecules to nanostructures to biomaterials. *Pep. Sci.* **2010,** *94* (1), 1-18.
13. Dong, H.; Paramonov, S. E.; Aulisa, L.; Bakota, E. L.; Hartgerink, J. D., Self-Assembly of Multidomain Peptides: Balancing Molecular Frustration Controls Conformation and Nanostructure. *J. Am. Chem. Soc.* **2007,** *129* (41), 12468-12472.
14. Feng, Z.; Wang, H.; Chen, X.; Xu, B., Self-Assembling Ability Determines the Activity of Enzyme-Instructed Self-Assembly for Inhibiting Cancer Cells. *J. Am. Chem. Soc.* **2017,** *139* (43), 15377-15384.
15. Hughes, M.; Debnath, S.; Knapp, C. W.; Ulijn, R. V., Antimicrobial properties of enzymatically triggered self-assembling aromatic peptide amphiphiles. *Biomater. Sci.* **2013,** *1* (11), 1138-1142.

16. Jiang, T.; Xu, C.; Liu, Y.; Liu, Z.; Wall, J. S.; Zuo, X.; Lian, T.; Salaita, K.; Ni, C.; Pochan, D.; Conticello, V. P., Structurally Defined Nanoscale Sheets from Self-Assembly of Collagen-Mimetic Peptides. *J. Am. Chem. Soc.* **2014,** *136* (11), 4300-4308.
17. Liu, Y.; Yang, Y.; Wang, C.; Zhao, X., Stimuli-responsive self-assembling peptides made from antibacterial peptides. *Nanoscale* **2013,** *5* (14), 6413-6421.
18. Makam, P.; Gazit, E., Minimalistic peptide supramolecular co-assembly: expanding the conformational space for nanotechnology. *Chem. Soc. Rev.* **2018,** *47* (10), 3406-3420.
19. Perry, S. L.; Leon, L.; Hoffmann, K. Q.; Kade, M. J.; Priftis, D.; Black, K. A.; Wong, D.; Klein, R. A.; Pierce, C. F.; Margossian, K. O.; Whitmer, J. K.; Qin, J.; de Pablo, J. J.; Tirrell, M., Chirality-selected phase behaviour in ionic polypeptide complexes. *Nat. Commun.* **2015,** *6* (1), 6052.
20. Raskatov, J. A.; Schneider, J. P.; Nilsson, B. L., Defining the Landscape of the Pauling-Corey Rippled Sheet: An Orphaned Motif Finding New Homes. *Acc. Chem. Res* **2021,** *54* (10), 2488-2501.
21. Raymond, D. M.; Nilsson, B. L., Multicomponent peptide assemblies. *Chem. Soc. Rev.* **2018,** *47* (10), 3659-3720.
22. Restuccia, A.; Hudalla, G. A., Tuning carbohydrate density enhances protein binding and inhibition by glycosylated β-sheet peptide nanofibers. *Biomater. Sci.* **2018,** *6* (9), 2327-2335.
23. Fletcher Jordan, M.; Harniman Robert, L.; Barnes Frederick, R. H.; Boyle Aimee, L.; Collins, A.; Mantell, J.; Sharp Thomas, H.; Antognozzi, M.; Booth Paula, J.; Linden, N.; Miles Mervyn, J.; Sessions Richard, B.; Verkade, P.; Woolfson Derek, N., Self-Assembling Cages from Coiled-Coil Peptide Modules. *Science* **2013,** *340* (6132), 595-599.
24. Jiang, L.; Xu, D.; Namitz, K. E.; Cosgrove, M. S.; Lund, R.; Dong, H., Protein-like Nanoparticles Based on Orthogonal Self-Assembly of Chimeric Peptides. *Small* **2016,** *12* (37), 5126-5131.
25. Chen, W.; Li, S.; Renick, P.; Yang, S.; Pandy, N.; Boutte, C.; Nguyen, K. T.; Tang, L.; Dong, H., Bacterial acidity-triggered antimicrobial activity of self-assembling peptide nanofibers. *J. Mater. Chem. B* **2019,** *7* (18), 2915-2919.
26. Cote, Y.; Fu, I. W.; Dobson, E. T.; Goldberger, J. E.; Nguyen, H. D.; Shen, J. K., Mechanism of the pH-Controlled Self-Assembly of Nanofibers from Peptide Amphiphiles. *J. Phys. Chem. C* **2014,** *118* (29), 16272-16278.
27. Dao, H. M.; Parajuli, S.; Urena-Benavides, E.; Jo, S., Self-assembled peptide fibrils with pH-sensitive reversible surface-active properties. *Colloid Interface Sci. Commun.* **2020,** *39*, 100325.
28. Ghosh, G.; Barman, R.; Sarkar, J.; Ghosh, S., pH-Responsive Biocompatible Supramolecular Peptide Hydrogel. *J. Phys. Chem. B* **2019,** *123* (27), 5909-5915.
29. Mei, L.; He, S.; Zhang, L.; Xu, K.; Zhong, W., Supramolecular self-assembly of fluorescent peptide amphiphiles for accurate and reversible pH measurement. *Org. Biomol. Chem.* **2019,** *17* (4), 939-944.

30. Raza, F.; Zhu, Y.; Chen, L.; You, X.; Zhang, J.; Khan, A.; Khan, M. W.; Hasnat, M.; Zafar, H.; Wu, J.; Ge, L., Paclitaxel-loaded pH responsive hydrogel based on self-assembled peptides for tumor targeting. *Biomater. Sci.* **2019,** *7* (5), 2023-2036.
31. Wakabayashi, R.; Higuchi, A.; Obayashi, H.; Goto, M.; Kamiya, N., pH-Responsive Self-Assembly of Designer Aromatic Peptide Amphiphiles and Enzymatic Post-Modification of Assembled Structures. *Int. J. Mol. Sci.* **2021,** *22* (7), 3459.
32. Wan, Y.; Liu, L.; Yuan, S.; Sun, J.; Li, Z., pH-Responsive Peptide Supramolecular Hydrogels with Antibacterial Activity. *Langmuir* **2017,** *33* (13), 3234-3240.
33. Wang, D.; Fan, Z.; Zhang, X.; Li, H.; Sun, Y.; Cao, M.; Wei, G.; Wang, J., pH-Responsive Self-Assemblies from the Designed Folic Acid-Modified Peptide Drug for Dual-Targeting Delivery. *Langmuir* **2021,** *37* (1), 339-347.
34. Zhang, P.; Wang, F.; Wang, Y.; Li, S.; Wen, S., Self-Assembling Behavior of pH-Responsive Peptide A6K without End-Capping. *Molecules* **2020,** *25* (9), 2017.
35. Isom Daniel, G.; Castañeda Carlos, A.; Cannon Brian, R.; García-Moreno, E. B., Large shifts in pKa values of lysine residues buried inside a protein. *Proc. Natl. Acad. Sci. U.S.A.* **2011,** *108* (13), 5260-5265.
36. Zhou, K.; Wang, Y.; Huang, X.; Luby-Phelps, K.; Sumer, B. D.; Gao, J., Tunable, Ultrasensitive pH-Responsive Nanoparticles Targeting Specific Endocytic Organelles in Living Cells. *Angew. Chem., Int. Ed. Engl.* **2011,** *50* (27), 6109-6114.
37. Jiang, L.; Xu, D.; Sellati, T. J.; Dong, H., Self-assembly of cationic multidomain peptide hydrogels: supramolecular nanostructure and rheological properties dictate antimicrobial activity. *Nanoscale* **2015,** *7* (45), 19160-19169.
38. Xu, D.; Dustin, D.; Jiang, L.; Samways, D. S. K.; Dong, H., Designed filamentous cell penetrating peptides: probing supramolecular structure-dependent membrane activity and transfection efficiency. *Chem. Commun.* **2015,** *51* (59), 11757-11760.
39. Xu, D.; Chen, W.; Tobin-Miyaji, Y. J.; Sturge, C. R.; Yang, S.; Elmore, B.; Singh, A.; Pybus, C.; Greenberg, D. E.; Sellati, T. J.; Qiang, W.; Dong, H., Fabrication and Microscopic and Spectroscopic Characterization of Cytocompatible Self-Assembling Antimicrobial Nanofibers. *ACS Infect. Dis.* **2018,** *4* (9), 1327-1335.
40. Chen, W.; Yang, S.; Li, S.; Lang, J. C.; Mao, C.; Kroll, P.; Tang, L.; Dong, H., Self-Assembled Peptide Nanofibers Display Natural Antimicrobial Peptides to Selectively Kill Bacteria without Compromising Cytocompatibility. *ACS Appl. Mater. Interfaces* **2019,** *11* (32), 28681-28689.
41. Yang, S.; Dong, H., Modular design and self-assembly of multidomain peptides towards cytocompatible supramolecular cell penetrating nanofibers. *RSC Adv.* **2020,** *10* (49), 29469-29474.
42. Dong, H.; Hartgerink, J. D., Role of Hydrophobic Clusters in the Stability of α-Helical Coiled Coils and Their Conversion to Amyloid-like β-Sheets. *Biomacromolecules* **2007,** *8* (2), 617-623.
43. Leahy, D. J.; Hendrickson, W. A.; Aukhil, l.; Erickson, H. P., Structure of a fibronectin type III domain from tenascin phased by MAD analysis of the selenomethionyl protein. *Science* **1992,** *258* (5084), 987-991.

44. Jorgensen, W. L.; Chandrasekhar, J.; Madura, J. D.; Impey, R. W.; Klein, M. L., Comparison of simple potential functions for simulating liquid water. *Chem. Phys.* **1983,** *79* (2), 926-935.
45. Best, R. B.; Zhu, X.; Shim, J.; Lopes, P. E.; Mittal, J.; Feig, M.; Mackerell, A. D., Jr., Optimization of the additive CHARMM all-atom protein force field targeting improved sampling of the backbone phi, psi and side-chain chi(1) and chi(2) dihedral angles. *J. Chem. Theory Comput.* **2012,** *8* (9), 3257-3273.
46. MacKerell Jr, A. D.; Bashford, D.; Bellott, M.; Dunbrack Jr, R. L.; Evanseck, J. D.; Field, M. J.; Fischer, S.; Gao, J.; Guo, H.; Ha, S., All-atom empirical potential for molecular modeling and dynamics studies of proteins. *J. Phys. Chem. B* **1998,** *102* (18), 3586-3616.
47. MacKerell Jr, A. D.; Feig, M.; Brooks, C. L., Improved treatment of the protein backbone in empirical force fields. *J. Am. Chem. Soc.* **2004,** *126* (3), 698-699.
48. Vanommeslaeghe, K.; Hatcher, E.; Acharya, C.; Kundu, S.; Zhong, S.; Shim, J.; Darian, E.; Guvench, O.; Lopes, P.; Vorobyov, I.; Mackerell, A. D., Jr., CHARMM general force field: A force field for drug-like molecules compatible with the CHARMM all-atom additive biological force fields. *J. Comput. Chem.* **2010,** *31* (4), 671-90.
49. Hoover, W. G., Canonical dynamics: Equilibrium phase-space distributions. *Phys. Rev. A Gen. Phys.* **1985,** *31* (3), 1695-1697.
50. Andersen, H. C., Molecular dynamics simulations at constant pressure and/or temperature. *Chem. Phys.* **1980,** *72* (4), 2384-2393.
51. Ryckaert, J.-P.; Ciccotti, G.; Berendsen, H. J., Numerical integration of the cartesian equations of motion of a system with constraints: molecular dynamics of n-alkanes. *J. Comput. Phys.* **1977,** *23* (3), 327-341.
52. Essmann, U.; Perera, L.; Berkowitz, M. L.; Darden, T.; Lee, H.; Pedersen, L. G., A smooth particle mesh Ewald method. *Chem. Phys.* **1995,** *103* (19), 8577-8593.
53. Hynninen, A. P.; Crowley, M. F., New faster CHARMM molecular dynamics engine. *J. Comput. Chem.* **2014,** *35* (5), 406-13.

Appendix A

Supporting data for chapter 4

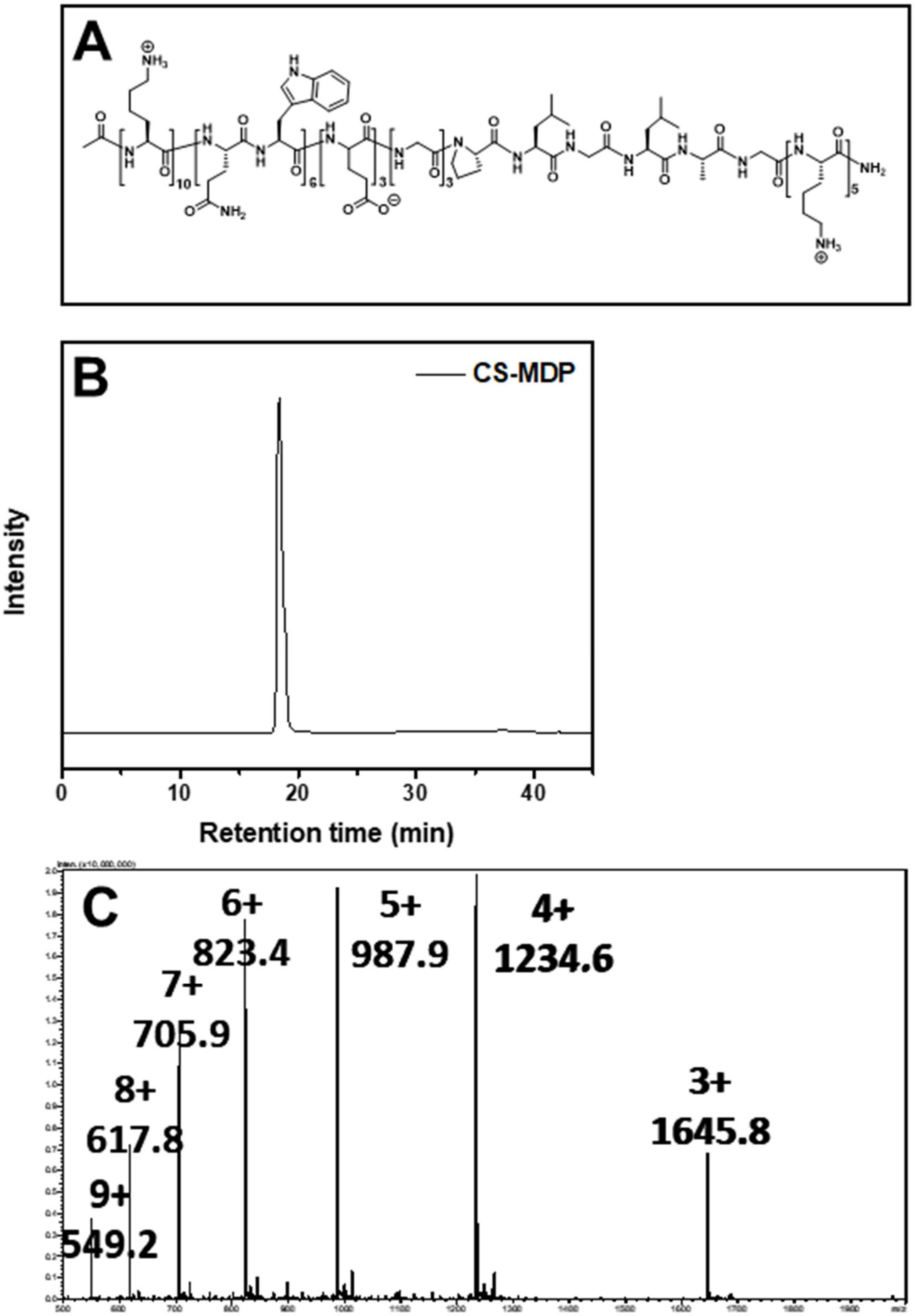

Figure A-S1 (1). (A) Chemical structure, (B) HPLC and (C) ESI/MS of CS-MDP.

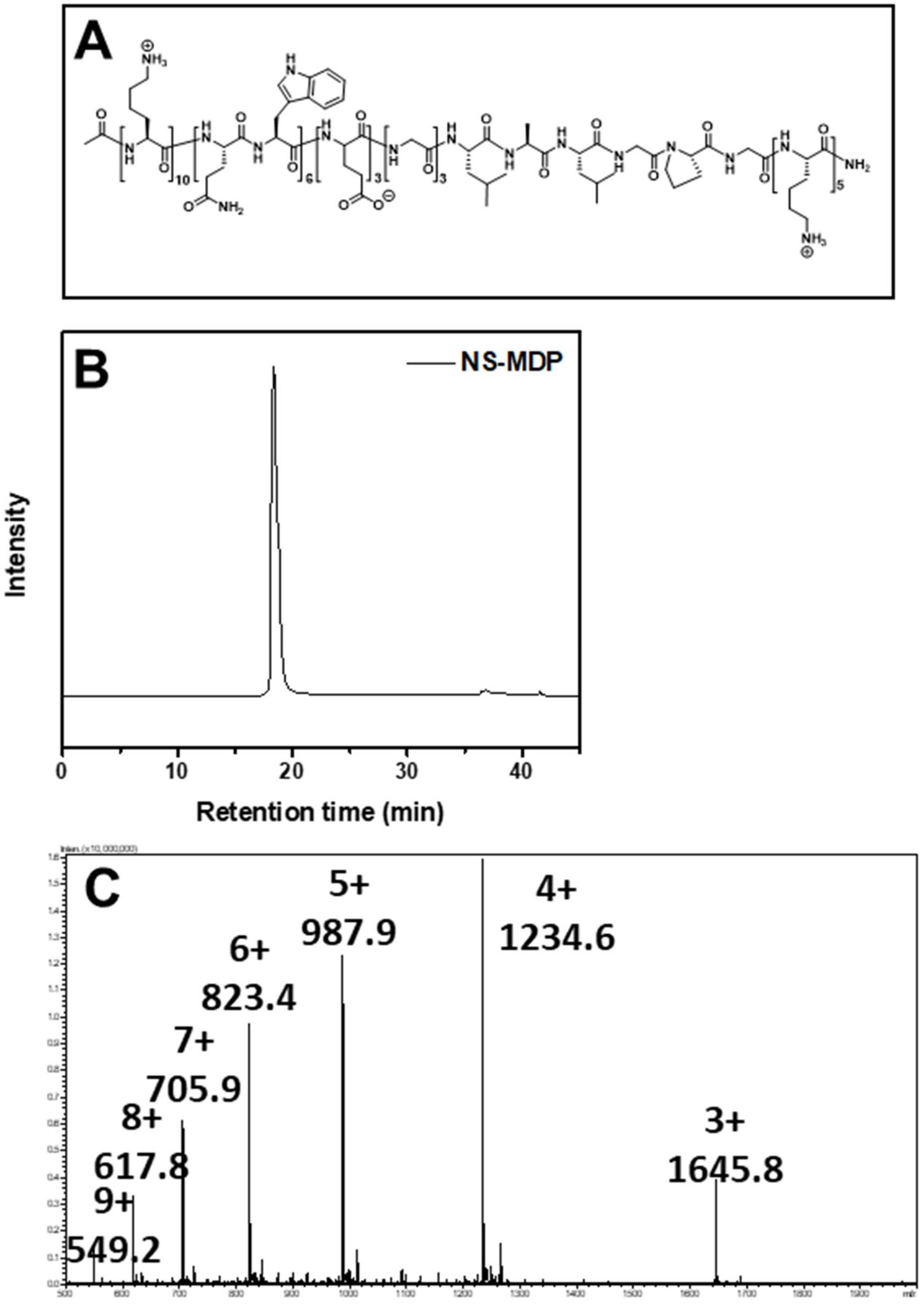

Figure A-S1 (2). (A) Chemical structure, (B) HPLC and (C) ESI/MS of NS-MDP.

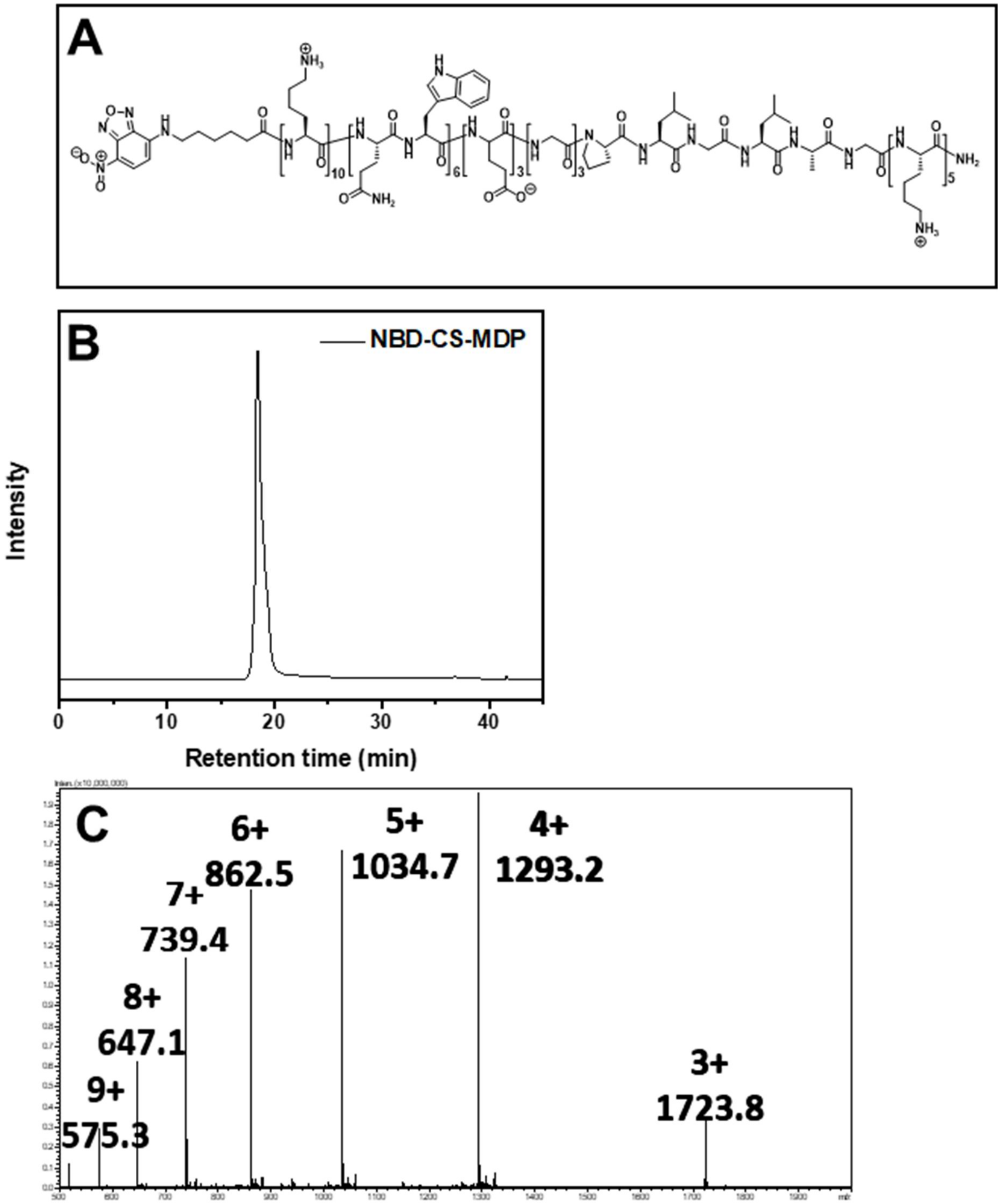

Figure A-S1 (3). (A) Chemical structure, (B) HPLC and (C) ESI/MS of NBD-CS-MDP.

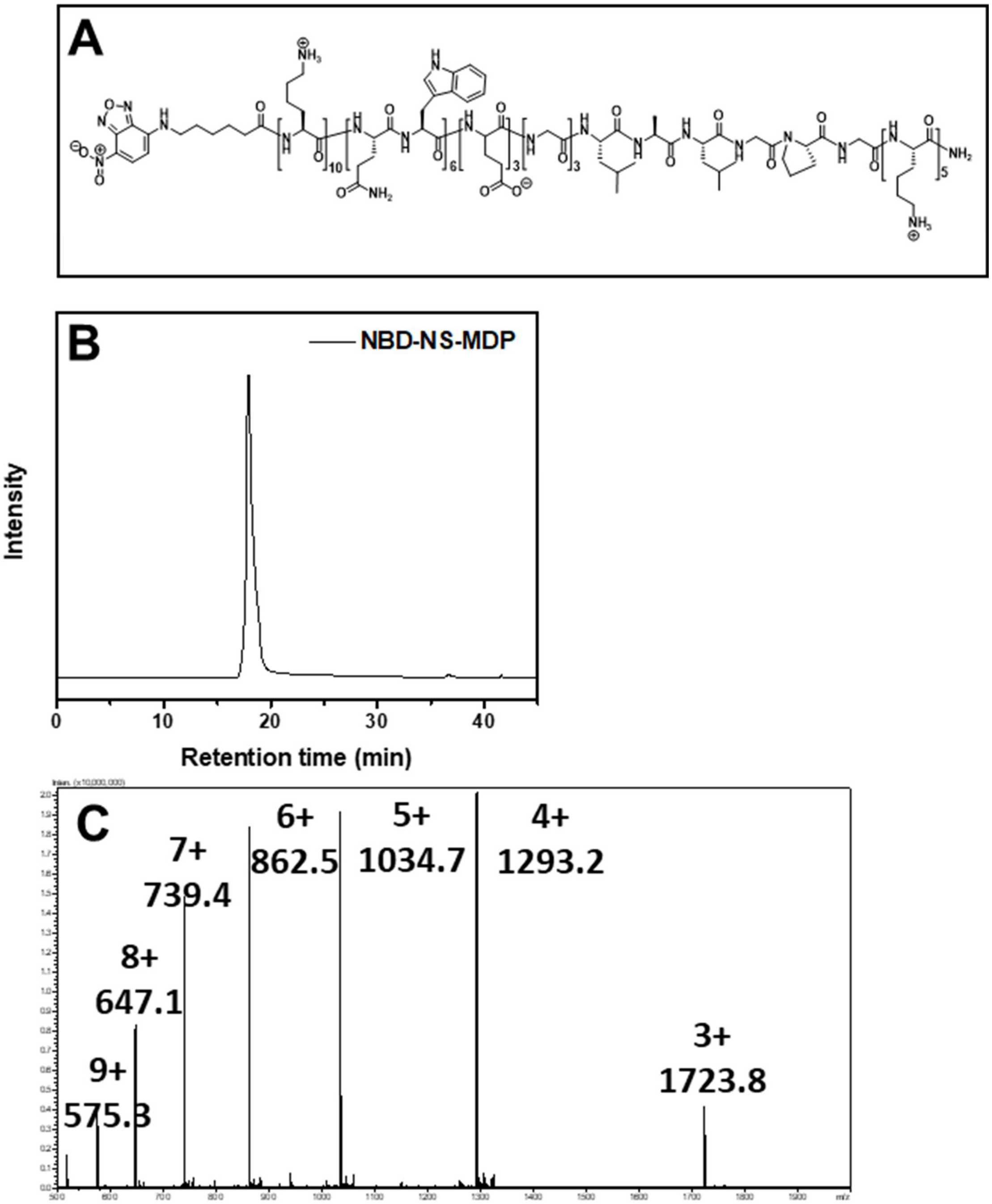

Figure A-S1 (4). (A) Chemical structure , (B) HPLC and (C) ESI/MS of NBD-NS-MDP.

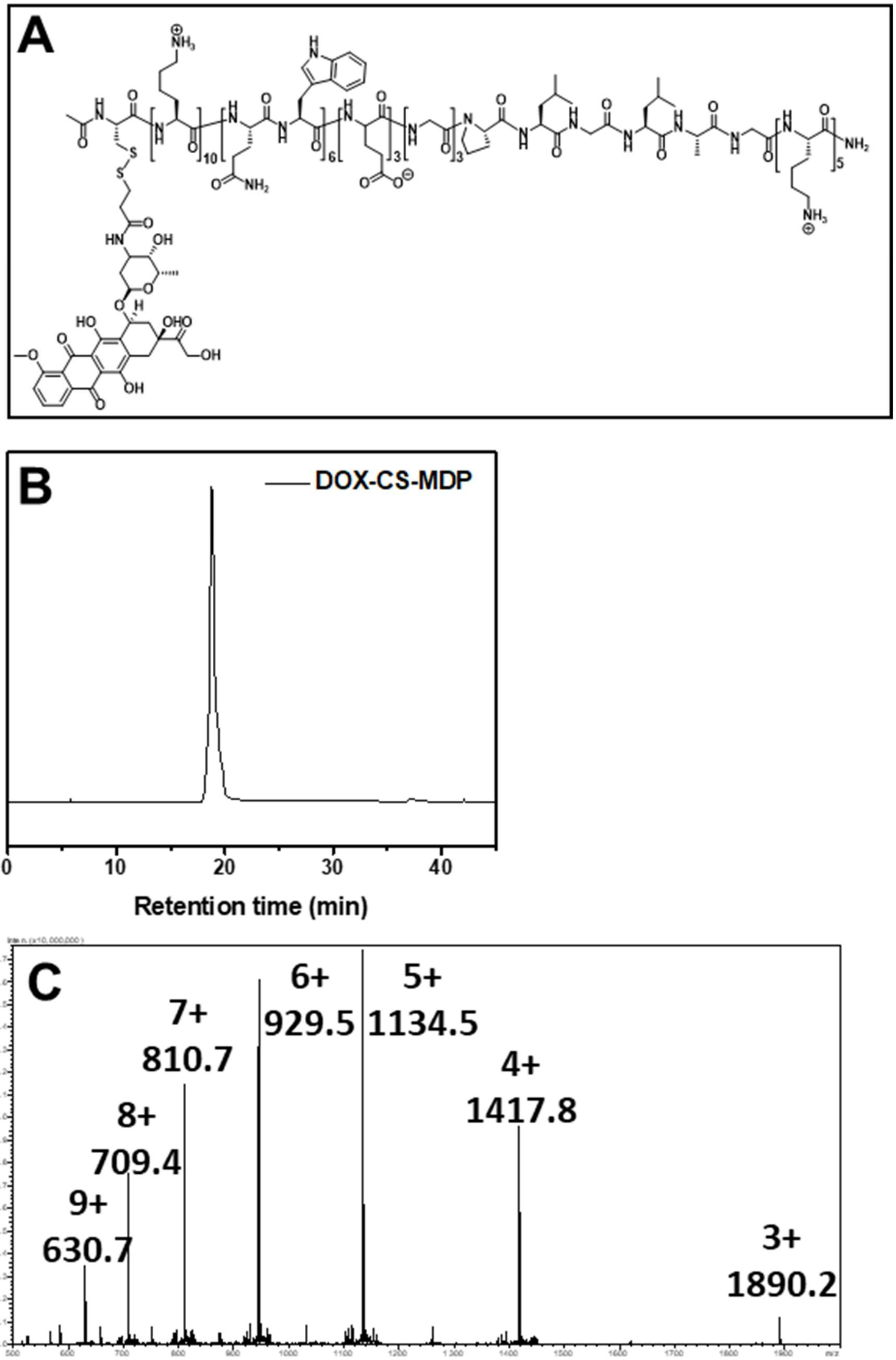

Figure A-S1 (A) Chemical structure, (B) HPLC and (C) ESI/MS of DOX-CS-MDP.

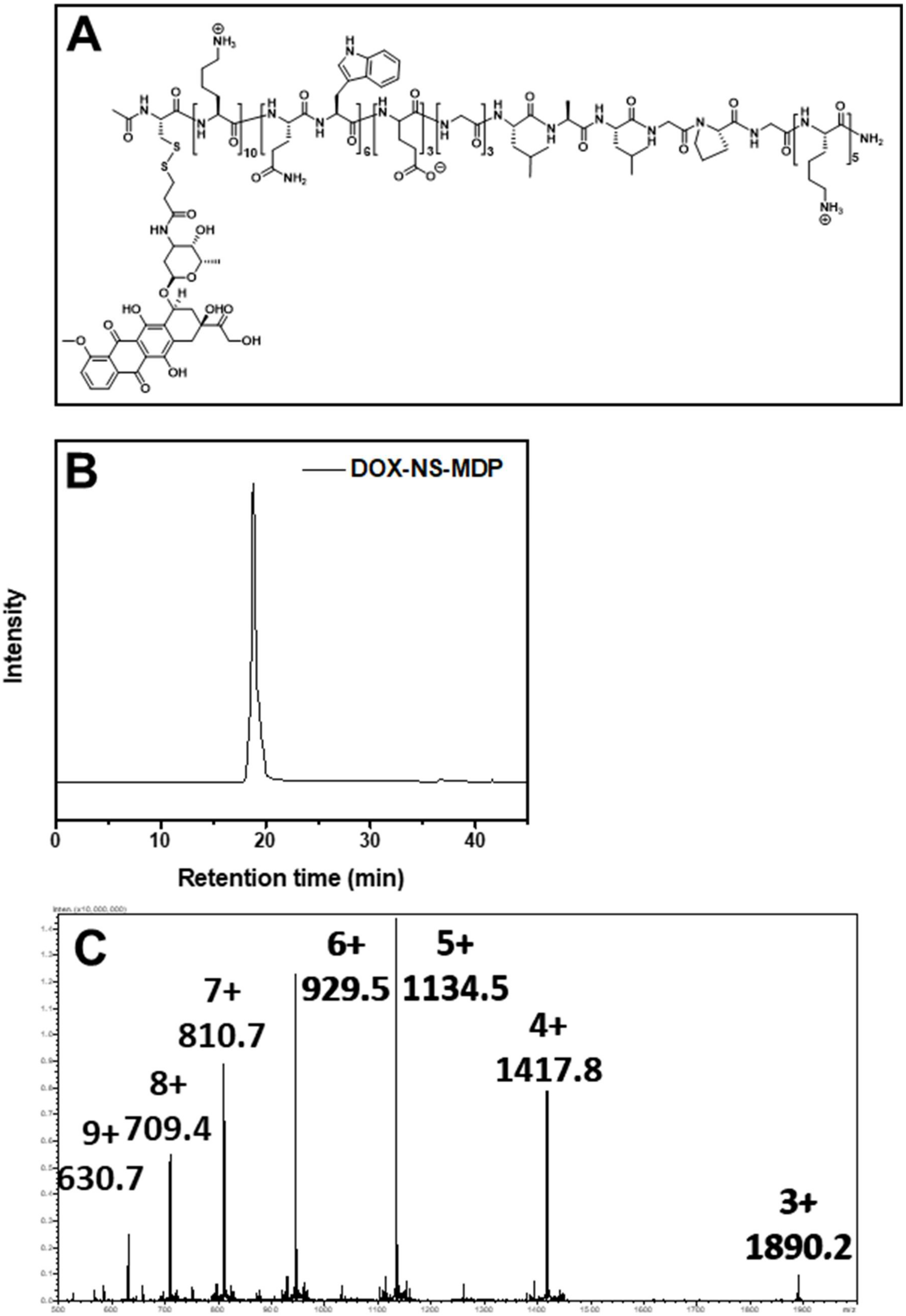

Figure A-S1 (6). (A) Chemical structure, (B) HPLC and (C) ESI/MS of DOX-NS-MDP.

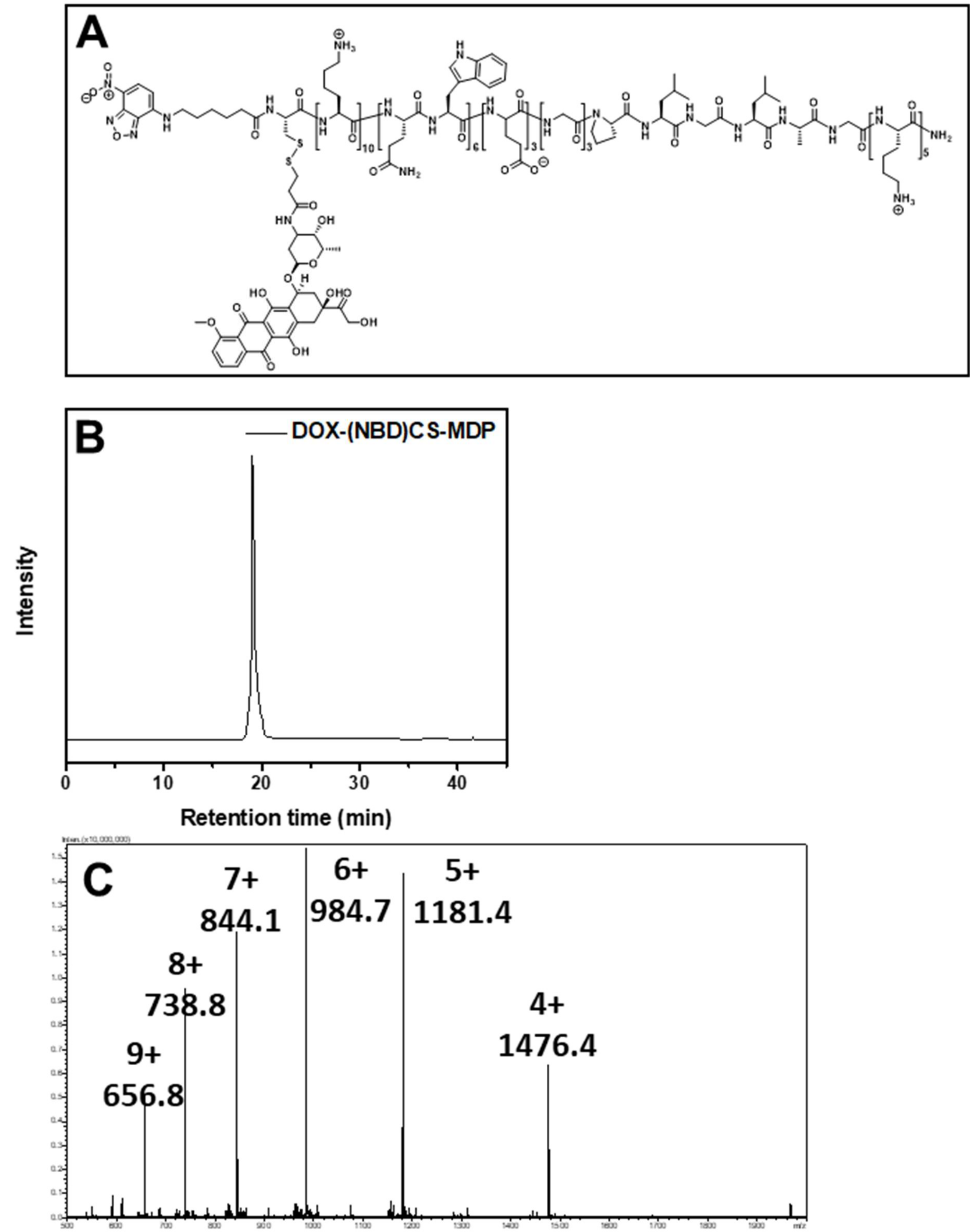

Figure A-S1 (7). (A) Chemical structure, (B) HPLC and (C) ESI/MS of DOX-(NBD)CS-MDP

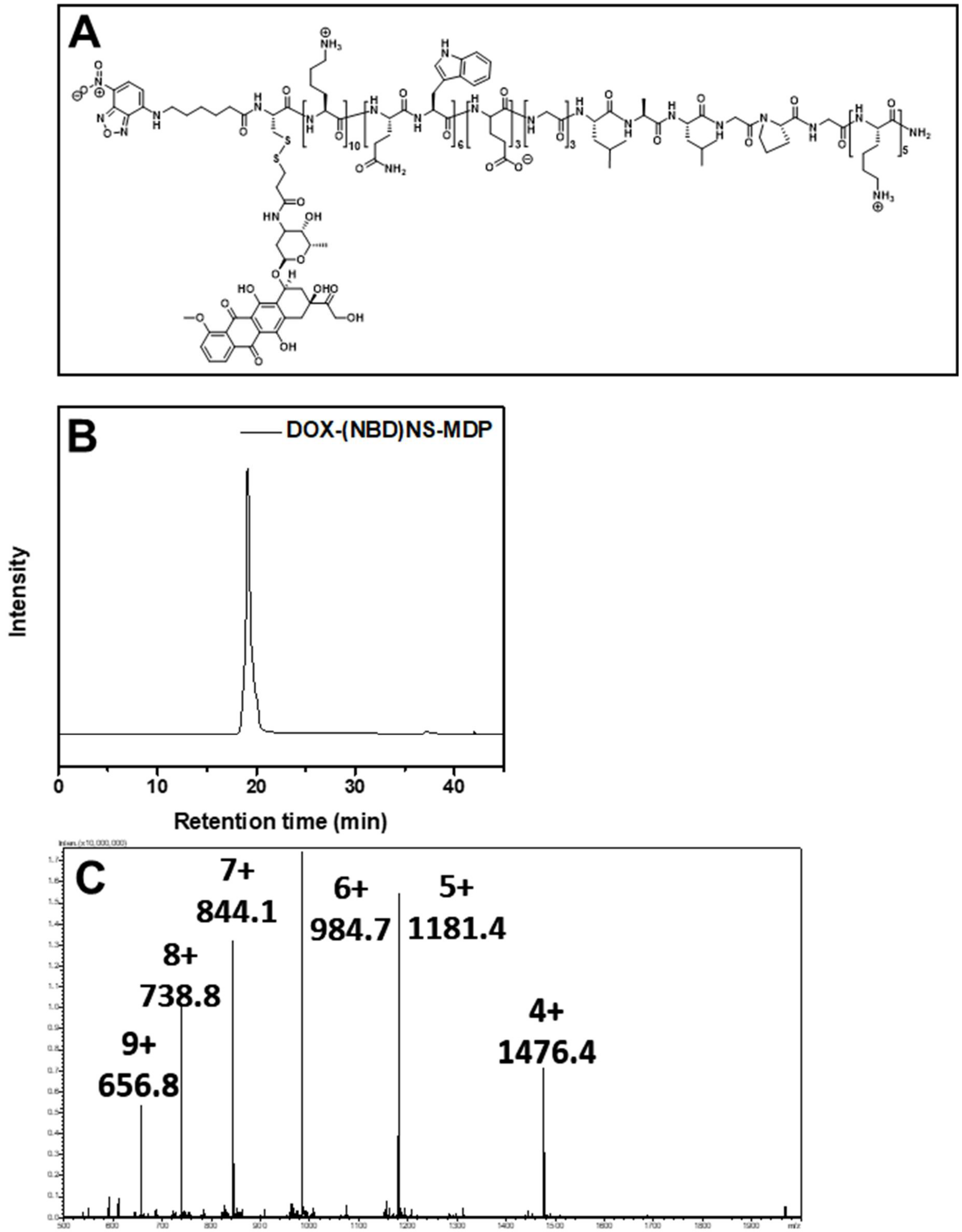

Figure A-S1 (8). (A) Chemical structure, (B) HPLC and (C) ESI/MS of DOX-(NBD)NS-MDP

Appendix B

Supporting data for chapter 5

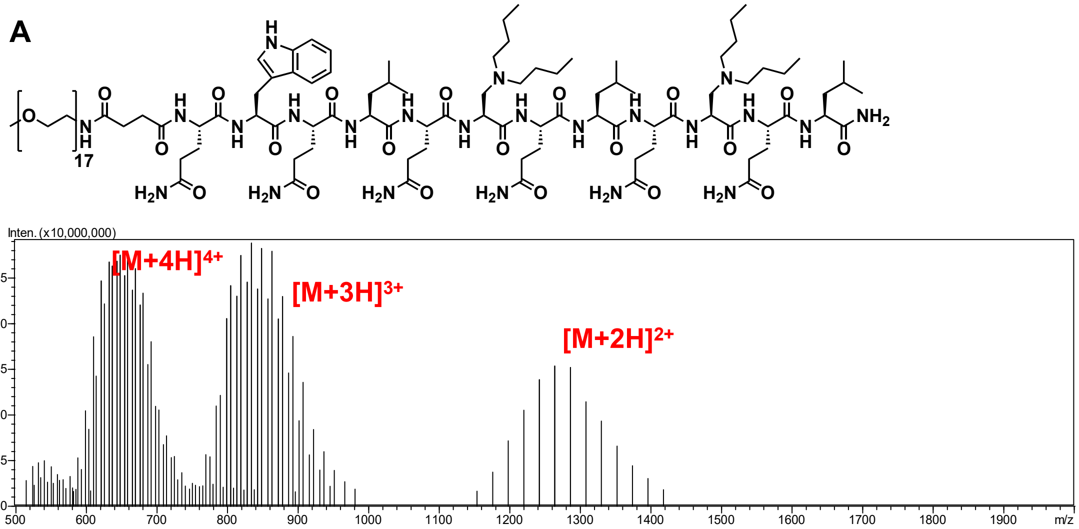

Figure B-S1 (A) Chemical structure and ESI-MS of PEG-X_b.

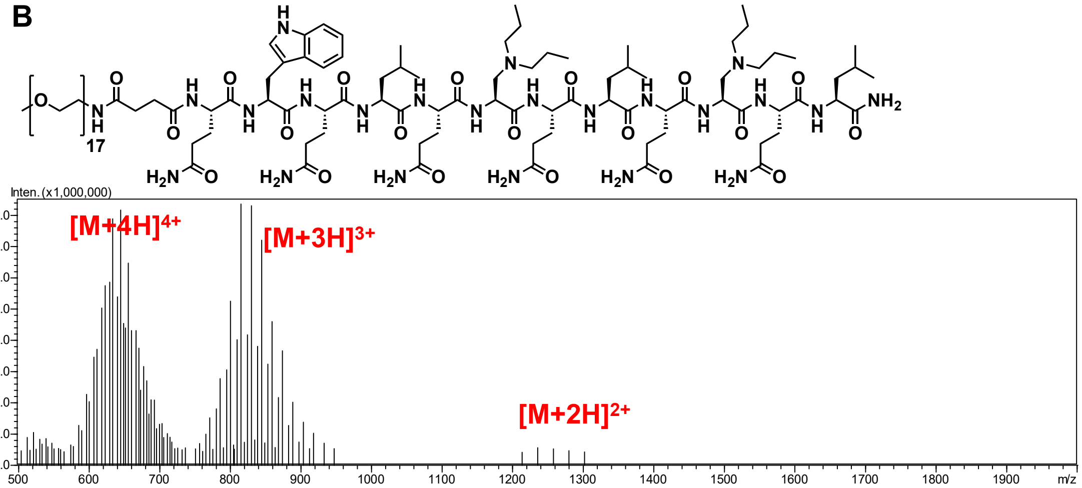

Figure B-S1 (B) Chemical structure and ESI-MS of PEG-X_p.

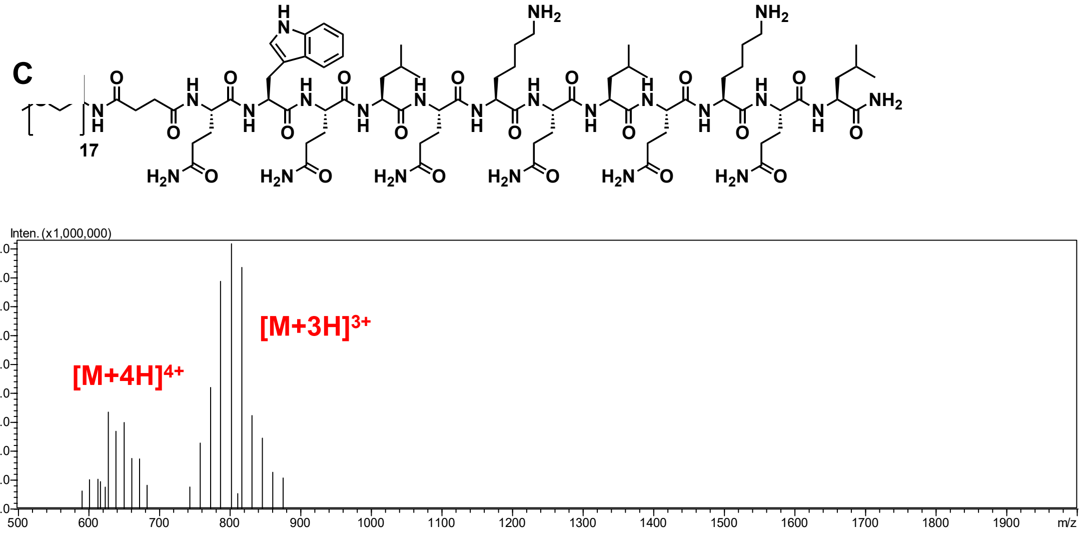

Figure B-S1 (C) Chemical structure and ESI-MS of PEG-K.

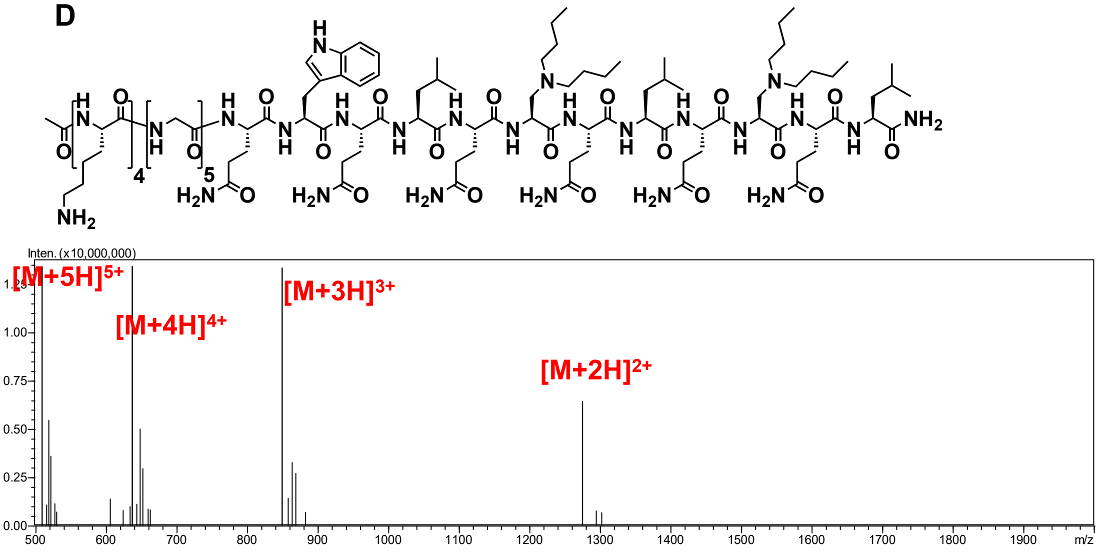

Figure B-S1 (D) Chemical structure and ESI-MS of K_4G_5-X_b.

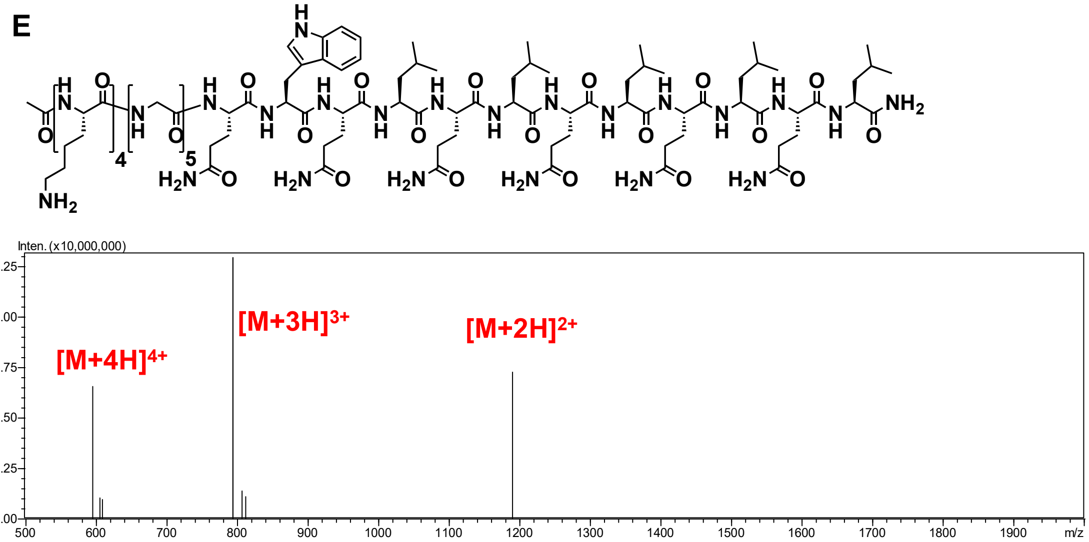

Figure B-S1 (E) Chemical structure and ESI-MS of K_4G_5-L.

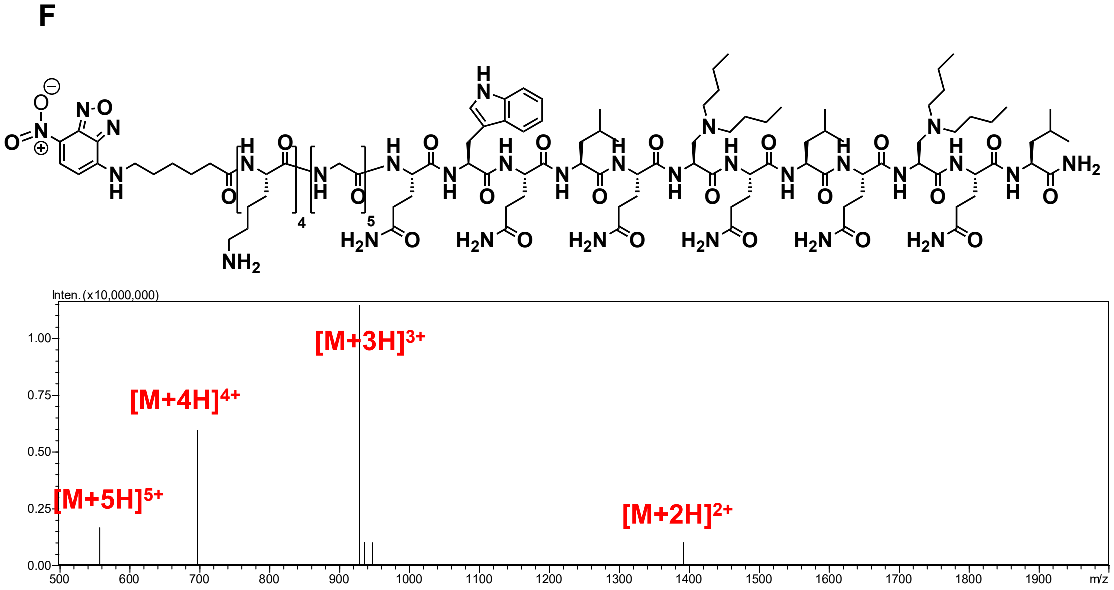

Figure B-S1 (F) Chemical structure and ESI-MS of NBD-K_4G_5-X_b.

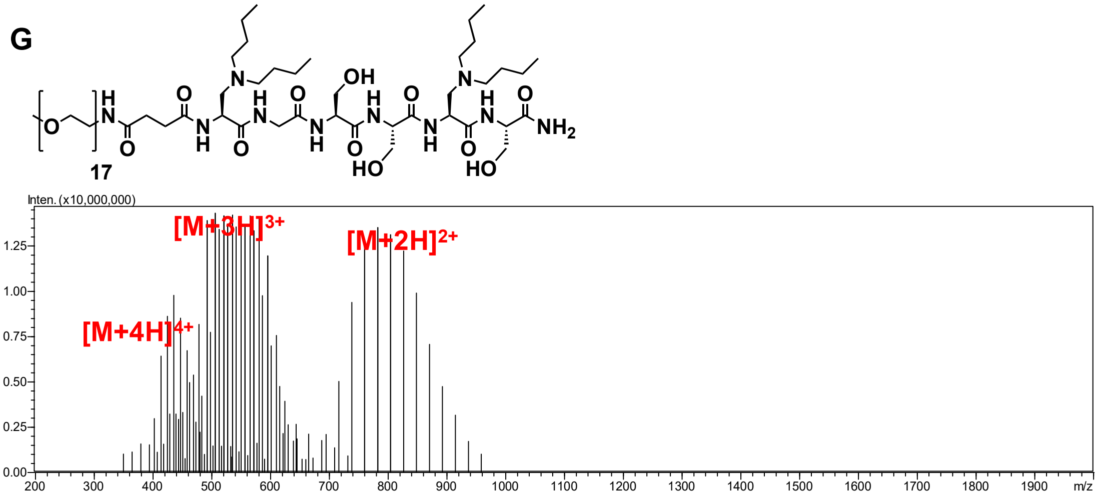

Figure B-S1 (G) Chemical structure and ESI-MS of PEG-X_bGSSX_bS.

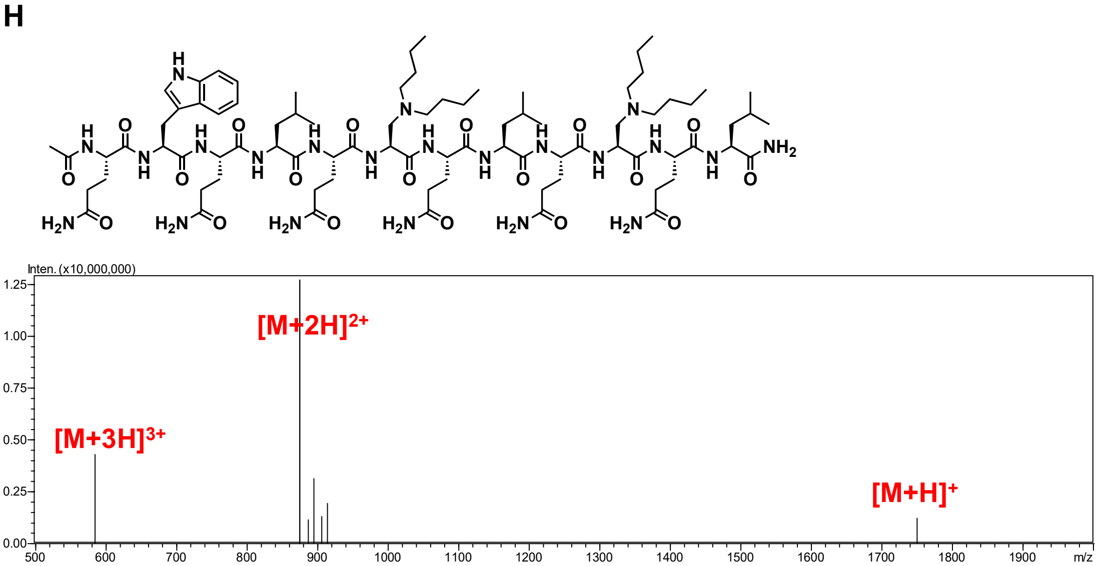

Figure B-S1 (H) Chemical structure and ESI-MS of CH_3CONH-QWQLQX_bQLQX_bQL.